Published in final edited form as:

Nanoscale. 2021 February 14; 13(6): 3374–3411. doi:10.1039/d0nr08353d.

Plasmonic Nano-Antimicrobials: Properties, Mechanisms and Applications in Microbe Inactivation and Sensing

Xingda An[a,c], **Shyamsunder Erramilli**[b,c], **Björn M. Reinhard**[a,c]

[a]Department of Chemistry, Boston University, Boston, MA 02215, United States.

[b]Department of Physics, Boston University, Boston, MA 02215, United States.

[c]The Photonics Center, Boston University, Boston, MA 02215, United States.

Abstract

Bacterial, viral and fungal infections pose serious threats to human health and well-being. The continuous emergence of acute infectious diseases caused by pathogenic microbes and the rapid development of resistances against conventional antimicrobial drugs necessitates the development of new and effective strategies for the safe elimination of microbes in water, food or on surfaces, as well as for the inactivation of pathogenic microbes in human hosts. The need for new antimicrobials has triggered the development of plasmonic nano-antimicrobials that facilitate both light-dependent and - independent microbe inactivation mechanisms. This review introduces the relevant photophysical mechanisms underlying these plasmonic nano-antimicrobials, and provides an overview of how the photoresponses and materials properties of plasmonic nanostructures can be applied in microbial pathogen inactivation and sensing applications. Through a systematic analysis of the inactivation efficacies of different plasmonic nanostructures, this review outlines the current state-of-the-art in plasmonic nano-antimicrobials and defines the application space for different microbial inactivation strategies. The advantageous optical properties of plasmonic nano-antimicrobials also enhance microbial detection and sensing modalities and thus help to avoid exposure to microbial pathogens. Sensitive and fast plasmonic microbial sensing modalities and their theranostic and targeted therapeutic applications are discussed.

1. Introduction

Microbes, especially selected types of bacteria, viruses, and fungi, can be pathogenic and cause infectious diseases in humans. For instance, bacterial pathogens *Mycobacterium tuberculosis* and *Vibrio cholerae* are responsible for tuberculosis and cholera, respectively. These diseases continue to infect millions of people every year worldwide and are associated with high fatalities rates. Viruses also cause a series of life-threatening and rapid-spreading infectious diseases. The global COVID-19 pandemic has provided a dire example of the significant burden viruses can inflict on public health systems. Even the common seasonal *influenza*, caused by various viral genera of *Orthomyxoviridae*, leads to hundreds of

---

bmr@bu.edu.

Conflicts of interest

S.E. and B.M.R have filed a patent “Photonic Inactivation of Pathogens” with Merck-Millipore.

thousands of fatalities worldwide each year.[1] In addition, some fungal infections are considered emerging global health threats. Candidiasis caused by yeast species can induce a life-threatening infection if it becomes invasive.[2]

Inactivation of food, water or surface-borne microbial pathogens is important to prevent microbial infections. To that end, different physical sterilization techniques are available, including UV illumination, gamma irradiation, autoclaving, as well as chemical sterilization through ozone, chlorine, formaldehyde, hydrogen peroxide, alcohol or other chemicals.[3] On the other hand, antimicrobial drugs have been developed for a selective inactivation of pathogens, in particular in human or mammalian hosts. Antibiotics, as an example, are utilized for bacterial inactivation commonly through impeding the peptidoglycan cell walls synthesis, DNA replication or protein synthesis processes.[4,5] Similarly, antifungal microbicides perturb the synthesis of fungal cell components like membrane sterols or cell wall glucans, leading to cell death.[2,6] Antiviral drugs typically function by inhibiting key steps of the viral infection, such as viral entry, reverse transcription (for RNA viruses), DNA integration or viral release from host cells. As antimicrobial drugs target specific molecular structures or mechanism of the microorganisms, they act selectively on the target microbes and have a much weaker effect on other organisms, which facilitates their use for treating microbial infections in humans or animals.

Although conventional antimicrobial approaches can achieve an effective inactivation of microbes, they also face numerous important challenges. Physical and chemical sterilization approaches can be energy intensive at large scales, while chemical sterilization approaches can have detrimental environmental effects.[7] Furthermore, the use of high energy radiation or reactive chemicals is precluded in some applications, for instance, for inactivating microbial pathogens in solutions containing valuable biologics that are sensitive to denaturation. For antimicrobial drugs, emergence of resistances in bacteria, fungi and viruses is becoming increasingly prevalent and threatening. The complex challenges faced by conventional antimicrobial strategies motivate the development of new strategies that are more energy effective, environmentally benign, and more resilient to the development of microbial resistances.

The need for alternative antimicrobial strategies has generated great interest in nanomaterials as nano-antimicrobials.[5,8] Different nanocrystals and mesoporous nanostructures have been utilized as nanocarriers for antimicrobial chemicals.[9–11] Selected photosensitizer nanoparticles (NPs),[12,13] metal-organic frameworks (MOFs)[14,15] and covalent-organic frameworks (COFs),[16,17] and semiconductor nanocrystals such as nitrides[18], chalcogenides,[19,20] and oxides including TiO_2,[21,22] ZnO,[23,24] $BiVO_4$,[25,26] perovskites,[27,28] etc. have all been shown to sustain photocatalytic inactivation of microbes upon photoexcitation. Photo-generated electron-hole pairs in these systems can initiate chemical reactions with H_2O or O_2 and result in the generation of reactive oxygen species (ROS) including peroxides (O_2^{2-}), singlet oxygen ($^1O_2$), superoxides ($O_2{\cdot}^-$) and hydroxyl radicals (·OH), which can induce oxidative stress and irreversible damage in microbial pathogens.[21,26,29] In general, these nano-antimicrobials have demonstrated great efficacy against various pathogen types, yet some important challenges and limitations still exist. For one, many of the semiconductor antimicrobials possess wide bandgaps (E_g), such as anatase TiO_2 (E_g = 3.2 eV) or ZnO (E_g =

3.0 eV), which require excitation in the UV, and can cause collateral damage to mammalian cells and biomolecules through non-specific photochemical reactions. Besides, despite some progress in enhancing the charge separation in nanoscale systems through doping,[30,31] heterostructure formation,[18,25,28] or dye sensitization,[32,33] rapid charge recombination and lack of specificity in photoreactivity still fundamentally limits the effectiveness of photocatalysis for pathogen inactivation.

Plasmonic metal NPs sustain coherent oscillations of surface charge density, referred to as localized surface plasmon (LSP) resonance (LSPR), which can be tuned to offer large optical cross-sections outside of the spectral range of strong molecular electronic absorptions. They are, thus, of great interest for enhancing the efficacy and specificity of light-driven antimicrobial effects, and are the topic of this review. The optical properties of plasmonic metal NPs are highly dependent on the composition, size and shape.[34,35] This tunability allows harvesting of a broad range of the electromagnetic spectrum from UV to IR. Photoexcitation of LSPRs can result in a series of photophysical responses, including strong electric (E-) field localization,[35,36] ballistic “hot” electron generation,[37,38] heating,[39] and nanocavitation.[40,41] These light-induced responses, in turn, drive a variety of antimicrobial effects based on plasmonic photocatalysis, photothermal therapy, or plasmonic shockwave generation among others (Figure 1). These photo-responses are complemented by light-independent antimicrobial effects that derive from the nanoscale size of the NPs, their surface properties, or their chemical composition. Some of the light-dependent and -independent mechanisms can occur simultaneously, potentially facilitating a synergistic enhancement of microbe inactivation, and decreasing the likelihood of microbial resistance development. Intriguingly, some plasmonic nano-antimicrobials have shown promise against multiple pathogens classes (e.g. viruses and bacteria) under conditions that are not harmful for mammalian cells or biologics.[42] Pan-microbial efficacy, selectivity and decreased likelihood for microbial resistances make plasmonic NPs a promising class of nano-antimicrobials. The large optical cross-sections, E-field enhancement, and increased local density of optical states at the plasmon resonance[35,43,44] are also of interest for providing unique sensing and imaging capabilities, such as through plasmon-enhanced fluorescence imaging,[45–48] surface-enhanced Raman spectroscopy (SERS),[49–52] LSPR sensing,[53,54] or plasmon coupling microscopy.[55–61] Plasmonic nano-antimicrobials are, consequently, desirable theranostic tools that enable pathogen inactivation and simultaneous monitoring of the inactivation process through plasmon-enhanced microscopic or spectroscopic approaches.

In this manuscript, we review the photophysical properties of plasmonic nano-antimicrobials and their applications for microbial pathogen inactivation and sensing. We categorize the plasmonic nano-antimicrobial effects into light-dependent and -independent inactivation, and controlled delivery and release pathways. The specific mechanisms of each pathways are discussed, and their antimicrobial efficacies for the tested pathogen types are compared. Finally, we review detection and quantification strategies of various pathogen types enabled by plasmonic NPs. These strategies help to avoid infections, facilitate a quantification of the efficacy of any antimicrobial strategy, and enable diagnostic and theranostic applications of plasmonic nano-antimicrobials.

2. Microbial Pathogens and Inactivation Metrics

2.1 Microbial Pathogens

Bacteria, viruses, and fungi are the three major classes of microbial pathogens that this review focuses on. Bacterial pathogens are prokaryotes, and can generally be categorized into Gram-positive and Gram-negative species based on the Gram staining test.[3,62] Gram-positive species typically contain a thicker peptidoglycan cell wall on top of a plasma membrane, whereas Gram-negative species possess an additional outer lipid membrane layer on top of a thinner cell wall and the regular cell plasma membrane (Fig. 2A). This extra membrane makes Gram-negative species generally more resilient against molecular or nanoscale biocides. Teichoic acids are present on the cell wall of Gram-positive species, while lipopolysaccharides are found on the outer membrane of Gram-negative bacteria. These compounds, together with anionic phospholipids in membrane structures, render both types of bacteria negatively charged. The effect of nano-antimicrobials is usually tested on both types to assess the generality of the antibacterial strategy. Mollicute bacteria, such as acholeplasma and mycoplasma, are a special type of bacteria that lack cell wall structures.[63] Therefore, small molecule antibiotics that target the inhibition of the synthesis of cell wall components are ineffective against these bacteria.

Infections by drug-resistant bacterial strains, such as methicillin-resistant *Staphylococcus aureus* (MRSA), are difficult to treat with conventional antibiotics. These species represent, therefore, good test platforms for plasmonic nano-antimicrobials. Bacterial strains with metal-reducing capabilities, such as *Arthrobacter sp.*,[64] are also important test targets for metal-based plasmonic systems, since ions released from plasmonic metal NPs can have a considerable antibacterial effect. In addition to suspensions of planktonic bacteria, bacterial spores or colonized bacteria in biofilms are also highly relevant targets for inactivation studies. Bacterial spores are dormant forms of bacteria that are highly resistant to microbicides, and can be re-activated and induce infections.[65,66] Biofilms are ubiquitous on a wide range of surfaces and can impact human health if present, for instance, in oral cavity, wounds or on medical implants.[3,67] As shown in Fig. 2B, biofilms contain bacterial cells encapsulated by an excreted extracellular matrix (ECM) consisting of polysaccharides, lipids, proteins and nucleic acids. The ECM provides bacterial pathogens with an additional degree of structural stability and resistance against conventional chemotherapy with antibiotics,[67,68] which necessitates the development of new and more effective inactivation strategies.

Fungi are eukaryotic microorganisms and can take on either single-celled growth pattern, or multicellular growth patterns in which the individual cells are connected through filaments called hyphae.[69] Some fungal species produce mycotoxins and/or induce severe infection in humans. Yeasts, such as *Candida* and *Cryptococcus,* are examples of fungi that can cause severe and systematic infections.[70] There is currently only a very limited number of microbicides, based on polyenes, azoles or echinocandins, available against invasive mycoses.[2,6] Similar as in bacteria, drug resistances can also evolve in fungi, as known from some *Candida* species and yeast *Saccharomyces cerevisiae*.[6,71] *Candida auris*, in particular, has recently attracted significant attention as new multidrug-resistant “superbug”.[2] Viruses can be categorized into many different classes based on their structure, nucleic acid composition (DNA *versus* RNA), host types and infection mechanisms. Since the chemical and physical responses of plasmonic nano-antimicrobials typically act on the surface of the viruses, classification of virus based on the surface structure into enveloped and non-enveloped viruses is most relevant in the context of this review. Non-enveloped viruses contain nucleic acids surrounded by a capsid shell primarily made of proteins, and include species such as adenovirus, norovirus and poliovirus. Enveloped viruses, such as coronavirus, Ebola and human immunodeficiency virus (HIV), possess an extra outer coat of glycoproteins and lipids around the nucleocapsid (Fig. 2C). Viruses are not unique to mammal hosts. Bacteriophages are viruses that reproduce in bacteria. Since they are relatively easy to generate in large quantities, bacteriophages have been included in multiple virus inactivation studies. High mutation rates render some virus species highly resistant to conventional antiviral drugs within a relatively short period of time.[72,73] There is, consequently, a need for new antiviral strategies that are effective against a broad range of virus species.

2.2 Quantification of Pathogen Inactivation

The most common approach for quantifying the reduction in bacterial and fungal loads in inactivation studies is by calculating the decrease in the Colony Forming Units (CFUs) concentration (CFUs/mL) on a decadic logarithmic ($\log_{10}$) scale. CFUs is a measure of the number of viable bacterial or fungal cells that are able to form a visible colony when plated on an agar plate. The log reduction value (LRV) describes the reduction in the load of a treated pathogen sample (C_t) relative to a no-treatment control (C_0) in CFUs/mL:[42]

$$LRV = log_{10}\left(\frac{C_0}{C_\mathrm{t}}\right) \qquad \text{Eq.(1)}$$

In the case of bacteria, a LRV ≥ 3 is generally considered a bactericidal effect.[74]

The optical density at 600 nm (OD_{600}) provides an alternative measure for determining the concentration of a bacterial suspension through application of the Lambert-Beer law. This method is, however, less sensitive and not applicable at low microbe concentrations or in the presence of plasmonic NPs with strong optical cross-sections. In addition, fluorescently labelled bacteria or fungi can also be used to assess the inactivation efficacy. Their fluorescence intensity can be feasibly quantified by plate reader or flow cytometry.[75,76]

Viral loads are quantified as plaque-forming units (PFUs). PFU is a measure of the number of viable viruses that lyse host cells and form a plaque. Similar as for bacteria and fungi, viral inactivation can be quantified in LRVs by comparing the reduction in viral load of a treated group (C_t) relative to that of a non-treated group (C_0) on a logarithmic scale.

If the pathogen concentrations are known as function of time, empirical disinfection kinetics can be determined using the Chick-Watson kinetics:

$$log_{10}\left(\frac{C_t}{C_0}\right) = -k_i[\chi]^n t \qquad \text{Eq.(2)}$$

where k_i is the inactivation kinetic constant, t is the time of the inactivation process, χ is the concentration of inactivating agent, and n is the reaction order.[14]

3. Localized Plasmons and Associated Properties of Plasmonic Nano-Antimicrobials

3.1 Size, Shape and Composition-Dependence of LSPR and Optical Properties

The photophysical microbe inactivation mechanisms of plasmonic nano-antimicrobials are enabled by their unique optical properties. The polarizability of a plasmonic NP is a fundamental property for describing the NP response to incident light. Polarizability, α, determines the polarization vector ($\boldsymbol{P}$) of the NP as $\boldsymbol{P} = \varepsilon_0\varepsilon_m\alpha\boldsymbol{E_0}$, where ε_0 is the permittivity of free space, ε_m is the dielectric function of the medium, and $\boldsymbol{E_0}$ is the incident electric field. For spherical NPs, with particle diameter, d, much smaller than the wavelength, λ, of the incident light ($d << \lambda$), the polarizability of a NP can be approximated by the Clausius-Mossotti relation as:

$$\alpha = 4\pi R^3\frac{\varepsilon - \varepsilon_m}{\varepsilon + 2\varepsilon_m} \qquad \text{Eq.(3)}$$

where R is the NP radius, and ε is the dielectric function of the metal. The LSPR occurs at the Fröhlich resonance condition, where α becomes maximum for the real part of $\varepsilon = -2\varepsilon_m$.[77] Noble metal NPs fulfill this requirement in the visible range of the electromagnetic spectrum. The expression of the NP polarizability in Eq. (3) can be generalized for non-spherical NPs by addition of a shape factor, κ:

$$\alpha = (1+\kappa)V\frac{\varepsilon - \varepsilon_m}{\varepsilon + \kappa\varepsilon_m} \qquad \text{Eq.(4)}$$

where V is the volume of the anisotropic NP.[78] For spheres, one finds κ=2. The polarizability of a particle determines absorption, scattering and extinction cross-sections, σ_{abs}, σ_{scat}, σ_{ext}, as:

$$\sigma_{abs} = k\ Im(\alpha) - \frac{k^4}{6\pi}\left|\alpha\right|^2 \qquad \text{Eq.(5)}$$

$$\sigma_{scat} = \frac{k^4}{6\pi}\left|\alpha\right|^2 \qquad \text{Eq.(6)}$$

$$\sigma_{ext} = k\ Im(\alpha) \qquad \text{Eq.(7)}$$

With $k = \frac{2\pi}{\lambda}$.[39]

It is evident from Equations (3)–(7) that the size, shape and dielectric function of the plasmonic material all contribute to determining the polarizability and optical responses of plasmonic NPs. These dependencies make it possible to tune the optical response of plasmonic NPs across the UV-visible-NIR spectrum (Figure 3) through rational synthetic strategies that control size, shape and composition of the NPs.[34,79–81] The ability to control LSPR frequencies through shape is particularly useful for many applications. For instance, Au nanorods (NRs) support a longitudinal LSPR mode that can be red-shifted to the near infrared (NIR) region by choice of a sufficiently high aspect ratio.[82,83] As NIR radiation possesses larger tissue or medium penetration depths than visible light, NIR-responsive metal NPs are of interest for microbial inactivation applications in tissues or in medium.[42,67,84] Au nanobipyramids are another example of metallic nanostructures whose optical responses can be controlled through their aspect ratio. Epitaxial deposition of Ag onto Au bipyramids (BPs) was demonstrated to be a rational strategy for either blue- or red-shifting the LSPR of a given BP in a controlled fashion by altering the tip width and/or length of the Au BPs.[85,86] A multitude of other plasmonic noble metal nanostructures were custom-designed for specific antimicrobial applications. For instance, nanostructures with high specific surface area, such as nanosheets,[87] nanocorals[88] or porous NPs[19] have been developed to facilitate light-induced phenomena at the interface between NP and ambient medium; core-shell nanostructures[84,89] and electro-spun nanofibers[90,91] also provide great opportunities for the formation of heterostructures and the incorporation of antimicrobials.

The size of NPs is also an important parameter that determines the ratio between absorption and scattering of individual plasmonic NPs. Baffou and Quidant performed a detailed analysis of the size-dependence of the optical cross-sections for spherical metal NPs.[39] The authors revealed that for Au NPs with $d < 90$ nm, the peak absorption cross-section is larger than the peak scattering cross-section, whereas for larger NPs ($d > 90$ nm) the peak scattering cross-section is larger than the peak absorption cross-section. These and other findings show that LSPR decay is dominated by radiative processes for large NP sizes, but that plasmon decay by dissipation becomes more important as the NP size decreases.[34] The dependence of the plasmonic response on size, shape, and composition provides the flexibility required to adapt the materials properties of plasmonic nano-antimicrobials to pathogen inactivation applications via different mechanisms and against different microbial species.

3.2 Photophysical Properties

3.2.1 Promoting Molecular Excitation and Emissions through Plasmonic E-Field and Local Density of States Enhancement.—The excitation and decay of an LSPR is associated with photophysical responses that can give rise to numerous light-dependent antimicrobial effects of plasmonic NPs. One important property of the LSPR is the generation of an intense local Electric (E-)field around individual NPs (Fig. 4A) that can be further enhanced in the junction between NPs in clusters of near-field coupled NPs (Fig. 4B).[36,92] This E-field enhancement has been applied to promote the photoexcitation of fluorophores and the reactivity of photocatalysts or photosensitizers (PSs).[93] In this context, plasmonic NPs are utilized as efficient nanolenses that boost the photoexcitation rates and/or photoconversion efficiencies of molecules localized within the localized E-field. Fundamentally, these processes rely on an energy transfer from the excited plasmon to the molecular adsorbates.

Localizing a fluorophore or a PS in the direct vicinity of a metal NP carries, however, also the risk of a metal-associated rapid quenching of the photoexcited state. In the case of quantum emitters, the distance-dependent quenching of the photoexcited state is well characterized by both calculations and experimental studies.[94–96] Fig. 4C contains plots of the excitation rate enhancement and quantum yield for a single dye molecule in the vicinity of an 80 nm Au NP as function of separation. Importantly, the quenching efficiency drops faster with increasing separation (indicated by the increase in quantum yield) than the E-field mediated excitation rate enhancement,[96] resulting in an optimum separation for fluorescence emission rate enhancement (Fig. 4D). In total analogy, we can expect that pinning of a photoreactive PS to a plasmonic NP at an optimum separation represents a viable strategy to enhance the formation of a reactive excited species and to boost the associated photoreactivity. This hypothesis was tested in a series of studies,[93,97–99] which demonstrated that for NPs with sizes in the range of 40–67 nm, strong quenching of the photoexcited states through the metal dominates at separations < 2 nm; whereas at distances > 10 nm, the plasmonic E-field intensity is no longer strong enough to sustain evident enhancement. These two thresholds define a working range of 2–10 nm for E-field enhanced photoexcitation of photocatalysts, PSs, or quantum emitters with limited quenching.

LSPRs of plasmonic NPs increase the Local Density of electromagnetic States (LDOS) with direct effects for the spontaneous decay of excited quantum emitters located in the vicinity of the NP.[35,43,44] In general, the spontaneous decay rate can be approximated by Fermi's golden rule as:[96]

$$\gamma = \frac{2\omega}{3\hbar\varepsilon_0}\left|p\right|^2 \rho(r_m, \omega) \qquad \text{Eq.(8)}$$

where ρ is the local density of electromagnetic states, ω is the transition frequency, $\boldsymbol{p}$ is the transition dipole moment, and $\boldsymbol{r_m}$ the location of the molecule. Enhanced radiative rates due to the large LDOS associated with the LSPR represents a second enhancement mechanism of photoluminescence in addition to the E-field-associated enhancement of excitation rates.

The E-field-enhanced photoexcitation of PSs and the associated gain in photoreactivity has been exploited for the light-driven inactivation of microbes in plasmonic photodynamic chemotherapy (section 4.1.1), while plasmon-enhanced fluorescence emission allows for a sensitive detection of microbial pathogens (section 5.2).

3.2.2 Plasmonic Charge Carrier Production and Transfer.

—Another mechanism of plasmonic photoreactivity involves transfer of charge and energy from the metal to adsorbate acceptor levels. Plasmonic charge transfers can take place through either indirect or direct pathways. The former requires the generation of kinetically excited "hot" charge carriers through a non-radiative decay of excited plasmons. This decay, referred to as

Landau damping, generates hot electrons (e^{-}) and holes ($h^{\cdot}$) (Figure 5, process (1)). Hot electrons possess an energy distribution that resembles a Fermi-Dirac distribution at a much higher temperature,[37,38,100,101] which facilitates their transfer into higher-lying unoccupied molecular orbitals or acceptor bands of semiconductors in direct contact with the NP, resulting in a charge separation of the generated e^{-} and $h^{\cdot}$ (process (2)). In the case of the semiconductors, the Schottky barrier prevents a rapid recombination of excited e^{-} and $h^{\cdot}$ in the metal NP and increases the availability of the charge carriers to participate in subsequent chemical reactions.[37] Generation of kinetically excited charge carriers for indirect transfer processes is in general favored by smaller plasmonic NPs with diameters (d) < 20 nm[102] and strong E-field intensity.[103,104] The efficiency also depends on the imaginary part of the dielectric function of the metal and increases in wavelength ranges where interband transitions are accessible.[105]

LSPR-driven electron transfer can also occur through a direct transfer pathway, in which electrons transfer to a higher lying adsorbate molecular level or semiconductor acceptor band without the prior generation of an excited electron energy distribution in the metal (Fig. 5, process (3)). If the direct electron transfer results in the population of vacant adsorbate molecular levels, it is referred to as Chemical Interface Damping (CID).[38,101,106] The efficiency of CID is proportional to the probability that a surface-scattered electron is transferred to the adsorbate (which depends on its chemical nature), as well as the Fermi velocity, and it is inversely proportional to the effective electron path length, which depends on the size and morphology of the NP.[107–109]

Both direct and indirect charge transfer can drive a variety of photocatalytic processes (Fig. 5, process (4)) for inactivation of microbial pathogens, such as through the generation of ROS or other reactive microbicidal chemicals in aqueous media, which is of high relevance to microbial pathogen inactivation applications. These possibilities are discussed in sections 4.1.1 and 4.1.2.

3.2.3 Photothermal Heating.—Dissipation of photon energy in plasmonic NPs can result in the heating of the metal NPs and the surrounding media.[110–112] In a typical plasmonic thermalization process with pulsed laser excitation of the LSP, the initial pulse prepares an electron gas in a non-equilibrium state. The electron gas thermalizes rapidly into a Fermi-Dirac distribution characterized by an electronic temperature within ~500 fs; this electron thermalization step is followed by a phonon thermalization step, in which the generated hot electrons relax through interaction with phonons of the metal with a time scale of 1–3 ps; finally, a heat diffusion step transfers the energy from the metal into the surrounding medium.[39,111] The three steps can be considered to happen successively when the pulse is short (< 0.1 ns), and/or the NP is small (d < 100 nm). With pulsed illumination, the estimated temperature increase of the NP reaches a maximal value of:[39]

$$\Delta T = \frac{\sigma_{abs} F}{V \rho_m c} \qquad \text{Eq.(9)}$$

where F is the fluence of the laser pulse; σ_{abs}, V, ρ_m and c are the absorption cross-section, volume, mass density and specific heat capacity of the NP, respectively. In the case of continuous-wave (CW) excitation, the temperature increase of the NP can be estimated as:[39]

$$\Delta T = \frac{Q}{\beta 4\pi\kappa_s R_{eq}} = \frac{\sigma_{abs} I}{\beta 4\pi\kappa_s R_{eq}} \qquad \text{Eq.(10)}$$

where Q is the absorbed light power given by the product of σ_{abs} and incident irradiance (I); β is a geometrical correction factor; κ_s is the surrounding medium's thermal conductivity, and R_{eq} is the equivalent NP radius. For spherical NPs, β=1 and R_{eq}=R. It is evident from this equation that small NPs with large absorption cross-sections are potentially more efficient heat sources.

3.2.4 Photonic Responses.—In addition to the light-induced responses described above, the photonic properties of plasmonic NPs can also trigger unique hydrodynamic responses in an aqueous medium, such as nanocavitation and nanocavitation-mediated shockwave generation. It is well-known that tightly focused lasers with sufficient power can induce cavitation through photoionization of the dielectric medium at the focal spot of the laser.[113] Recombination of the formed plasma can trigger a shockwave and initiate cavitation-induced bubble nucleation, followed by an expansion of the bubble and its collapse.[114] Importantly, under pulsed resonant excitation, plasmonic NPs aid the formation of shockwaves (Figure 6). As plasmonic NPs focus the incident light into nanoscale volumes with greatly increased E-field intensities, their presence reduces the incident fluence required for inducing cavitation. In addition to the E-field enhancement, another factor that favors plasma formation around a metal NPs is the optically driven kinetic excitation of the conduction band electrons. If the electronic temperature of the NPs after a pulsed excitation is sufficiently high, for instance, to overcome the work function of ~ 5 eV for 5–75 nm Ag NPs,[115] the hot electrons can be ejected from the metal and increase the free carrier concentration of the plasma until it reaches the threshold of 10^{20}-10^{21} cm^{-3} required for cavitation.[114] The effect of E-field induced shockwave formation is distinct from the thermally induced plasmonic bubble formation mechanisms, in which the heat generated by an irradiated NP results in an evaporation of the surrounding medium.[41,116] The choice of the wavelength and fluence of the incident laser, as well as the E-field enhancement, absorption and thermal emission properties of the NPs are key factors that determine the efficiency of plasmonic shockwave generation.[40,117]

4. Pathogen Inactivation Mechanisms of Plasmonic Nano-Antimicrobials

The optical, photoreactive/catalytic, photothermal and photonic properties of plasmonic nanostructures outlined in section 3 form the basis for multiple light-induced plasmonic microbe inactivation pathways. In addition to these light-driven processes, plasmonic NPs can also have antimicrobial effects that derive from their small sizes or chemical properties independent of the plasmon resonances. When irradiated, light-dependent and -independent mechanisms can coexist and may synergistically enhance the total antimicrobial efficacy of the plasmonic NPs. Some antimicrobial strategies also utilize the plasmonic responses to obtain actively controlled release of microbicides in rational delivery platforms. These three inactivation pathways will be reviewed and discussed in this section.

4.1 Light-Induced Inactivation Pathways

4.1.1 Plasmonic Photodynamic Chemotherapy.—

Plasmonic Photodynamic Chemotherapy (PDCT) involves the use of plasmonic NPs as efficient nanoantenna to generate intense E-fields (see section 3.2.1) for a resonant enhancement of the excitation of photosensitizers, such as tris(bipyridine) Ruthenium(II) ($[Ru(bpy)_3]^{2+}$),[118] rose Bengal (RB),[97,98] toluidine blue O (TBO),[119] hematoporphyrin,[120,121] among others, for ROS production and other microbicidal effect. As shown in Figure 7, PS molecules undergo photoexcitation into a reactive excited state, which can relax *via* multiple charge or energy transfer processes. The plasmonic NPs can significantly enhance the photoexcitation rates of the PSs and thus boost their photoreactivity. One important requirement for an efficient resonant plasmonic enhancement of the photoexcitation process is the spectral overlap between the LSPR and the PS absorption band. Such overlap exists between Ag NPs and $[Ru(bpy)_3]^{2+}$ at 420–450 nm,[118] Ag nanocubes and RB at 480–550 nm,[98] as well as the LSPR of Au NRs and verteporfin at 700 nm.[89] Plasmonic enhancement factors for the absorption between 10 and 35 have been reported in these systems.[93,97,98] This significant enhancement facilitates a reduction of the PS concentration required to achieve an observable microbicidal effect in microbial pathogen inactivation studies from micromolar concentrations in studies using only “free” PSs,[122,123] to nanomolar or even sub-nanomolar concentrations of PS in plasmonic PDCT studies.[84,118,119] This improvement could limit the cytotoxicity and collateral damage caused by the photoreactive PSs to mammal cells in potential *in vivo* applications.[84,124]

One important consequence of the plasmon-enhanced excitation of PSs in aqueous suspensions during PDCT is the generation of ROS, which can induce irreversible structural damage to microbial pathogens and which are molecular drivers of microbial inactivation in the PDCT mechanism. ROS production can be achieved through two distinct sensitized photo-oxidation pathways, known as Type I or Type II reactions (Fig. 7).[125] Type I reactions involve direct one-electron transfer from PS to O_2, and can lead to formation of radicals or radical anions, such as the superoxide anion ($O_2{\cdot}^{-}$).[118,126] The superoxide anion can, in turn, lead to the production of H_2O_2, which is an important precursor of another ROS, hydroxyl radicals (·OH), through the metal -catalyzed Fenton reaction.[127] Type II reactions involve the generation of singlet oxygen ($^1O_2$) through energy transfer from the excited PS to oxygen.[97]

ROS production in PDCT pathogen inactivation studies can be detected directly through photoluminescence measurements.[97,98,128] Heyne and coworkers obtained evidence of plasmon-enhanced ROS formation in hybrid systems that combine Ag nanospheres or nanocubes with RB through measurement of a time-resolved $^1O_2$ luminescence signal at 1275 nm both before and after incubation with bacteria (Fig. 8A).[97,98] The authors observed increased luminescence intensity for the hybrid system (red) compared to an etched control (blue) with no metal core. The generation of $^1O_2$ led to an efficient reduction of the concentration of both Gram-positive and Gram-negative bacteria with an LRV = 6–7 within a period of 2–4 hours of visible illumination. Additionally, ROS production in the plasmonic PDCT mechanism can also be directly probed and quantified through fluorescent sensor dyes, such as singlet oxygen sensor green agent[119,129] and dichlorofluorescin diacetate (DCFDA).[130,131] Kuo *et al.* observed a 13% increase in the fluorescence intensity for a Au NRs-enhanced TBO system labelled with singlet oxygen sensor green agent when compared with free TBO after 2 min of 632 nm illumination (Fig. 8B), indicating an enhancement in ROS production by the plasmonic structure.[119] Importantly, this increase in ROS production led to a 21% increase in inactivation efficacy of MRSA.

The role of ROS in PDCT pathogen inactivation has also been characterized through indirect measurements. One approach is the quantification of the effect of ROS scavengers on plasmonic nano-antimicrobials. For instance, sodium azide (scavenger for $^1O_2$) and Mn(III)tetrakis(4-benzoic acid)porphyrin chloride (MnTBAP) (scavengers for $O_2 \cdot^-$) were observed to reduce the antibacterial effect of a hybrid Ag/$[Ru(bpy)_3]^{2+}$ photoreactor system against Gram-positive bacteria by more than three orders of magnitude (Fig. 8C),[118] which indicated an inactivation through $^1O_2$ and $O_2 \cdot^-$-mediated pathways. Other types of ROS scavengers, such as p-benzoquinone (for $O_2 \cdot^-$), tert-Butanol (for ·OH), L-histidine (for $^1O_2$) and catalase (for peroxides) have also been used for the same purpose.[132–134] The photocatalytic decomposition of dye molecules, such as 9,10-anthracenediylbis(methylene)-dimalonic acid (ABDA),[84,98] represents another effective indicator for singlet oxygen production. ABDA has been used to monitor changes in $^1O_2$ concentration in the presence of plasmonic nano-antimicrobials composed of Au NRs@SiO_2 core-shell nanostructures incorporating indocyanine green (ICG) (Fig. 8D) or verteporfin as PSs under resonant illumination conditions.[84,89] The decrease of ABDA absorbance at 262 nm provided experimental evidence of $^1O_2$ formation.

The ROS produced in PDCT can induce a series of irreversible damages to microbial pathogens, for instance, through peroxidation of cell membrane lipids or cell wall components. Unsaturated membrane components such as sterols and unsaturated lipids are particularly susceptible to lipid peroxidation and can generate cytotoxic peroxidation products, including lipid hydroperoxides, aldehydes, ketones and/or alcohols.[135,136] Simulations performed for different monounsaturated lipid species have shown that peroxidation initiates at the phospholipid head group and then proceeds to the lipid tail within the lipid bilayer.[137] These peroxidation processes can cause major changes in the pathogen membrane morphology, fluidity and permeability,[135,138,139] and negatively affect the structural stability and osmotic pressure of the pathogen membrane. The generated ROS can also induce structural damage to pathogen surface proteins and nucleic acids in the cell interior.[140] All of these factors contribute to the inactivation of microbial pathogens in the PDCT mechanism.

Table 1 summarizes the pathogen types, plasmonic architectures, PSs, illumination conditions as well as LRVs reported in PDCT microbial inactivation studies. PDCT has proven effective for a broad range of bacterial and fungal pathogens. Microbicidal effects with LRVs > 3 have been achieved for both pathogen classes within 1 hour of illumination. The LRVs for Gram-positive bacteria (*Enterococcus faecalis*, *Arthrobacter sp.*, *Staphylococcus epidermidis*) were generally higher than those of Gram-negative species (*E.*

coli, *P. aeruginosa*), and were found to reach LRV = 6–7 within minutes in some cases.[118,120] This systematic difference is consistent with a stronger resilience of Gram-negative species due to the presence of an outer membrane (see section 2.1). Another notable observation is that, with a few exceptions,[97,141] *S. aureus* or the drug-resistant MRSA generally had LRVs below 3 in PDCT studies,[119,121,129,142] lower than for other Gram-positive strains. One possible explanation is that the antioxidant defense mechanisms of various *Staphylococcal* strains, and in particular, MRSA, can reduce the efficacy of PDCT-induced oxidative stress.[143,144] Although PDCT with "free" PSs have been applied for viral inactivation,[145,146] to the best of our knowledge, PDCT has not yet been tested against viruses. Yet we expect that at least for enveloped viruses, PDCT should be an effective inactivation strategy given the susceptibility of the lipid envelope to ROS.

4.1.2 Charge Carrier-Induced Photocatalytic Microbial Pathogen Inactivation.

—The generation of ballistic hot charge carriers from plasmonic nanostructures (see section 3.2.2) is able to initiate photocatalytic reactions that can be utilized in a diverse range of applications, such as in organic photosynthetic reactions[149] and for energy conversion and storage applications.[99,150] Relevant in the context of the current review is the demonstration of a charge carrier-induced plasmonic photocatalytic (PC) inactivation of a series of microbial pathogens. The reported studies for PC inactivation were performed either with plasmonic NPs only, or with heterostructures containing both plasmonic and semiconductor components. For the former case, facile photocatalytic production of e^- and $h^\cdot$ by Ag and Au NPs has been reported to inactivate Gram-negative bacteria, *P. aeruginosa* and *E. coli*.[151,152] Hot carrier PC inactivation with only plasmonic NPs suffers, however, from a rapid recombination of charge carriers within the NPs. Recombination typically occurs much faster than any photocatalytic reactions of the hot carriers, and the lifetimes (τ) of photoinduced hot electrons are inversely related to the size of the NPs. A relaxation time of τ = 1–2 ps has been observed for Au NPs with a diameter of d = 3.5 nm,[153] whereas for larger NPs (d= 15–25 nm) simulations predict τ = 0.1–1 ps.[102]

One strategy to overcome the rapid recombination of photo-induced charge carriers in the metal NPs is to separate them over a Schottky barrier in metal-semiconductor heterostructures (Fig. 5). Due to their spatial separation, the reactive charge carriers can then exist long enough to induce chemical reactions that result in the inactivation of microbial pathogens. Bian *et al.* measured lifetimes of τ = 10 ns for excited electrons produced in Au/mesocrystalline TiO_2.[154] In a more extreme case where photogenerated electrons were trapped in oxygen vacancies of a Au/TiO_2 system, τ up to a few minutes were measured.[155] Strong and rapid microbial pathogen inactivation was observed for plasmonic Schottky junctions. Liga *et al.* reported LRV = 7 for bacteriophage MS2 irradiated in the presence of Ag/TiO_2 hybrid structures within 2 min.[156] The hybrid structure achieved an almost 5 orders-of-magnitude improvement in bacteriophage inactivation over the TiO_2 nanostructures without metallic component. Plasmon-driven charge separation across Schottky junctions in metal-semiconductor heterostructures can also facilitate the inactivation of microbial pathogens at much longer wavelengths than is possible for wide-bandgap semiconductor components alone. For instance, efficient visible light pathogen inactivation was achieved with Ag/TiO_2,[132,156,157] or Ag/ZnO[158–160] heterostructures, complementing the intrinsic UV response of the wide-bandgap semiconductors. When semiconductors with visible light response were hybridized with plasmonic components, the resulting heterostructures achieved a broadband response, covering almost the entire visible range of the electromagnetic spectrum.[25,131,161,162] Broad absorption bands in the visible are particular useful as they can enable microbial pathogen inactivation with ambient light.

In addition to heterostructures comprising plasmonic nanomaterials and inorganic semiconductors, combinations of noble metal NPs with carbon-based conductors have also been explored for microbial pathogen inactivation. Xin *et al.*[163] and Shi *et al.*[164] achieved the coupling of Ag NPs to reduced graphene oxide (rGO) and carbon nanotubes (CNTs), respectively, to engineer enhanced charge transfer and separation. Due to their excellent photocatalytic properties, these hybrid materials achieved an efficient inactivation of *E. coli* with LRVs = 6–8 within tens of minutes of visible light illumination from a Xe lamp. As summarized in Table 2, in general, Schottky junction or other heterostructure-based systems achieve stronger microbial PC inactivation effects (LRVs > 5) than individual metal NPs (LRVs = 1–2). This can be attributed to (1.) the coexistence of intrinsic photocatalytic performances of the individual components as well as synergistic effects facilitated by the heterostructures; and (2.) the extended lifetimes of the generated reactive charge carriers and the resulting higher and more versatile photocatalytic reactivity sustained by the heterojunctions.

The excited e^- and $h^{\cdot}$ produced in the PC inactivation mechanism can generate various redox products through reactions with water, oxygen or other compounds of the ambient medium. Similar as in PDCT, pathogen inactivation through PC can involve ROS generated by a Type I direct charge transfer process, such as the electron-mediated reduction of O_2 into $O_2{\cdot}^-$ or the hole-mediated oxidation of hydroxides to form ·OH.[159,162] ROS formation through charge transfer-mediated PC mechanisms has been confirmed through photoluminescence spectroscopy[158,163] or with ROS probe molecules.[161,162] For instance, 5,5-dimethyl-1-pyrroline-N-oxide (DMPO) has been used as a radical trapper for $O_2{\cdot}^-$ generated from a Ag NPs/graphitic-C_3N_4 system through Type I charge transfer to oxygen.[161] Six signature peaks of the DMPO-$O_2{\cdot}^-$ adduct were detected through Electron Paramagnetic Resonance (EPR). Nitroblue tetrazolium and p-phthalic acid have also been used to monitor ROS production through UV-vis absorption spectroscopy,[162] as reactions of both compounds with ROS leads to a decrease in their respective optical absorption signatures. ROS generated by plasmonic nanostructures through the PC pathway are highly reactive and cause irreversible structural damage to bacterial and fungal membranes, cell walls or intracellular components,[158] as well as to viral envelopes, capsid protein structures and/or nucleic acids.[156]

Hot holes generated by irradiated plasmonic nanostructures through the PC pathway can react with other molecules than water, oxygen, or hydroxide anions to generate additional reactive species with antimicrobial effect. Hou *et al.* demonstrated the formation of reactive Br^0 through oxidation of bromide ($Br^- + h^{\cdot} \rightarrow Br^0$) and observed successful *E. coli* inactivation in a Ag/AgBr/TiO_2 system.[132] The authors reported LRV = 7 for *E. coli* after 110 min white light illumination with an applied bias of 0.6 V (*vs.* Saturated Calomel Electrode). This bias was unable to drive the bacteria inactivation on its own, but it facilitated a hot hole-mediated oxidative process and contributed to a higher inactivation efficiency for the hybrid system. In a different study, hot holes were also reported to oxidize Ag to Ag^+ for subsequent ion release and inactivation of bacteria.[131]

The work performed so far has shown that PC inactivation is efficient for a broad range of microbes, including Gram-positive[131,165] and - negative[132,158] bacteria, non-enveloped viruses,[90,91,156] and fungi[166], achieving high LRVs (>6) for all of these pathogen types (Table 2). This pan-microbial effect can be attributed to the robustness of the photocatalytic inactivation process, especially for heterostructure-based systems. Although in some cases PC achieves LRVs of several orders of magnitude within minutes, in general, the treatment time to achieve a particular level of microbial inactivation is longer for PC than for PDCT. The difference in required treatment time may be attributed to several factors. The plasmon-enhanced photoexcitation of molecular PSs in PDCT could generally occur faster and are more efficient than the charge carrier excitation and transfer in PC. The larger size of the reactive centers in semiconductor-metal heterostructures when compared to molecular PSs-based hybrid systems could also contribute to a less efficient ROS generation due to the smaller specific surface area, slower diffusion and lower charge localization. Another potential drawback of the PC approach, in particular when metal-semiconductor heterostructures are used, is a lower level of control over the onset of the inactivation process, as several studies reported LRVs of 1–2 for these structures against bacterial pathogens even in the dark.[159,167] This light-independent inactivation is related to the ground-state reactivity of the materials, and is likely to cause collateral damage to healthy cells in potential *in vivo* therapeutic applications.

4.1.3 Photonic Shockwave Inactivation of Microbial Pathogens with Femtosecond Pulsed Lasers.—

Femtosecond (fs) pulsed laser treatment is an emerging sterilization technology which has been determined effective against a broad range of microbial pathogen types.[168–171] Tsen and co-workers who performed many of the early benchmark studies attributed the inactivation to an impulsive stimulated Raman scattering (ISRS) process.[168,172,173] Practical challenges for the photonic microbial inactivation through fs-pulsed laser irradiation include the need for high fluences, especially for operational wavelengths in the NIR. The fs-pulsed laser inactivation studies performed with NIR illuminations so far used laser power densities ranging from hundreds of MW/cm^2 to tens of GW/cm^2 and typically required long exposure times on the order of an hour or longer.[172,173] Pulsed laser irradiation in the UV can mitigate the need for long exposure times for some pathogen types.[170,171,174] The increased inactivation efficacy with fs-pulsed UV lasers can be attributed to the UV-driven photochemistry on the surface of or inside microbial pathogens. The exposure of biological samples to high energy UV photons can, however, also be problematic in some applications, since important groups of biomolecules (DNA, RNA, and proteins) have electronic absorption bands in the UV. Irradiation of biological samples with high energy photons creates a high risk for collateral photo-damages.

The antimicrobial effect of fs-pulsed NIR lasers, whose photon energy does not overlap with molecular absorptions, is generally weak without any plasmonic enhancement. At sub-GW/cm^2 laser power densities, NIR lasers barely induced any noticeable inactivation effect on either murine leukemia virus (MLV) or non-enveloped bacteriophage ϕX174 (Fig. 9A, B).[42,86,172] Even for high power densities > 100 GW/cm^2, the inactivation of ϕX174 was still very low at long illumination times of 120 min.[86] However, their antimicrobial efficacy can be significantly increased in the presence of resonant plasmonic NPs. Au NRs and Ag-coated Au bipyramids (BPs) with plasmon resonances in the NIR irradiated with fs-pulsed 800 nm light were highly effective against Gram-positive and Gram-negative bacteria, mollicute bacteria, as well as enveloped and non-enveloped viruses.[86] The plasmon enhanced fs-pulsed irradiation technique was successfully tested against MLV (LRV = 3.7 within 10s, Fig. 9A), bacteriophage ϕX174 (LRV > 7 within 1 min with BPs, Fig. 9B), *E.coli* (LRV > 4 within 30 min), *Bacillus subtilis* (LRV = 3 within 20 min), and *Acholeplasma laidlawii* (LRV = 6.7 within 30 min). Importantly, a non-resonant illumination of plasmonic NPs controls barely yielded any inactivation, which confirms a strong wavelength dependence of the photonic inactivation process.[42,86]

The significant gain in inactivation for fs-pulsed NIR irradiation in the presence of resonant plasmonic NPs has been attributed to a plasmon-enhanced generation of shockwaves.[41,114] As introduced in section 3.2.4, the efficient nanolens properties of plasmonic NPs reduce the fluence threshold required for laser-induced cavitation and shockwave generation.[40,42] Several experimental observations made in fs-pulsed NIR pathogen inactivation studies that were successfully enhanced by plasmonic NPs support the model of a shockwave-mediated microbe inactivation mechanism. First of all, the detection of ultrasonic waves (Fig. 9C),[42] and fs-laser illumination-induced bubble formation (Fig 9D, see also supplemental video 1) are direct indications of laser-induced cavitation. Secondly, structural damage to the pathogens after pulsed laser inactivation with plasmonic NPs were observed, including the perforation and fragmentation of ϕX174 virus particles.[174] In the case of MLV, structural damage to the viral envelope resulted in a loss in viral fusion capability and infectivity.[42] These observations point toward a significant mechanical force as provided by a shockwave mechanism. Furthermore, some experimental findings indicate that a direct contact between NPs and pathogens is not necessary for an effective plasmonic enhancement of fs-pulsed pathogen inactivation, suggesting a remote interaction mechanism as in the case of a shockwave.[42] Lastly, scavenger experiments revealed that ROS, which play a central role in PDCT and PC inactivation mechanisms, do not account for the observed pathogen inactivation observed for pulsed lasers in the presence of resonant NPs.[42]

The antimicrobial effect of the plasmon-enhanced photonic inactivation approach is particularly impressive considering that the same experimental conditions did not induce a measurable decrease in the viability of mammalian cells (Chinese hamster ovary cells, CHO) (Fig. 9E), or cause structural damage to monoclonal antibodies as indicated by comparable absorption spectra before and after illumination (Fig. 9F).[86] This selectivity was attributed to a high frequency (*i.e.* short wavelength) cut-off frequency defined by the NP size. The effective wavelength associated with the cut-off frequency can be engineered to be larger than the physical dimensions of molecules and biologics, leading to a small local gradient, and producing only small forces for objects (molecules, NPs, biologics) smaller than the threshold wavelength. For larger mammalian cells with typical sizes of tens of microns, the shear force associated with the shockwave distributes over a larger area, diminishing its effect. Many microbes (virus, yeast and bacteria cells), however, lie in the size range between approximately 20 – 1000 nm, in which shockwaves can be expected to be particularly effective.

4.1.4 Plasmonic Photothermal Inactivation.—

Photothermal therapy is a commonly used strategy for localized inactivation of cancer cells in a tumor[175,176] as well as for the inactivation of bacteria and other pathogen species. Pathogenic bacteria are usually mesophilic and can thrive between 33–41 °C.[177] Higher temperatures can induce the denaturation of proteins and inhibition of cellular functions.[112] Bacterial and fungal spores are able to endure higher temperatures.[65,66] Viruses, in particular non-enveloped viruses, can also be more resilient to heat-induced inactivation than bacteria, occasionally requiring temperatures up to 60 – 95 °C for effective (LRVs > 3) inactivation.[178] Photothermal heating of plasmonic NPs and their immediate environment to temperatures above the thresholds that induces microbial pathogen inactivation provides a light-controlled strategy of plasmonic photothermal (PPT) sterilization (Table 3). PPT inactivation has been demonstrated to be particularly effective against bacteria, such as *E. coli*, *S. aureus* and MRSA, reaching LRVs > 7 in some cases for both CW visible illumination and pulsed laser illumination.[179–181] Although PPT inactivation has also been demonstrated for heat-resistant bacteria, such as *B. subtilis* or thermophilic *Exiguobacterium*,[182] and non-enveloped viruses, like bacteriophages MS2 and PR772,[134,183] the overall efficiency of inactivation is much lower in these cases.

Various types of plasmonic metals, including Au[134,179,182–185] and Ag[180,186,187] with distinct shapes and sizes have been used to achieve enhanced PPT heating. The large absorption cross-sections of the plasmonic NPs effectively increased the absorbed heat power (Q) and enhanced the antimicrobial effect in these studies (see Eq. (9), (10)). An increased specific surface area of the plasmonic NPs can also be beneficial, as it leads to more efficient thermalization of the ambient medium. Zheng and colleagues designed two-dimensional Pd@Ag nanosheets for efficient NIR-induced heating and PPT inactivation.[87] 10 min irradiation of the nanosheets with 808 nm laser led to an increase in temperature by 19 °C in the ambient medium as well as an efficient release of bactericidal Ag^+, resulting in a complete killing of *S. aureus* and *E. coli* at 10^7 CFUs/mL. In another work, Quidant and coworkers achieved efficient PPT heating and inactivation of *S. aureus* biofilms grown on surgical meshes that were coated with citrate-stabilized Au NRs.[67] After illumination with a 810 nm CW laser (0.435 W/cm^2) for seconds, a temperature increase of 150 K/(W/cm^2) was achieved. The authors monitored the biofilm inactivation process through fluorescence imaging of bacteria stained with a live/dead viability staining kit. The recorded confocal images confirm that the laser illumination leads to a decrease in viable (green) cells and an increase in dead (red) cells (Fig. 10 A–D). A quantitative analysis revealed a LRV = 1–2 for *S. aureus* at the mesh surfaces after treatment (Fig. 10E). Considering the high resilience of biofilms against conventional microbicides, PPT inactivation strategy shows potential as sterilization strategy for surgical implants.

Engineering plasmonic nano-antimicrobials with different shapes can also broaden the absorption band and facilitate efficient PPT heating by a wider range of excitation wavelengths. Poletti *et al.* designed Au nanocorals that sustain large absorption and photothermal responses from the visible region of the spectrum (568 nm) to the NIR (1000 nm).[88] A temperature increase of 15 °C was measured for different lasers in aqueous suspensions. Porous nanostructures have also been found useful for tuning both optical and PPT properties.[181,182] Nanoporous Au nanodisks were shown to possess LSPRs in the NIR and to provide larger absorption cross-sections and broader peak widths (Full Width at Half Maxima, FWHM ≈ 400 nm) than non-porous Au NPs.[182] The porous Au nanodisks achieved a temperature increase of 75 °C on glass upon CW NIR laser illumination, which resulted in a LRV = 1–2 within 30 seconds for various bacteria. PPT effects obtained for on *versus* off-resonance excitation have been compared in a study with DNA aptamer-functionalized spherical Au NPs (LSPR in the green) and Au NRs (longitudinal LSPR in the NIR) using 808 nm CW laser illumination with a power density of 1.1 W/cm^2.[184] The resonant excitation in case of 1 nM Au NRs achieved a temperature increase of 29.8 °C in an aqueous PBS suspension after illumination for 2 min, which exceeded the temperature change induced by the same concentration of nanospheres by more than 20 °C. Notably, Au NRs provided an efficient inactivation of MRSA (LRV = 1–2) after 2 min. In contrast, spherical Au NPs achieved almost no decrease in CFUs.[184] These measurements confirm that an efficient PPT effect requires a resonant excitation of the LSP.

Nanocomposites formed between plasmonic metals and broadband absorbers is another commonly used strategy to boost PPT efficiencies. The NIR light-response and photothermal effect of rGO was reported by Dai and coworkers in 2011.[175] The combination of rGO with NIR-responsive plasmonic metals, such as Au NRs, can increase light absorption and heating efficiency. Szunerits and coworkers conjugated rGO through polyethylene glycol (PEG) chains to Au NRs and demonstrated an increase in temperature of 49 °C with pulsed laser illumination.[179] The authors achieved LRV = 7 for *E.coli* in only 10 min of illumination. Ag NPs have also been composited with rGO for antibacterial applications.[180,187] Although the temperature increase in both cases were lower than for Au/rGO, efficient sterilization was still observed after visible light inactivation for a longer period of time (LRV = 7 for *E. coli* after 30 min).[187] Other carbon-based absorbers, such as carbon black, have also been used in combination with plasmonic metals.[134,183] An increase in temperature of > 18 °C was observed for a Au NRs-carbon black composite after 30 min of illumination with a sunlight simulator. This temperature increase achieved an efficient inactivation of both bacteria (*E. coli*, LRV = 5) and viruses (bacteriophages, LRV > 1.3), and facilitated the implementation of a flow-through photothermal reactor for water purification.

4.1.5 Comparison of Light-Induced Inactivation Mechanisms of Plasmonic Nano-Antimicrobials.—

All four light-induced inactivation mechanisms reviewed in this manuscript, PDCT, PC, photonic shockwave, and PPT inactivation, have shown antimicrobial efficacy against at least two classes of pathogens. This pan-microbial efficacy is desirable for many applications as it facilitates the simultaneous inactivation of multiple pathogens. Intriguingly, the photonic inactivation strategy based on fs-pulsed irradiation of plasmonic NPs demonstrated the broadest effect against different pathogen types,[42,86] while at the same time it generated no detectable collateral damage to mammalian (CHO) cells or antibodies as selected biologics, presumably due to a size-selectivity of the underlying shockwave inactivation mechanism.[86] This selectivity could pave a path to new broadband sterilization technologies with minimal collateral damage to biologics and mammalian cells.

It is challenging to achieve the same level of selectivity with PDCT, PC and PPT mechanisms, since these pathways rely on the generation of reactive species or hyperthermia, which can affect pathogens and healthy cells alike. The lack of specificity in these approaches can, however, be mitigated to some degree by an active targeting of the plasmonic NPs to microbes in order to localize the effect to the pathogens (see section 5).

Another advantage of the photonic shockwave inactivation strategy is that, compared to other light-induced pathways, it requires relatively short irradiation times. Irradiation times < 1 min have been shown to lead to an efficient inactivation (LRVs > 3) of the tested pathogens. This efficiency forms a promising basis for potential *in vivo* pathogen sterilization applications for the treatment of acute microbial infections. A general drawback of the plasmon-enhanced shockwave inactivation strategy is, however, the requirement of fs-pulsed NIR lasers, whereas PDCT and PC can be implemented with lower power visible light sources, which makes them more readily applicable in on-demand sterilization applications with low power consumption and potentially utilizing ambient sunlight.

One feature that all light-dependent inactivation pathways have in common is that they can cause significant structural damage to microbial pathogens. ROS or other reactive species associated with PDCT or carrier-induced PC pathways lead to damages of bacterial cell wall components as well as of cytoplasmic membrane lipids and sterols, and thus cause changes to the surface morphology of these pathogens.[129,140,158] The high reactivity associated with the generated reactive species can result in a perforation of the cell surface after relatively short inactivation times of a few minutes by low-power CW illumination sources (Fig. 11A, B),[118,167] whereas a complete rupture of the pathogen is possible with longer illumination times under similar illumination conditions (Fig. 11C).[165] Likewise, fs-pulsed irradiation of NPs can cause detectable structural damage in viruses.[42,86,174] In the case of enveloped viruses, structural damage to bacteriophages and MLV particles has been detected by dynamic light scattering measurements and nanopore measurements,[174] as well as by TEM micrographs after photonic shockwave inactivation (Fig. 11D).[42]

Since plasmonic NPs can simultaneously develop multiple antimicrobial photophysical responses, “multimodal” inactivation pathways are possible in which multiple responses co-exist and potentially sustain mutual enhancement. For instance, as energy dissipation can lead to both increased temperature and hot electron generation, PPT and PC pathways can co-exist. This has been demonstrated in metal/semiconductor heterostructures.[181,186] Similarly, PDCT and PPT can coexist in metal/photosensitizer systems.[89,119,129,139,190] The rapid (10 min to 1 hour) and effective (LRVs>3) inactivation associated with the coexistence of multiple inactivation mechanisms demonstrated in previous studies justifies the interest in multimodal inactivation approaches for maximizing the efficiency of microbe inactivation.

4.2 Light-Independent Inactivation Pathways

Plasmonic nano-antimicrobials can also affect microbes and microbial infections through light-independent mechanisms. This is because plasmonic NPs can have additional non-plasmonic antimicrobial effects that derive either from their nanoscale size, surface charge and surface affinity, or from light-independent chemical reactivity. These processes can occur separately, collectively, or in combination with light-induced pathways for a synergistic gain in inactivation efficacy.

The best-known light-independent antimicrobial effect is the wound-healing effect of Ag, which can be traced back to Hippocrates 400 B.C..[191] In more recent times, additional modes of light-independent microbe inactivation have been proposed for Ag and other plasmonic nanostructures (Fig. 12A).[5,192] Firstly, the binding of NPs to pathogens surface components through covalent, van der Waals, electrostatic interactions, and/or hydrogen bonding can perturb important microbial functionalities. Ag and Au NPs can bind to thiol-containing surface proteins, such as surface sensor proteins, and disrupt disulfide bonds and damage cellular binding and sensing functionalities on pathogen surfaces.[191] Ag NP binding to cysteine residues in the envelope glycoprotein gp120 of HIV-1 has been observed to block gp120/CD4-mediated virion binding, fusion and infection.[193] It was demonstrated that Ag NPs achieve a high percentage of fusion inhibition between HIV-1 envelope protein expressing cells and CD4-presenting cells (Fig. 12B). In comparison, the well-known antiretroviral drugs UC781, AZT and Indinavir, did not inhibit fusion in this cell-based fusion mimicking assay.[193] In another work, Broglie *et al.* also attributed the inactivation of non-enveloped norovirus by Au/CuS core/shell NPs to the binding of the NPs to the viral protein capsid.[194]

Plasmonic nano-antimicrobials with rationally engineered surface ligands can target important pathogen surface functions. Adhikari *et al.* used polythiophene-conjugated Au NPs (AuNP-PTh) for targeting Gram-negative bacteria species and to induce damage to the outer cell membranes.[195] Loss in membrane polarization and membrane damage were observed in this work for *E. coli* after treatment with AuNP-PTh, as indicated by a membrane potential-sensitive probe. The AuNP-PTh-induced membrane permeability facilitated a synergistic enhancement of the antibacterial effect of the hydrophobic antibiotic erythromycin and led to an effective inhibition of the growth of both planktonic bacteria and biofilms.[195] Stellacci and coworkers utilized thiolated mercapto-undecanesulfonic acid (MUS)-capped Au NPs to mimic viral attachment ligands based on heparan sulfate proteoglycans (HSPG) (Fig. 12C).[196] Compared to known HSPG-mimicking linkers such as 3-mercaptoethylsulfonate (MES), MUS are longer and can sustain multivalent binding. The MUS-functionalized Au NPs exhibit high binding affinity and, importantly, strong non-reversible MUS-Au NP binding was demonstrated to cause local deformations of the viral capsid. MUS-Au NPs were effective in preventing the initial step of virus-cell binding for both enveloped and non-enveloped viruses that rely on HSPG as viral attachment factor.[196] Other capping ligands, such as thiolated amino-substituted pyrimidines, have been shown to induce membrane damage to Gram-negative bacteria by perturbing Mg^{2+} chelation and sequestration.[197]

Surface charge-mediated electrostatic interactions represent another mode of pathogen binding by plasmonic NPs. The charge of the NPs is an important factor that influences the mechanism by which NPs can cross cell walls and membranes. Membrane reflectivity profile characterizations indicate that positively capped Au NPs are more likely to penetrate zwitterionic artificial bilayer lipid membranes than negatively capped Au NPs.[198] The surface charge of Au NPs has also been shown to affect the Gram-selectivity in bacteria inactivation. Grzybowski and coworkers explored the effect of different ratios of positively and negatively-charged surface ligands on the antibacterial efficacy of Au NPs.[199] The authors demonstrated that Au NPs capped with a higher ratio of positively-charged ligands are more effective against Gram-negative bacteria, whose surfaces are considered more negatively charged due to the presence of lipopolysaccharides and phospholipids in bacterial membranes.[62] NPs capped with a higher ratio of negatively-charged ligands were found to favor interactions with and inactivation of Gram-positive bacteria (Fig. 12D).

Detrimental interactions between NPs and pathogens are not limited to surfaces, as NPs, especially those with small diameter, can enter pathogens under some conditions. For instance, Ag NPs with diameters between 1–10 nm were demonstrated to enter bacterial cells where they can bind to and perturb intracellular components due to their high specific surface area and surface charge.[200]

One other notable property of plasmonic metal nanostructures, particularly those from Ag, is cation release through oxidative dissolution. Release of Ag^+ from Ag NPs usually occurs in two steps: (1.) formation of an oxide layer upon interaction with O_2 or H_2O; and (2.) cation dissolution into the aqueous phase when the oxide layer interacts with protons.[201] Oxidative dissolution is spontaneous and can occur without any photoexcitation. Although the kinetics of this process is slow in neutral pH, it can be accelerated by photocatalysts,[131,132] or other factors such as irradiation, lower pH, elevated temperatures, or applied voltage.[87,118,201] Other plasmonic metals, such as Cu and Al and even Au, have also been observed to release cations into the aqueous solution under specific conditions.[128,202–204] The released cations can directly bind to pathogen surface components and cause surface structural damage to the microbial pathogens.[194,205,206] Due to their relatively small ionic radii, metal cations, such as Ag^+ and Cu^{2+}, can enter bacterial cells through porins[207] and perturb intracellular processes, for instance, by denaturing enzymes and proteins. Metal cations have also been found to synergistically interact with other antibacterial agents, such as molecular antibiotics. Morones-Ramirez *et al.* demonstrated that Ag^+ enhances the effectiveness of the antibiotic vancomycin for sterilizing Gram-negative bacteria by increasing the membrane permeability.[191]

The light-independent ground-state chemical reactivity of $M(0)$-M^{n+} redox pairs can induce oxidative stress in pathogens through formation of reactive species, such as ROS and $SO_4{\cdot}^-$. These species can cause structural damage on the surface as well as in the interior of pathogens.[140,194,204,208,209] ROS formation associated with Ag NP binding to Gram-negative bacteria strains of *E. coli* and *P. aeruginosa* was found to damage the bacterial cell membrane, as indicated by a reduced negative surface charge of the bacteria.[208] These damages can lead to an increase in membrane permeability and leakage of cell contents and impede normal cell metabolomic functions, such as ion uptake and osmosis. Eventually, these effects can result in bacterial cell death.[206–208,210]

One important challenge associated with light-independent pathways of plasmonic NPs that involve M^{n+}-associated mechanisms is the development of microbial metal resistances. Upregulation of various antioxidant genes as well as metal transport, metal reduction and ATPase pumps-encoding genes have been observed in *E. coli* after treatment with Ag^+

released from Ag NPs embedded in a zeolite membrane.[211] Increase in antioxidant enzyme activity, for instance by catalases, and metal cation-reducing capability were also recorded in MRSA after Ag^+ treatment.[210]

4.3 Plasmonic Nano-Antimicrobials for Delivery and Controlled Release of Microbicides

Plasmonic nanostructures and composite structures containing plasmonic NPs also represent effective nanocarriers for antimicrobial drugs or biologics. Various composite structures based on plasmonic NPs and polymers,[19,212] lipid,[118,213] core-shell,[214,215] or MOF[15] architectures have been designed to achieve an efficient loading with and delivery of antimicrobials. It is, therefore, conceivable to enhance the antimicrobial function of plasmonic nano-antimicrobials with microbicides contained in and released from the NPs. Importantly, the photocatalytic and photothermal properties of plasmonic NPs discussed above in the context of microbe inactivation can also enable unique mechanisms for controlling the release of antimicrobials from plasmonic NP-based or -containing nanocarriers. The combination of microbicides with plasmonic delivery platforms can enhance the efficacy and selectivity of the antimicrobial effect of both components, and potentially minimize “collateral damage” to healthy cells in *in vivo* applications.

Plasmonic nano-antimicrobials have been combined with conventional molecular antibiotics for bacteria inactivation applications. In these studies, the plasmonic NPs not only served as carriers for delivery of antibiotics, but also enhanced the antibacterial effect of the antibiotics.[191,195,216,217] Detailed analyses revealed that the gain in efficacy in these studies arises primarily from an increase of bacterial membrane permeability caused by metal NP or cation binding. Wang *et al.*[214] and Song *et al.*[215] used mesoporous silica NPs (MSNs) with Ag cores as carriers for levofloxacin (LEVO), a common antibiotics that functions through inhibition of DNA gyrase and topoisomerase IV. Spontaneous release of LEVO and Ag^+ from the NPs achieved an efficient inactivation of drug-resistant *E. coli* both *in vitro* and *in vivo* due to the Ag^+-mediated increase in cell membrane permeability that enhanced uptake of LEVO. Importantly, Wang *et al.* demonstrated an effective *in vivo* treatment of *E. coli*-induced peritoneal infection in mice (Fig. 13A).[214] Mice treated with Ag NP cores@MSNs@LEVO at concentrations of 160 μg/mL or above demonstrated the highest survival rate compared to control groups (Fig. 13B, C), as well as a much reduced bacteria load (LRV = 3) in the peritoneal cavity after 72 hours of treatment (Fig. 13D). Hematoxylin-eosin (H&E) staining tests performed on the spleen and peritoneum of infected mice showed enlarged lymphoid nodules (yellow arrows) and inflammatory cells (green arrows) after infection. Both features diminished and dropped to normal levels within 72 hours after treatment with Ag@MSNs@LEVO (Fig. 13E).

In a different work, Webster and colleagues synthesized a methoxypoly(ethylene glycol)-poly(D)-(L)-lactic acid (mPEG-PDLLA) diblock copolymer polymersome embedding Ag NPs in the hydrophobic regions and ampicillin in the hydrophilic region for the inactivation of genetically-modified ampicillin-resistant *E. coli* (Fig. 14A).[212] The authors found that the Ag NP-polymersomes engage in hydrophobic interactions with the outer cell membrane of *E. coli*, which results in Ag NP-induced bacterial membrane damage and disabling of drug-resistance mechanisms based on membrane barrier effects or efflux pumps.

The versatile photophysical properties of plasmonic nanostructures enable unique mechanisms for controlling the microbicide release from plasmonic NP-based carriers. E-field-enhanced photoreactivity, for instance, represents one strategy of visible light-induced release. A hybrid plasmonic photoreactor design containing photosensitizer $[Ru(bpy)_3]^{2+}$ integrated into a membrane around a Ag NP core has been proposed as E-field-enhanced nano-antimicrobials (Fig. 14B).[118] The hybrid photoreactors facilitate a light-controlled photoreactive release of Ag^+ and $[Ru(bpy)_3]^{2+}$ to inactivate both Gram-positive and -negative bacteria through PDCT and light-independent Ag^+ reactivity. The photoreactors were shown to be biocompatible and possess no observable inactivation effect in dark. Visible light illumination triggers, however, the plasmon-enhanced photoreactivity of $[Ru(bpy)_3]^{2+}$, initiates the generation of ROS and induces the peroxidation of the photoreactor lipid architecture. These processes led to a permeabilization of the lipid membrane around the Ag NP (Fig. 14C) and resulted in the release of both Ag^+ and $[Ru(bpy)_3]^{2+}$ into the surrounding medium, where they can synergistically interact to inactivate bacteria. Importantly, the rate of release of reactive compounds from the hybrid NPs was shown to depend on the composition of the lipid architecture. A higher concentration of unsaturated lipids or cholesterol in the Ag NP encapsulating membrane favored membrane peroxidation and a higher rate of cation release (Fig. 14D). This plasmonic photoreactor concept was demonstrated to achieve LRVs > 7 for Gram-positive *Arthrobacter sp.* (Fig. 14E) and LRV ≈ 4 for Gram-negative *E. coli* after 1 hour of low power (9.76 mW/cm^2) visible light illumination. Importantly, this hybrid system also achieved an effective inactivation of *Arthrobacter sp.* biofilms.

Controlled release has also been initiated in some cases by pathogen-induced chemical signals. Zhang and colleagues designed a bacterial toxin-triggered bactericide release pathway from vancomycin-encapsulated liposomes decorated with chitosan-modified Au NPs.[213] The chitosan-Au NPs effectively prevented the fusion of liposomes and undesirable release of loaded vancomycin in the absence of bacteria. However, in the presence of bacteria, the secreted bacterial toxin inserted into the liposome to form pores that led to the release of antibacterial drug for an effective inactivation of MRSA. Another effective pathogen-induced release pathway involves secretion of hyaluronidase (Hyase) by bacteria and the resulting selective degradation of HA scaffolds assembled around NPs in close vicinity of a bacterial target. To exploit this effect, a Ag-infused PCN-224 MOF architecture with HA coating (PCN-224-Ag-HA) was designed for the inactivation of MRSA (Fig. 14F).[15] In the absence of the bacteria target, the negatively-charged HA prevents release of the cation, whereas damage to the HA coat layer induced by Hyase initiates release of microbicidal Ag^+, as indicated by Inductively Coupled Plasma - Optical Emission Spectrometry (ICP-OES) measurements (Fig. 14G). The PCN-224-Ag-HA architecture achieved an efficient inactivation of MRSA *in vitro* after visible light illumination with a halogen lamp for 15 min (Fig. 14H). The NPs also demonstrated an effective healing of MRSA infected wounds in mice.

5. Plasmonic Nano-Antimicrobial-Enabled Pathogen Sensing for Diagnostic and Theranostic Applications

The large optical cross-sections and E-field localizing properties of plasmonic NPs facilitate new microbe inactivation strategies, and can, at the same time, be utilized for enhancing pathogen imaging and sensing capabilities. The possibilities to enhance optical microscopy and spectroscopy in the vicinity of plasmonic NPs and to use the strong optical signal of the NP plasmon as transducers provide sensitive microbe detection and quantification modalities. These pathogen sensing modalities cover a broad range of microbe species, and are typically fast, sensitive and non-invasive. They generally require little or no sample preparations and rely on signal amplification mechanisms rather than sample amplification. These approaches represent important alternatives to conventional detection and quantification strategies for microbial pathogens or their components, such as enzyme-linked immunosorbent assay (ELISA) and quantitative polymerase chain reaction (qPCR).[218,219] Sensitive detection modalities that are selective, easy and fast facilitate an early detection of pathogen contaminants in food and water and on surfaces, and can thus make an important contribution to preventing dangerous infections. Furthermore, the ability to simultaneously detect, quantify and inactivate microbes with plasmonic NPs paves the path to targeted therapeutic or theranostic applications of nano-antimicrobials.

5.1 Surface Enhanced Raman Spectroscopy for Pathogen Sensing

Surface Enhanced Raman Spectroscopy (SERS) utilizes the strong E-field-enhancement provided by oligomers or clusters of plasmonic NPs to amplify Raman signal intensities, which scale with the fourth power of the E-field.[36,51,220] Tip-Enhanced Raman Spectroscopy (TERS) is a special form of SERS which rasters an E-field enhancing probe over a sample of interest using an Atomic Force Microscope. This approach achieves a local enhancement of Raman scattering intensity and facilitates the acquisition of spatially resolved SERS spectra.[221–223] SERS can be used to characterize the intrinsic vibrational modes of microbes in a label-free manner, or to detect molecular vibrational SERS labels with high signal intensities and spectral precision. In both cases, SERS characterizations and the detection processes are fast and non-invasive.

SERS spectra recorded on nanostructured plasmonic metal substrates have shown great promise for the reliable identification and discrimination of microbial pathogens in a label-free fashion.[50,51,224,225] Premasiri *et al.* discovered strong contributions from metabolites of purine degradation, such as adenine (correlated with *S. aureus* NCTC 8325), hypoxanthine (*E. faecalis* ATCC 29212) and xanthine (*A. baumannii* ATCC 17978) in the SERS spectra of different bacteria.[226] Popp and colleagues also utilized the plasmonic enhancement provided by Ag colloid-based microfluidic chips for the detection and discrimination of nine *E. coli* strains.[227] However, as the chemical composition of microbial pathogens is complex, specific peaks cannot necessarily be attributed to one molecular group due to a spectral overlap of multiple compounds. Consequently, chemometric data analyses and machine learning methods, such as hierarchical cluster analysis (HCA)[228,229] and principal component analysis (PCA),[50,51,224,230] are commonly used to identify spectral patterns and to identify differences between bacteria samples. These analytical methods have been combined with SERS measurements on colloidal plasmonic NPs,[227,231] aggregated NP films,[229,232] rationally designed Au NP arrays[50,51,233] and Ag cylindrical nanotrough networks[224] for effective detection and discrimination between different types of bacteria. In the latter case, SERS spectra (Fig. 15A) and PCA (Fig. 15B) revealed significant differences in the Raman signatures of (1.) *E. coli* K12 (red) or its derivative DH 5α E (blue) from (2.) a different type of *E. coli* strain BL21 (DE3) (green). Wu *et al.* utilized vancomycin-functionalized Ag NR arrays as SERS substrate for the detection and identification of six food-borne bacterial pathogens in mung bean sprouts samples.[230] The intensity of the ring breathing and N-H wagging mode of adenine as well as a PCA analysis of the bacteria spectra were used to distinguish between different species. The measured peak intensities were utilized to determine the concentrations of pathogens. Limit of Detection (LOD) = 100 CFU/mL was achieved within 4 hours, including the time required to process the food samples and to perform the Raman data acquisition.

A combination of SERS spectroscopy and deep neural network model analyses has been successfully used to assess the bacterial susceptibility to antibiotics.[234] The ability to rapidly differentiate susceptible and resistant bacterial strains is extremely useful for preventing excessive administration of antimicrobial drugs, and for monitoring antimicrobial processes.

Label-free SERS sensing has also been utilized for the detection of bacterial spores. As an example, SERS signatures in the 300–2000 cm^{-1} spectral range were used to detect single optically trapped *Bacillus* spores and to differentiate between two different *Bacillus stearothermophilus* spore strains.[235] TERS in combination with PCA has also been applied for Raman imaging of *B. subtilis* spores.[221] The imaging studies revealed that the spores contain relatively large concentrations of amino acids tyrosine and cysteine.

The spectral fingerprints of different viral[222,225,236] or fungal[237] species have been recorded with regular Raman spectroscopy, SERS or TERS. The Popp group monitored the TERS signatures of tobacco mosaic viruses (TMV) with a spatial resolution of less than 50 nm, allowing acquisition of molecular vibrational information at single virus level.[222] Ray and colleagues demonstrated effective detection of non-enveloped rotavirus[225] and enveloped mosquito-borne flaviviruses,[236] including West Nile virus (WNV) (Fig. 15C) and Dengue virus (DENV) (Fig. 15D), with antibody-conjugated Au NPs. For the flaviviruses, they determined that the amide band at 1680 cm^{-1} and the $-CH_2$ deformation band at 1450 cm^{-1} are unique to WNV, whereas the skeletal mode at 420 cm^{-1} and CH_3 rocking modes at 950 cm^{-1} are unique to DENV. These bands were used for the quantification of the viral particles and an LOD of 10 PFU/ml was achieved.

In addition to utilizing the intrinsic Raman signatures of pathogens for detection and identification, Raman labels like Cy3,[238] malachite green isothiocyanate (MGITC),[231,239] 4-mercaptobenzoic acid (4-MBA),[240] etc. have also been combined with plasmonic NPs to generate highly selective SERS pathogen detection modalities. Multiple molecular recognition mechanisms have been proposed to facilitate the specific binding of Raman labels to pathogens or pathogen-associated molecules. One notable example is the use of nucleotide base pairing between target strands of pathogenic nucleic acids and single-stranded DNA or RNA-modified plasmonic NPs. Mirkin and coworkers utilized complementary base pairing between (1.) single-strand DNA targets, (2.) probe strands conjugated to Ag SERS substrates, and (3.) single-strand nucleic acid modified Au NPs containing a specific Raman tag (Cy3) for target detection *via* SERS.[238] A successful binding event results in the SERS enhancement of the signals from the Raman tag, which can be calibrated to quantify the binding. As nucleic acids define the genetic information that are unique for each pathogen species and strain, this approach provides a basis for an accurate and sensitive detection and identification of pathogens. Li *et al.* designed Ag nanorice cores@MGITC Raman label@SiO_2 shell nanostructures for detection of Hepatitis B Virus (HBV) DNA (Fig. 15E).[239] The composite nanostructures were conjugated to the reporter DNA oligonucleotide, and significant SERS enhancement was achieved through annealing of the MGITC-tagged probe strand to the target strand immobilized on a Au nanoarray. The SERS intensity of the MGITC 1335 cm^{-1} band was monitored and calibrated to achieve a LOD of 50 aM. The high sensitivity of the approach made it possible to distinguish the target DNA from DNA strands with a single base mismatch.

In addition to base-pairing between complementary nucleic acids, other recognition mechanisms based on antibody-antigen binding[240] or formation of coordination bonds[241] were also successfully implemented to bind Raman reporter tags to NPs and to generate a SERS signal. Wang *et al.* utilized boronic acid-containing 4-mercaptophenylboronic acid (4-MPBA)-modified Ag NPs to complex the peptidoglycans in the bacterial cell wall.[241] Both the SERS signatures of 4-MPBA and the intrinsic fingerprints of *E. coli* and *S. aureus* were identified in the recorded SERS spectra. The authors demonstrated a high SERS sensitivity (10^2 CFU/ml) for both species with high reproducibility. Notably, the 4-MPBA-modified Ag NPs also exhibited good antibacterial properties. A reduction of the bacterial load by 97% was demonstrated, which indicates potential for the theranostic treatment of bacterial infections.

5.2 Plasmon-Enhanced Fluorescence for Pathogen Sensing and Targeted Therapeutics

As introduced in section 3.2.1, plasmonic E-field and LDOS enhancement can lead to an increased emission of quantum emitters located in the hot spots around plasmonic nanostructures.[94–96] Such enhancement effects have been exploited for fluorescence (FL) microbial pathogen sensing with a wide range of fluorescent labels, including dye molecules,[94,95,242] fluorescent proteins,[243,244] carbon nanotubes,[245] quantum dots (QDs),[246–248] and others. Similar to SERS sensing with Raman-active tag molecules, plasmon-enhanced FL sensing requires the combination of the plasmon-enhanced transducer with a molecular recognition element to generate a functional sensor. Recognition strategies such as electrostatic interaction,[249] nucleic acids base pairing,[242] as well as antibody[245,250] or other forms of protein binding[244,248] have been applied, and sensing of various bacteria and virus species were achieved with LODs ranging between 10 – 100 CFUs/mL or PFUs/mL. E. Y. Park and coworkers designed immunofluorescence sensors based on antigen-antibodies interactions.[250] The authors achieved a selective co-binding of CdSeTeS QDs and Au NPs as source of fluorescence and as enhancement factor, respectively, on influenza H1N1 virus surfaces (Fig. 16A). The authors observed a linear increase of photoluminescence intensity as a function of virus particle concentration (Fig. 16B), which enabled LODs of 0.03 pg/mL in water and 0.4 pg/mL in human serum. In two other reports from E. Y. Park's group, the reduction in FL intensity due to virus binding-induced steric hindrances was utilized for detection purposes. CdSeTeS[251] or CdZnSeS/ZnSeS[246] QDs were conjugated to Au NPs through an intermediate peptide linker, which also contained aspartic acid moieties with carboxyl groups. The latter allowed the conjugation of monoclonal antibodies against anti-influenza virus A/H1N1 hemagglutinin protein (Fig. 16C). Binding of virus particles to the antibodies increased the steric hindrance and the average length of the peptide linker, which reduced the plasmonic enhancement of the FL intensity from the QDs. This decrease was calibrated to determine the virus concentration (Fig. 16D), resulting in a LOD of 17.02 fg/mL for H1N1 virus and 12.1 fg/mL for norovirus-like particles.

In addition to plasmonic enhancement of fluorescence, the quenching of luminescence intensity by metal NPs at short separations has also been used to monitor pathogen concentrations. Chen and coworkers synthesized Au NP-QD nanoclusters, in which the QD photoluminescence signal was efficiently quenched by the small Au NPs (diameter < 10 nm). Binding of HBV in this study triggered the disassembly of the nanocomplex, resulting in a strong increase in the luminescence signals of the QDs.[252]

As some fluorescent molecules are also effective PSs, simultaneous FL sensing and plasmon enhanced PDCT inactivation can be applied as targeted therapeutics, as well as for the theranostic treatment of microbial infections. Wang *et al.* utilized Ag NPs functionalized with conjugated polyelectrolytes (CPs) composed of a backbone and hydrophilic side chains to capture *E. coli*.[249] The LSP of the Ag NPs achieved an efficient increase in both FL intensity and ROS generation of CPs. CPs sustain a radiative decay and fluorescence emission at 427 nm, which can be enhanced by the Ag LSP upon binding with target bacteria on the Ag NPs substrate. CPs can also sustain fluorescence resonant energy transfer (FRET) between different CP ligand units, which is detected as an emission at 663 nm. As the FRET emission is decreased upon pathogen binding due to less CPs aggregation, the ratio between FL emission intensity at 427 nm and at 663 nm can be used as metric for bacteria binding. The authors successfully tested the detection capabilities of the sensor with *E. coli* in the range of 10^5 – 10^8 CFUs. Moreover, generation of ROS and PDCT-induced bacteria inactivation with LRV = 2 after only 5 min of low power (20 mW/cm^2) white light irradiation were also reported in this work. Importantly, the FL sensing of ROS formation can also provide an effective approach to monitor and track the plasmonic PDCT inactivation efficacy (see section 4.1.1).[97,98,129] In particular, the works of Heyne and colleagues with Ag NP or nanocube-enhanced Rose Bengal demonstrated both strong distant-dependent plasmonic enhancement of $^1O_2$ luminescence and efficient killing of *S. aureus* and *E. coli*, which paves the way to an efficient theranostic strategy against bacterial infections.[97,98]

5.3 Microbial Pathogen Detection Based on LSPR and Colorimetric Sensing

Due to the refractive index dependence of the LSPR (see Equations (3), (4)), plasmonic NPs functionalized with specific microbial recognition elements facilitate LSPR sensing of pathogens. The binding of pathogen cells, viral particles, or molecules associated with the microbes increase the local refractive index around the NPs[253] and, consequently, induce a red-shift of the LSPR peak.[254–256] Therefore, the spectral shift is an important transducer for sensing purposes. For instance, the longitudinal plasmon mode of antibody-functionalized Au NRs, whose LSPR was centered at 700 nm, showed a red shift of 6 – 20 nm after addition of HBV as antigen, corresponding to an effective detection range of 0.01 – 1 IU/mL (Fig. 17A).[254] LSPR spectral shifts and associated colorimetric changes can also occur when the plasmonic NPs aggregate due to interactions with microbes or microbial metabolites. Nath *et al.* utilized dextran-coated Au NPs for bacteria (*E. coli*) detection in the presence of concanavalin A (Con A) and carbohydrates.[257] In the presence of low concentrations of bacteria, large NP clusters were formed from dextran-coated Au NPs due to Con A-mediated cross-linking of bacteria, dextran-coated Au NPs and carbohydrates, resulting in a detectable (> 4 nm) spectral shift of the Au LSPR. In the presence of a larger concentrations of bacteria, the carbohydrates were consumed by the bacteria, resulting in the formation of smaller clusters and a smaller (2–4 nm) shift of the LSPR peak. The work performed so far illustrates the versatility of the LSPR as observable to monitor even low concentrations of pathogens, which is highly beneficial for assessing the efficacy of antibacterial strategies.

In addition to inducing a spectral shift of the LSPR peak position, analyte binding to NPs can also increase both absorption and scattering intensities, which can be calibrated and used for sensing and quantification purposes.[255,258–260] Yoo *et al.* and Lee *et al.* used DNA aptamer-conjugated Au-coated silica NPs and hollow Au spike-like NPs for bacteria and avian influenza H5N1 virus detection.[255,259] In both cases, the binding of target pathogens led to a measurable increase in extinction, which was calibrated to quantify bacteria with LODs between 10 and 3×10^4 CFU/ml, or H5N1 virus hemagglutinin protein with concentrations > 1 pM.

Some fungal and bacterial species have shown to assist the growth of various shapes of plasmonic metal nanostructures from metal ions, which provides an alternative strategy to detect and identify microbial pathogens through shape and optical properties of the generated nanoparticles. The pathogen-induced formation of NPs with different shapes was attributed to the reductive effect of enzymes such as reductases and the presence of various macromolecular compounds or ligands for NP capping.[261] Tian and colleagues applied this approach for the colorimetric sensing of fungal species using a colloidal Au diagnostic reagent.[262] In the presence of the fungal target, the shape of the Au NPs quickly changed from spheres into nanostars within 2 minutes through an unknown mechanism, leading to huge changes in the absorbance spectra and manifesting a color change of the colloid from red to blue (Fig. 17B). An LOD of 10 CFU/mL was achieved for the fungus *Aspergillus niger*. Interestingly, the structural and colorimetric changes observed in this work were specific to a few tested spore-forming fungi. Changes in the environmental conditions such as salt concentration, or the presence of other types of microbes obstructed the unique shape and colorimetric responses of the NP sensors.

5.4 Electrochemical Pathogen Sensing with Plasmonic Nanostructures

The electrical conductivity and electrocatalytic performance of plasmonic NPs also enables an effective electrochemical (EC) probing of microbial pathogens. EC pathogen sensing is typically accomplished through monitoring of the impedance before and after binding of pathogen or pathogen components,[258,263–265] and/or measurement of the current at defined potentials produced by chemical redox reactions associated with the binding process.[266–270] Changes in impedance can be monitored by Nyquist plots measured from Electrical Impedance Spectroscopy (EIS). The surfaces of microbial pathogens have low conductivities and generate an increase in the charge transfer resistance (R_{ct}) at the electrode-electrolyte interface. The increase in resistance can be correlated with pathogen concentrations for quantification purposes. Wang and colleagues observed a linear relationship between R_{ct} of a doxorubicin-conjugated Au NP-modified electrode and the CFUs of *E. coli* on a decadic logarithmic scale: $R_{ct}=24.45 \times \log_{10}$ CFU - 142.82 (R=0.998) (Fig. 17C).[265] This calibration enabled a detection limit of 150 CFU/mL with a signal-to-noise ratio threshold of 3. Similar linear relationships between the R_{ct} from EIS measurements and the $\log_{10}$ concentration have been reported for the Zika virus envelope protein[263] and single-stranded DNA[264] of HBV on Au NPs-modified electrodes. The LODs were given as 10 pM and 1 aM, respectively.

The selective binding of microbial pathogens, antigens or nucleic acids to plasmonic nanostructures can initiate various catalytic or enzymatic reactions. These reactive processes can in turn result in amperometric responses, which can serve as another type of electrochemical signal for pathogens. This approach typically involves the combination of plasmonic NPs with catalysts and reactants into reactive platforms. For instance, single-stranded DNA strands conjugated to magnetic Fe_2O_3@Au core-shell NPs conjugated were used as capture probes to bind specific target *E. coli* DNA. The *E. coli* DNA subsequently bound to another reporter probe strand that immobilized horseradish peroxidase (HRP) on the NPs (Fig. 17D).[267] The magnetic NPs were collected onto the electrode through application of an external magnetic field, and the HRP was then used to catalyze the reduction of hydrogen peroxide contained in the electrolyte, which resulted in a detectable current. Stable electrochemical signals were obtained within a matter of seconds (Fig. 17D, bottom left). An LOD of 0.01 pM of DNA target and 500 CFU/mL bacteria was demonstrated within an incubation time of 2 hours. The LOD was further improved to 5 CFU/mL by increasing the incubation time to 4 h. This reaction was also utilized in another study where antibody-conjugated rGO-Au@Pt nanocomposites were adopted to bind *E. coli* antigens and to act as catalyst for the reduction of H_2O_2. The sensor achieved a LOD of 450 CFU/mL.[266] Other examples of catalyzed reactions exploited as source for electrochemical current include the electrochemical oxidation of disulfide bonds[268] and the enzyme-catalyzed reduction of p-aminophenyl phosphate to p-aminophenol.[269] These reactions were applied for the detection of Human Immunodeficiency Virus-1 (HIV-1) and avian leukosis virus subgroup J (ALV-J), respectively. For the latter case, the current signal was further enhanced through p-aminophenol-mediated Ag(0) deposition from Ag^+.

5.5 Plasmon-Enhanced Photoacoustic (PA) Imaging

The photophysical properties of plasmonic nanostructures also provide a promising strategy to enhance the contrast in photoacoustic (PA) imaging. PA imaging relies on the emission of untrasound from plasmonic NPs or other photoacoustic contrast agents, and has been applied in imaging mammal tissues and cancers *in vivo*.[271,272] In the context of plasmonic nano-antimicrobials, PA imaging has been utilized mostly to monitor bacterial inactivation. A Ag-capped Au NR system was designed to monitor Ag^+ release in antimicrobial applications.[273]

The Ag deposited on the Au core prevents an efficient NIR excitation and PA emission from the Au NRs when the structure is intact, but the dissolution of Ag upon addition of a Ag etchant initiates both the PA emission from Au NRs as well as an antimicrobial effect of Ag^+ against MRSA. Au@Ag nanoplates have been used in theranostic applications to disinfect *E. coli*-induced wounds in mice and to simultaneously monitor the wound healing through PA imaging.[185] The PA signals from the wounded mice treated with Au@Ag nanoplates revealed a quicker wound healing than for Au nanoplate controls. This difference was attributed to the photothermal and light-independent antimicrobial effect of the Au@Ag nanoplates. In another study, Lu *et al.* exploited Au NPs functionalized with P1 peptides for the treatment and PA imaging of *S. aureus*-induced wounds in mice.[274] The P1 peptide facilitated the targeting of *S. aureus* cell walls with NPs. Hydrogen bonding between P1 peptide ligands also induced clustering of Au NPs for higher PA contrast. In general, direct PA sensing of microbes is limited by the low intensities of PA emission from discrete NPs. But NP clustering[185,274] or increased absorption by both the plasmonic NPs and the surrounding medium[271,275] could provide potential experimental strategies to enhance the contrast.

5.6 Summary of Plasmonic Nano-Antimicrobial-Based Microbe Sensing Strategies

Table 4 provides an overall summary of the LSP-enabled microbial pathogen sensing techniques covered in section 5. LODs up to 10 CFU/mL or PFU/mL for microbes and/or attomolar-scale concentrations for molecular microbial biomarkers have been accomplished for various sensing modalities, including SERS, FL, LSPR and EC; while the PA strategy have primarily been used for qualitative imaging and diagnostic applications. SERS, FL, LSPR and PA have all demonstrated great promises for large-scale *in vitro* as well as potential *in vivo* sensing. In particular, SERS and TERS sensing of the intrinsic Raman features of microbes or microbial components can allow for label-free sensing of the pathogens with high sensitivity. Simultaneous microbe monitoring through SERS and FL, and inactivation through PDCT, PC or additional have been achieved, facilitating a theranostic application of the plasmonic nano-antimicrobials in treatment of microbe-induced diseases.

6. Summary and Outlook

In this manuscript, we have reviewed the photophysical properties of plasmonic nano-antimicrobials and their relevance to the detection, quantification and inactivation of microbial pathogens. The studies performed so far show that plasmonic NPs are instrumental in microbial inactivation through different pathways. Plasmonic NPs can themselves sustain both light-dependent and -independent inactivation mechanisms, or provide delivery and controlled release pathways for molecular microbicides. Furthermore, as plasmonic nanostructures, in general, can also enable enhanced microbe detection and identification, they provide unique opportunities to minimize exposure to microbial pathogens. Plasmonic nano-antimicrobials that combine microbicidal and diagnostic functionalities have also led to theranostic applications, in which simultaneous detection, monitoring and inactivation of microbes are achieved.

Table 5 compares the properties of plasmonic nano-antimicrobials with other antimicrobial strategies, including conventional sterilization techniques such as UV treatment or autoclaving, other nanoscale antimicrobials such as semiconductors and MOFs, molecular antimicrobial drugs or antimicrobial peptides, and macroscale antimicrobial materials such as antimicrobial coatings. Plasmonic nano-antimicrobials have proven effective against a broad range of microbial pathogens. A microbicidal effect with LRVs > 3 was achieved for Gram-positive, -negative and mollicute bacteria, enveloped and non-enveloped viruses, and fungi within minutes to a few hours of treatment. Some plasmon-enabled inactivation strategies, such as the plasmon-enhanced photonic shockwave inactivation, have shown promise for the selective inactivation of microbes even in the presence of mammalian cells and are, therefore, of significant interest for future *in vivo* sterilization approaches. Moreover, in some cases of PDCT, PC, PPT and NP-enabled controlled release, ambient white-light illumination was shown to be sufficient to achieve efficient inactivation. These observations underline the potential of plasmonic nano-antimicrobials to enable efficient sterilization approaches with low energy consumption. As plasmonic nano-antimicrobials enable different chemical and photophysical inactivation pathways, it is feasible to implement strategies that utilize multiple mechanisms to achieve efficient synergistic inactivation. Plasmonic nano-antimicrobials could also play an important role in mitigating and controlling future pandemic diseases caused by microbes, for which effective antimicrobial compounds are lacking. Plasmonic nano-antimicrobials also face some important challenges. Utilization of light-dependent plasmonic anti-microbial inactivation mechanisms requires efficient illumination of the NPs, which can be challenging in some *in vivo* applications if the sites of infections are not readily accessible. However, light-independent inactivation and microbicide release mechanisms can be applied in a minimally invasive manner without any external illumination, such as initiation of release processes by chemical signals secreted by the microbes.[15,213] For those application that require light, NIR-responsive materials such as nanorods or bipyramids[42,86] can be helpful due to the larger tissue penetration depths at these wavelengths. Up-conversion strategies through resonant energy transfers between NIR-responsive light donors and UV- or visible-responsive materials have also been shown to allow for photoexcitation with higher wavelengths.[141] In addition, the use of optical fibers for efficient light delivery is widely available and represent a minimally invasive procedure that can provide illumination in deep tissues.

Another challenge for plasmonic nano-antimicrobials, in particular in the case of PC or PDCT inactivation pathways, is the generation of undesired collateral cytotoxicity by plasmonic NPs, photosensitizers and/or photocatalysts. One strategy to minimize the collateral damage is to further increase the plasmonic enhancement as well as the efficacy of the inactivation mechanisms so that the required dosage of microbicidal components can be further reduced. In addition, localizing the antimicrobial effect by selective pathogen targeting, or passivating the plasmonic nanostructures by encapsulation in liposomes or polymersome could also contribute to limiting the collateral damage of plasmonic nano-antimicrobials.[118,212,276]

Finally, the development of resistance against metal cation-based inactivation strategies is a concern for some types of plasmonic nano-antimicrobials. Several studies have reported altered gene expression levels or other cellular changes indicative of emerging resistances against metal cations.[210,211] These resistances can, however, be overcome by “multimodal” inactivation strategies that combine M^{n+}-associated light-independent mechanisms with light-dependent mechanisms or rational microbicide delivery functionalities of the NPs. Such strategies provide a more resilient microbicidal effect as they can affect multiple structural or metabolomic aspects of the pathogens simultaneously.

To harness the full potential of plasmonic nano-antimicrobials, future work should focus on further improving the efficacy of a broad range of diverse microbial pathogens in biological medium, reducing the time required for complete inactivation, and limiting the collateral damage by active targeting of the microbial pathogens or enhancing the selectivity of the antimicrobial effects.

Supplementary Material

Refer to Web version on PubMed Central for supplementary material.

Acknowledgements

The authors thank Dr. Mina Nazari for recording of the bubble formation image and movies. B.M.R. acknowledges support from the National Institutes of Health through grants R01AI132111 and R01CA138509.

Notes and References

(1). Petrova VN; Russell CA The evolution of seasonal influenza viruses. Nature Reviews Microbiology 2018, 16, 47. [PubMed: 29081496]

(2). Lee Y; Puumala E; Robbins N; Cowen LE Antifungal Drug Resistance: Molecular Mechanisms in Candida albicans and Beyond. Chemical Reviews 2020.

(3). Todar K: Todar’s online textbook of bacteriology. University of Wisconsin Madison^ eWisconsin Wisconsin, 2004.

(4). Neu HC The crisis in antibiotic resistance. Science 1992, 257, 1064–1073. [PubMed: 1509257]

(5). Gupta A; Mumtaz S; Li C-H; Hussain I; Rotello VM Combatting antibiotic-resistant bacteria using nanomaterials. Chemical Society Reviews 2019, 48, 415–427. [PubMed: 30462112]

(6). Berman J; Krysan DJ Drug resistance and tolerance in fungi. Nature Reviews Microbiology 2020, 1–13. [PubMed: 31740776]

(7). Jiang Q; Jie Y; Han Y; Gao C; Zhu H; Willander M; Zhang X; Cao X Self-powered electrochemical water treatment system for sterilization and algae removal using water wave energy. Nano Energy 2015, 18, 81–88.

(8). Bekmukhametova A; Ruprai H; Hook JM; Mawad D; Houang J; Lauto A Photodynamic therapy with nanoparticles to combat microbial infection and resistance. Nanoscale 2020.

(9). Xie S; Manuguri S; Proietti G; Romson J; Fu Y; Inge AK; Wu B; Zhang Y; Häll D; Ramström O Design and synthesis of theranostic antibiotic nanodrugs that display enhanced antibacterial activity and luminescence. Proceedings of the National Academy of Sciences 2017, 114, 8464–8469.

(10). Zhou J; Jayawardana KW; Kong N; Ren Y; Hao N; Yan M; Ramström O Trehalose-Conjugated, Photofunctionalized Mesoporous Silica Nanoparticles for Efficient Delivery of Isoniazid into Mycobacteria. ACS Biomaterials Science & Engineering 2015, 1, 1250–1255. [PubMed: 33429672]

(11). Ji H; Dong K; Yan Z; Ding C; Chen Z; Ren J; Qu X Bacterial Hyaluronidase Self - Triggered Prodrug Release for Chemo-Photothermal Synergistic Treatment of Bacterial Infection. Small 2016, 12, 6200–6206. [PubMed: 27690183]

(12). Roy I; Shetty D; Hota R; Baek K; Kim J; Kim C; Kappert S; Kim K A multifunctional subphthalocyanine nanosphere for targeting, labeling, and killing of antibiotic-resistant bacteria. Angewandte Chemie International Edition 2015, 54, 15152–15155. [PubMed: 26493283]

(13). Li X; Lee D; Huang JD; Yoon J Phthalocyanine - Assembled Nanodots as Photosensitizers for Highly Efficient Type I Photoreactions in Photodynamic Therapy. Angewandte Chemie 2018, 130, 10033–10038.

(14). Li P; Li J; Feng X; Li J; Hao Y; Zhang J; Wang H; Yin A; Zhou J; Ma X Metal-organic frameworks with photocatalytic bactericidal activity for integrated air cleaning. Nature communications 2019, 10, 1–10.

(15). Zhang Y; Sun P; Zhang L; Wang Z; Wang F; Dong K; Liu Z; Ren J; Qu X Silver - Infused Porphyrinic Metal – Organic Framework: Surface - Adaptive, On - Demand Nanoplatform for Synergistic Bacteria Killing and Wound Disinfection. Advanced Functional Materials 2019, 29, 1808594.

(16). Zhu Y; Xu C; Zhang N; Ding X; Yu B; Xu FJ Polycationic synergistic antibacterial agents with multiple functional components for efficient anti - infective therapy. Advanced Functional Materials 2018, 28, 1706709.

(17). Hynek J; Zelenka J; Rathouský J. i.; Kubát P; Ruml T. s.; Demel J; Lang K Designing porphyrinic covalent organic frameworks for the photodynamic inactivation of bacteria. ACS applied materials & interfaces 2018, 10, 8527–8535. [PubMed: 29470048]

(18). Wang W; Yu JC; Xia D; Wong PK; Li Y Graphene and g-C3N4 nanosheets cowrapped elemental α-sulfur as a novel metal-free heterojunction photocatalyst for bacterial inactivation under visible-light. Environmental science & technology 2013, 47, 8724–8732. [PubMed: 23859533]

(19). Liu Y; Lin A; Liu J; Chen X; Zhu X; Gong Y; Yuan G; Chen L; Liu J Enzyme-Responsive Mesoporous Ruthenium for Combined Chemo-Photothermal Therapy of Drug-Resistant Bacteria. ACS applied materials & interfaces 2019, 11, 26590–26606. [PubMed: 31264823]

(20). Wang W; Ng TW; Ho WK; Huang J; Liang S; An T; Li G; Jimmy CY; Wong PK CdIn2S4 microsphere as an efficient visible-light-driven photocatalyst for bacterial inactivation: Synthesis, characterizations and photocatalytic inactivation mechanisms. Applied Catalysis B: Environmental 2013, 129, 482–490.

(21). Foster HA; Ditta IB; Varghese S; Steele A Photocatalytic disinfection using titanium dioxide: spectrum and mechanism of antimicrobial activity. Applied microbiology and biotechnology 2011, 90, 1847–1868. [PubMed: 21523480]

(22). Adams LK; Lyon DY; Alvarez PJ Comparative ecotoxicity of nanoscale TiO2, SiO2, and ZnO water suspensions. Water research 2006, 40, 3527–3532. [PubMed: 17011015]

(23). Sirelkhatim A; Mahmud S; Seeni A; Kaus NHM; Ann LC; Bakhori SKM; Hasan H; Mohamad D Review on zinc oxide nanoparticles: antibacterial activity and toxicity mechanism. Nano-Micro Letters 2015, 7, 219–242. [PubMed: 30464967]

(24). Lipovsky A; Nitzan Y; Gedanken A; Lubart R Antifungal activity of ZnO nanoparticles—the role of ROS mediated cell injury. Nanotechnology 2011, 22, 105101. [PubMed: 21289395]

(25). Booshehri AY; Goh SC-K; Hong J; Jiang R; Xu R Effect of depositing silver nanoparticles on BiVO 4 in enhancing visible light photocatalytic inactivation of bacteria in water. Journal of Materials Chemistry A 2014, 2, 6209–6217.

(26). Wang W; Yu Y; An T; Li G; Yip HY; Yu JC; Wong PK Visible-light-driven photocatalytic inactivation of E. coli K-12 by bismuth vanadate nanotubes: bactericidal performance and mechanism. Environmental science & technology 2012, 46, 4599–4606. [PubMed: 22428729]

(27). Boruah B; Gupta R; Modak JM; Madras G Novel insights into the properties of AgBiO3 photocatalyst and its application in immobilized state for 4-nitrophenol degradation and bacteria inactivation. Journal of Photochemistry and Photobiology A: Chemistry 2019, 373, 105–115.

(28). Wang R; Kong X; Zhang W; Zhu W; Huang L; Wang J; Zhang X; Liu X; Hu N; Suo Y Mechanism insight into rapid photocatalytic disinfection of Salmonella based on vanadate QDs-interspersed g-C3N4 heterostructures. Applied Catalysis B: Environmental 2018, 225, 228–237.

(29). Wang W; Li G; Xia D; An T; Zhao H; Wong PK Photocatalytic nanomaterials for solar-driven bacterial inactivation: recent progress and challenges. Environmental Science: Nano 2017, 4, 782–799.

(30). Peng Z; Wu D; Wang W; Tan F; Wang X; Chen J; Qiao X Effect of metal ion doping on ZnO nanopowders for bacterial inactivation under visible-light irradiation. Powder Technology 2017, 315, 73–80.

(31). Karunakaran C; Abiramasundari G; Gomathisankar P; Manikandan G; Anandi V Cu-doped TiO2 nanoparticles for photocatalytic disinfection of bacteria under visible light. Journal of colloid and interface science 2010, 352, 68–74. [PubMed: 20832079]

(32). Sadowski R; Strus M; Buchalska M; Heczko PB; Macyk W Visible light induced photocatalytic inactivation of bacteria by modified titanium dioxide films on organic polymers. Photochemical & Photobiological Sciences 2015, 14, 514–519. [PubMed: 25254352]

(33). Salabat A; Mirhoseini F Applications of a new type of poly (methyl methacrylate)/TiO 2 nanocomposite as an antibacterial agent and a reducing photocatalyst. Photochemical & Photobiological Sciences 2015, 14, 1637–1643. [PubMed: 26112068]

(34). Jain PK; Lee KS; El-Sayed IH; El-Sayed MA Calculated absorption and scattering properties of gold nanoparticles of different size, shape, and composition: applications in biological imaging and biomedicine. The journal of physical chemistry B 2006, 110, 7238–7248. [PubMed: 16599493]

(35). Hong Y; Reinhard BM Optoplasmonics: basic principles and applications. Journal of Optics 2019, 21, 113001.

(36). Yan B; Boriskina SV; Reinhard BM Optimizing gold nanoparticle cluster configurations (n≤ 7) for array applications. The Journal of Physical Chemistry C 2011, 115, 4578–4583.

(37). Zhang Y; He S; Guo W; Hu Y; Huang J; Mulcahy JR; Wei WD Surface-plasmon-driven hot electron photochemistry. Chemical reviews 2017, 118, 2927–2954. [PubMed: 29190069]

(38). Kale MJ; Avanesian T; Christopher P Direct photocatalysis by plasmonic nanostructures. Acs Catalysis 2014, 4, 116–128.

(39). Baffou G; Quidant R Thermo - plasmonics: using metallic nanostructures as nano-sources of heat. Laser & Photonics Reviews 2013, 7, 171–187.

(40). Boulais E. t.; Lachaine R. m.; Meunier M Plasma-mediated nanocavitation and photothermal effects in ultrafast laser irradiation of gold nanorods in water. The Journal of Physical Chemistry C 2013, 117, 9386–9396.

(41). Neumann O; Urban AS; Day J; Lal S; Nordlander P; Halas NJ Solar vapor generation enabled by nanoparticles. ACS nano 2013, 7, 42–49. [PubMed: 23157159]

(42). Nazari M; Xi M; Lerch S; Alizadeh M; Ettinger C; Akiyama H; Gillespie C; Gummuluru S; Erramilli S; Reinhard BM Plasmonic Enhancement of Selective Photonic Virus Inactivation. Scientific reports 2017, 7, 1–10. [PubMed: 28127051]

(43). Guo K; Verschuuren MA; Koenderink AF Superresolution imaging of the local density of states in plasmon lattices. Optica 2016, 3, 289–298.

(44). Carminati R; Cazé A; Cao D; Peragut F; Krachmalnicoff V; Pierrat R; De Wilde Y Electromagnetic density of states in complex plasmonic systems. Surface Science Reports 2015, 70, 1–41.

(45). Bauch M; Toma K; Toma M; Zhang Q; Dostalek J Plasmon-enhanced fluorescence biosensors: a review. Plasmonics 2014, 9, 781–799. [PubMed: 27330521]

(46). Muskens O; Giannini V; Sánchez-Gil JA; Gómez Rivas J Strong enhancement of the radiative decay rate of emitters by single plasmonic nanoantennas. Nano letters 2007, 7, 2871–2875. [PubMed: 17683156]

(47). Mertens H; Koenderink A; Polman A Plasmon-enhanced luminescence near noble-metal nanospheres: Comparison of exact theory and an improved Gersten and Nitzan model. Physical Review B 2007, 76, 115123.

(48). Kühn S; Håkanson U; Rogobete L; Sandoghdar V Enhancement of single-molecule fluorescence using a gold nanoparticle as an optical nanoantenna. Physical review letters 2006, 97, 017402. [PubMed: 16907406]

(49). Banholzer MJ; Millstone JE; Qin L; Mirkin CA Rationally designed nanostructures for surface-enhanced Raman spectroscopy. Chemical Society Reviews 2008, 37, 885–897. [PubMed: 18443674]

(50). Yang L; Yan B; Premasiri WR; Ziegler LD; Negro LD; Reinhard BM Engineering nanoparticle cluster arrays for bacterial biosensing: the role of the building block in multiscale SERS substrates. Advanced Functional Materials 2010, 20, 2619–2628.

(51). Yan B; Thubagere A; Premasiri WR; Ziegler LD; Dal Negro L; Reinhard BM Engineered SERS substrates with multiscale signal enhancement: nanoparticle cluster arrays. Acs Nano 2009, 3, 1190–1202. [PubMed: 19354266]

(52). Yan B; Boriskina SV; Reinhard BM Design and implementation of noble metal nanoparticle cluster arrays for plasmon enhanced biosensing. The Journal of Physical Chemistry C 2011, 115, 24437–24453.

(53). Hall WP; Ngatia SN; Van Duyne RP LSPR biosensor signal enhancement using nanoparticle−antibody conjugates. The Journal of Physical Chemistry C 2011, 115, 1410–1414.

(54). Willets KA; Van Duyne RP Localized surface plasmon resonance spectroscopy and sensing. Annu. Rev. Phys. Chem. 2007, 58, 267–297. [PubMed: 17067281]

(55). Rong G; Wang H; Skewis LR; Reinhard BM Resolving sub-diffraction limit encounters in nanoparticle tracking using live cell plasmon coupling microscopy. Nano Letters 2008, 8, 3386–3393. [PubMed: 18788826]

(56). Rong G; Wang H; Reinhard BM Insights from a nanoparticle minuet: two-dimensional membrane profiling through silver plasmon ruler tracking. Nano letters 2010, 10, 230–238. [PubMed: 20017502]

(57). Wang H; Reinhard BM Monitoring simultaneous distance and orientation changes in discrete dimers of DNA linked gold nanoparticles. The Journal of Physical Chemistry C 2009, 113, 11215–11222.

(58). Wu L; Reinhard BM Probing subdiffraction limit separations with plasmon coupling microscopy: concepts and applications. Chemical Society Reviews 2014, 43, 3884–3897. [PubMed: 24390574]

(59). Chen T; Hong Y; Reinhard BM Probing DNA stiffness through optical fluctuation analysis of plasmon rulers. Nano letters 2015, 15, 5349–5357. [PubMed: 26121062]

(60). Zhang S; Reinhard BM Characterizing large-scale receptor clustering on the single cell level: a comparative plasmon coupling and fluorescence superresolution microscopy study. The Journal of Physical Chemistry B 2019, 123, 5494–5505. [PubMed: 31244098]

(61). Wang H; Rong G; Yan B; Yang L; Reinhard BM Optical sizing of immunolabel clusters through multispectral plasmon coupling microscopy. Nano letters 2011, 11, 498–504. [PubMed: 21247191]

(62). Shai Y Mode of action of membrane active antimicrobial peptides. Peptide Science: Original Research on Biomolecules 2002, 66, 236–248.

(63). Trachtenberg S Mollicutes—wall-less bacteria with internal cytoskeletons. Journal of structural biology 1998, 124, 244–256. [PubMed: 10049810]

(64). Margesin R; Schinner F Heavy metal resistant Arthrobacter sp.—A tool for studying conjugational plasmid transfer between Gram-negative and Gram-positive bacteria. Journal of basic microbiology 1997, 37, 217–227. [PubMed: 9265744]

(65). Malleck T; Daufouy G; André S; Broussolle V; Planchon S Temperature impacts the sporulation capacities and spore resistance of Moorella thermoacetica. Food microbiology 2018, 73, 334–341. [PubMed: 29526221]

(66). Lopes RP; Mota MJ; Gomes AM; Delgadillo I; Saraiva JA Application of high pressure with homogenization, temperature, carbon dioxide, and cold plasma for the inactivation of bacterial spores: a review. Comprehensive Reviews in Food Science and Food Safety 2018, 17, 532–555. [PubMed: 33350128]

(67). de Miguel I; Prieto I; Albornoz A; Sanz V; Weis C; Turon P; Quidant R Plasmon-Based Biofilm Inhibition on Surgical Implants. Nano letters 2019, 19, 2524–2529. [PubMed: 30860848]

(68). Mah T-FC; O'Toole GA Mechanisms of biofilm resistance to antimicrobial agents. Trends in microbiology 2001, 9, 34–39. [PubMed: 11166241]

(69). Harris SD Branching of fungal hyphae: regulation, mechanisms and comparison with other branching systems. Mycologia 2008, 100, 823–832. [PubMed: 19202837]

(70). Gonzales FP; Maisch T Photodynamic inactivation for controlling Candida albicans infections. Fungal biology 2012, 116, 1–10. [PubMed: 22208597]

(71). Anderson JB Evolution of antifungal-drug resistance: mechanisms and pathogen fitness. Nature Reviews Microbiology 2005, 3, 547–556. [PubMed: 15953931]

(72). Wigginton KR; Kohn T Virus disinfection mechanisms: the role of virus composition, structure, and function. Current opinion in virology 2012, 2, 84–89. [PubMed: 22440970]

(73). Johnson VA; Calvez V; Günthard HF; Paredes R; Pillay D; Shafer R; Wensing AM; Richman DD 2011 update of the drug resistance mutations in HIV-1. Topics in antiviral medicine 2011, 19, 156. [PubMed: 22156218]

(74). Mascio CT; Alder JD; Silverman JA Bactericidal action of daptomycin against stationary-phase and nondividing Staphylococcus aureus cells. Antimicrobial agents and chemotherapy 2007, 51, 4255–4260. [PubMed: 17923487]

(75). Berney M; Hammes F; Bosshard F; Weilenmann H-U; Egli T Assessment and interpretation of bacterial viability by using the LIVE/DEAD BacLight Kit in combination with flow cytometry. Applied and environmental microbiology 2007, 73, 3283–3290. [PubMed: 17384309]

(76). Vanhauteghem D; Demeyere K; Callaert N; Boelaert A; Haesaert G; Audenaert K; Meyer E Flow cytometry is a powerful tool for assessment of the viability of fungal conidia in metalworking fluids. Applied and environmental microbiology 2017, 83.

(77). Maier SA: Plasmonics: fundamentals and applications; Springer Science & Business Media, 2007.

(78). Jain PK; El-Sayed MA Plasmonic coupling in noble metal nanostructures. Chemical Physics Letters 2010, 487, 153–164.

(79). Halas N Playing with plasmons: tuning the optical resonant properties of metallic nanoshells. Mrs Bulletin 2005, 30, 362–367.

(80). Sun Y; Xia Y Shape-controlled synthesis of gold and silver nanoparticles. science 2002, 298, 2176–2179. [PubMed: 12481134]

(81). Eustis S; El-Sayed MA Why gold nanoparticles are more precious than pretty gold: noble metal surface plasmon resonance and its enhancement of the radiative and nonradiative properties of nanocrystals of different shapes. Chemical society reviews 2006, 35, 209–217. [PubMed: 16505915]

(82). Link S; El-Sayed MA: Spectral properties and relaxation dynamics of surface plasmon electronic oscillations in gold and silver nanodots and nanorods. ACS Publications, 1999.

(83). Murphy CJ; Sau TK; Gole A; Orendorff CJ Surfactant-directed synthesis and optical properties of one-dimensional plasmonic metallic nanostructures. Mrs Bulletin 2005, 30, 349–355.

(84). Jijie R; Dumych T; Chengnan L; Bouckaert J; Turcheniuk K; Hage C-H; Heliot L; Cudennec B; Dumitrascu N; Boukherroub R Particle-based photodynamic therapy based on indocyanine green modified plasmonic nanostructures for inactivation of a Crohn’s disease-associated Escherichia coli strain. Journal of Materials Chemistry B 2016, 4, 2598–2605. [PubMed: 32263283]

(85). Xi M; Reinhard BM Evolution of near-and far-field optical properties of Au bipyramids upon epitaxial deposition of Ag. Nanoscale 2020, 12, 5402–5411. [PubMed: 32077890]

(86). Nazari M; Xi M; Aronson M; Mcrae O; Hong MK; Gummuluru S; Sgro AE; Bird JC; Ziegler LD; Gillespie C Plasmon-Enhanced Pan-Microbial Pathogen Inactivation in the Cavitation Regime: Selectivity Without Targeting. ACS Applied Nano Materials 2019, 2, 2548–2558.

(87). Mo S; Chen X; Chen M; He C; Lu Y; Zheng N Two-dimensional antibacterial Pd@ Ag nanosheets with a synergetic effect of plasmonic heating and Ag+ release. Journal of Materials Chemistry B 2015, 3, 6255–6260. [PubMed: 32262744]

(88). Poletti A; Fracasso G; Conti G; Pilot R; Amendola V Laser generated gold nanocorals with broadband plasmon absorption for photothermal applications. Nanoscale 2015, 7, 13702–13714. [PubMed: 26219425]

(89). Turcheniuk K; Turcheniuk V; Hage C-H; Dumych T; Bilyy R; Bouckaert J; Héliot L; Zaitsev V; Boukherroub R; Szunerits S Highly effective photodynamic inactivation of E. coli using gold nanorods/SiO 2 core–shell nanostructures with embedded verteporfin. Chemical Communications 2015, 51, 16365–16368. [PubMed: 26403761]

(90). Zheng X; Shen Z.-p.; Cheng C; Shi L; Cheng R; Dong J Electrospinning Cu–TiO 2 nanofibers used for photocatalytic disinfection of bacteriophage f2: preparation, optimization and characterization. RSC advances 2017, 7, 52172–52179.

(91). Zheng X; Shen Z.-p.; Cheng C; Shi L; Cheng R; Yuan D.-h. Photocatalytic disinfection performance in virus and virus/bacteria system by Cu-TiO2 nanofibers under visible light. Environmental Pollution 2018, 237, 452–459. [PubMed: 29510364]

(92). Boriskina SV; Reinhard BM Molding the flow of light on the nanoscale: from vortex nanogears to phase-operated plasmonic machinery. Nanoscale 2012, 4, 76–90. [PubMed: 22127488]

(93). An X; Stelter D; Keyes T; Reinhard BM Plasmonic Photocatalysis of Urea Oxidation and Visible-Light Fuel Cells. Chem 2019, 5, 2228–2242.

(94). Gontero D; Veglia AV; Bracamonte AG; Boudreau D Synthesis of ultraluminescent gold core–shell nanoparticles as nanoimaging platforms for biosensing applications based on metal-enhanced fluorescence. RSC advances 2017, 7, 10252–10258.

(95). Gontero DI; Veglia AV; Boudreau D; Bracamonte AG Ultraluminescent gold core–shell nanoparticles applied to individual bacterial detection based on metal-enhanced fluorescence nanoimaging. Journal of Nanophotonics 2017, 12, 012505.

(96). Anger P; Bharadwaj P; Novotny L Enhancement and quenching of single-molecule fluorescence. Physical review letters 2006, 96, 113002. [PubMed: 16605818]

(97). Planas O; Macia N; Agut M; Nonell S; Heyne B Distance-dependent plasmon-enhanced singlet oxygen production and emission for bacterial inactivation. Journal of the American Chemical Society 2016, 138, 2762–2768. [PubMed: 26867005]

(98). Macia N; Bresoli-Obach R; Nonell S; Heyne B Hybrid silver nanocubes for improved plasmon-enhanced singlet oxygen production and inactivation of bacteria. Journal of the American Chemical Society 2018, 141, 684–692. [PubMed: 30525580]

(99). Linic S; Christopher P; Ingram DB Plasmonic-metal nanostructures for efficient conversion of solar to chemical energy. Nature materials 2011, 10, 911–921. [PubMed: 22109608]

(100). Wellstood F; Urbina C; Clarke J Hot-electron effects in metals. Physical Review B 1994, 49, 5942.

(101). Kazuma E; Jung J; Ueba H; Trenary M; Kim Y Real-space and real-time observation of a plasmon-induced chemical reaction of a single molecule. Science 2018, 360, 521–526. [PubMed: 29724952]

(102). Manjavacas A; Liu JG; Kulkarni V; Nordlander P Plasmon-induced hot carriers in metallic nanoparticles. ACS nano 2014, 8, 7630–7638. [PubMed: 24960573]

(103). Besteiro LV; Kong X-T; Wang Z; Hartland G; Govorov AO Understanding hot-electron generation and plasmon relaxation in metal nanocrystals: Quantum and classical mechanisms. Acs Photonics 2017, 4, 2759–2781.

(104). Linic S; Chavez S; Elias R Flow and extraction of energy and charge carriers in hybrid plasmonic nanostructures. Nature Materials 2021, 10.1038/s41563-020-00858-4.

(105). Brown AM; Sundararaman R; Narang P; Goddard WA III; Atwater HA Nonradiative plasmon decay and hot carrier dynamics: effects of phonons, surfaces, and geometry. Acs Nano 2016, 10, 957–966. [PubMed: 26654729]

(106). Hendrich C; Bosbach J; Stietz F; Hubenthal F; Vartanyan T; Träger F Chemical interface damping of surface plasmon excitation in metal nanoparticles: a study by persistent spectral hole burning. Applied Physics B 2003, 76, 869–875.

(107). Foerster B; Joplin A; Kaefer K; Celiksoy S; Link S; Sönnichsen C Chemical interface damping depends on electrons reaching the surface. ACS nano 2017, 11, 2886–2893. [PubMed: 28301133]

(108). Persson B Polarizability of small spherical metal particles: influence of the matrix environment. Surface Science 1993, 281, 153–162.

(109). Lee SY; Tsalu PV; Kim GW; Seo MJ; Hong JW; Ha JW Tuning chemical interface damping: Interfacial electronic effects of adsorbate molecules and sharp tips of single gold bipyramids. Nano Letters 2019, 19, 2568–2574. [PubMed: 30856334]

(110). Chen X; Chen Y; Yan M; Qiu M Nanosecond photothermal effects in plasmonic nanostructures. ACS nano 2012, 6, 2550–2557. [PubMed: 22356648]

(111). Boulais E; Lachaine R; Hatef A; Meunier M Plasmonics for pulsed-laser cell nanosurgery: Fundamentals and applications. Journal of Photochemistry and Photobiology C: Photochemistry Reviews 2013, 17, 26–49.

(112). Jaque D; Maestro LM; Del Rosal B; Haro-Gonzalez P; Benayas A; Plaza J; Rodriguez EM; Sole JG Nanoparticles for photothermal therapies. nanoscale 2014, 6, 9494–9530. [PubMed: 25030381]

(113). Sinibaldi G; Occhicone A; Alves Pereira F; Caprini D; Marino L; Michelotti F; Casciola C Laser induced cavitation: Plasma generation and breakdown shockwave. Physics of Fluids 2019, 31, 103302.

(114). Noack J; Vogel A Laser-induced plasma formation in water at nanosecond to femtosecond time scales: calculation of thresholds, absorption coefficients, and energy density. IEEE journal of quantum electronics 1999, 35, 1156–1167.

(115). Dadlani AL; Schindler P; Logar M; Walch SP; Prinz FB Energy states of ligand capped Ag nanoparticles: relating surface plasmon resonance to work function. The Journal of Physical Chemistry C 2014, 118, 24827–24832.

(116). Li X; Wang Y; Zaytsev ME; Lajoinie G; Le The H; Bomer JG; Eijkel JC; Zandvliet HJ; Zhang X; Lohse D Plasmonic Bubble Nucleation and Growth in Water: Effect of Dissolved Air. The Journal of Physical Chemistry C 2019, 123, 23586–23593.

(117). Boulais E. t.; Lachaine R. m.; Meunier M Plasma mediated off-resonance plasmonic enhanced ultrafast laser-induced nanocavitation. Nano letters 2012, 12, 4763–4769. [PubMed: 22845691]

(118). An X; Naowarojna N; Liu P; Reinhard BM Hybrid Plasmonic Photoreactors as Visible Light-Mediated Bactericides. ACS Applied Materials & Interfaces 2019.

(119). Kuo W-S; Chang C-N; Chang Y-T; Yeh C-S Antimicrobial gold nanorods with dual-modality photodynamic inactivation and hyperthermia. Chemical communications 2009, 4853–4855. [PubMed: 19652803]

(120). Ding R; Yu X; Wang P; Zhang J; Zhou Y; Cao X; Tang H; Ayres N; Zhang P Hybrid photosensitizer based on amphiphilic block copolymer stabilized silver nanoparticles for highly efficient photodynamic inactivation of bacteria. RSC advances 2016, 6, 20392–20398.

(121). Khlebtsov BN; Tuchina ES; Khanadeev VA; Panfilova EV; Petrov PO; Tuchin VV; Khlebtsov NG Enhanced photoinactivation of Staphylococcus aureus with nanocomposites containing plasmonic particles and hematoporphyrin. Journal of Biophotonics 2013, 6, 338–351. [PubMed: 22736550]

(122). Mantareva V; Kussovski V; Angelov I; Wöhrle D; Dimitrov R; Popova E; Dimitrov S Non-aggregated Ga (III)-phthalocyanines in the photodynamic inactivation of planktonic and biofilm cultures of pathogenic microorganisms. Photochemical & Photobiological Sciences 2011, 10, 91–102. [PubMed: 21031201]

(123). Soares BM; da Silva DL; Sousa GR; Amorim JCF; de Resende MA; Pinotti M; Cisalpino PS In vitro photodynamic inactivation of Candida spp. growth and adhesion to buccal epithelial cells. Journal of Photochemistry and Photobiology B: Biology 2009, 94, 65–70.

(124). Wijesiri N; Yu Z; Tang H; Zhang P Antifungal photodynamic inactivation against dermatophyte Trichophyton rubrum using nanoparticle-based hybrid photosensitizers. Photodiagnosis and photodynamic therapy 2018, 23, 202–208. [PubMed: 29944934]

(125). Baptista MS; Cadet J; Di Mascio P; Ghogare AA; Greer A; Hamblin MR; Lorente C; Nunez SC; Ribeiro MS; Thomas AH Type I and type II photosensitized oxidation reactions: guidelines and mechanistic pathways. Photochemistry and photobiology 2017, 93, 912–919. [PubMed: 28084040]

(126). Hamblin MR Antimicrobial photodynamic inactivation: a bright new technique to kill resistant microbes. Current opinion in microbiology 2016, 33, 67–73. [PubMed: 27421070]

(127). Giannakis S; López MIP; Spuhler D; Pérez JAS; Ibáñez PF; Pulgarin C Solar disinfection is an augmentable, in situ-generated photo-Fenton reaction—Part 1: A review of the mechanisms and the fundamental aspects of the process. Applied Catalysis B: Environmental 2016, 199, 199–223.

(128). Rivas Aiello M.a. B. n.; Ghilini F; Martínez Porcel J. n. E.; Giovanetti L; Schilardi PL; Mártire DO Riboflavin-Mediated Photooxidation of Gold Nanoparticles and Its Effect on the Inactivation of Bacteria. Langmuir 2020, 36, 8272–8281. [PubMed: 32569473]

(129). Huang X; Chen G; Pan J; Chen X; Huang N; Wang X; Liu J Effective PDT/PTT dual-modal phototherapeutic killing of pathogenic bacteria by using ruthenium nanoparticles. Journal of Materials Chemistry B 2016, 4, 6258–6270. [PubMed: 32263638]

(130). Eruslanov E; Kusmartsev S: Identification of ROS using oxidized DCFDA and flow-cytometry. In Advanced protocols in oxidative stress II; Springer, 2010; pp 57–72.

(131). Li H; Zou Y; Jiang J Ag@ CuO nanohybrids synthesis and their photo-enhanced bactericidal effect through concerted Ag ion release and reactive oxygen species generation. Dalton Transactions 2020.

(132). Hou Y; Li X; Zhao Q; Chen G; Raston CL Role of hydroxyl radicals and mechanism of Escherichia coli inactivation on Ag/AgBr/TiO2 nanotube array electrode under visible light irradiation. Environmental science & technology 2012, 46, 4042–4050. [PubMed: 22385264]

(133). Hu P; Tirelli N Scavenging ROS: superoxide dismutase/catalase mimetics by the use of an oxidation-sensitive nanocarrier/enzyme conjugate. Bioconjugate chemistry 2012, 23, 438–449. [PubMed: 22292618]

(134). Loeb S; Li C; Kim J-H Solar photothermal disinfection using broadband-light absorbing gold nanoparticles and carbon black. Environmental science & technology 2018, 52, 205–213. [PubMed: 29240431]

(135). Bacellar IO; Baptista MS Mechanisms of Photosensitized Lipid Oxidation and Membrane Permeabilization. ACS omega 2019, 4, 21636–21646. [PubMed: 31891041]

(136). Bacellar IO; Oliveira MC; Dantas LS; Costa EB; Junqueira HC; Martins WK; Durantini A. s. M.; Cosa G; Di Mascio P; Wainwright M Photosensitized membrane permeabilization requires contact-dependent reactions between photosensitizer and lipids. Journal of the American Chemical Society 2018, 140, 9606–9615. [PubMed: 29989809]

(137). Yusupov M; Wende K; Kupsch S; Neyts E; Reuter S; Bogaerts A Effect of head group and lipid tail oxidation in the cell membrane revealed through integrated simulations and experiments. Scientific reports 2017, 7, 1–14. [PubMed: 28127051]

(138). Tai W-Y; Yang Y-C; Lin H-J; Huang C-P; Cheng Y-L; Chen M-F; Yen H-L; Liau I Interplay between structure and fluidity of model lipid membranes under oxidative attack. The Journal of Physical Chemistry B 2010, 114, 15642–15649. [PubMed: 21053974]

(139). Mao C; Xiang Y; Liu X; Zheng Y; Yeung KWK; Cui Z; Yang X; Li Z; Liang Y; Zhu S Local photothermal/photodynamic synergistic therapy by disrupting bacterial membrane to accelerate reactive oxygen species permeation and protein leakage. ACS applied materials & interfaces 2019, 11, 17902–17914. [PubMed: 31013044]

(140). Wang S; Wang Y; Peng Y; Yang X Exploring the antibacteria performance of multicolor Ag, Au, and Cu nanoclusters. ACS applied materials & interfaces 2019, 11, 8461–8469. [PubMed: 30714708]

(141). Zhao Y; Hu M; Zhang Y; Liu J; Liu C; Choi SK; Zhang Z; Song L Multifunctional therapeutic strategy of Ag-synergized dual-modality upconversion nanoparticles to achieve the rapid and sustained cidality of methicillin-resistant Staphylococcus aureus. Chemical Engineering Journal 2020, 385, 123980.

(142). Xie X; Mao C; Liu X; Zhang Y; Cui Z; Yang X; Yeung KW; Pan H; Chu PK; Wu S Synergistic bacteria killing through photodynamic and physical actions of graphene oxide/Ag/collagen coating. ACS Applied Materials & Interfaces 2017, 9, 26417–26428. [PubMed: 28715631]

(143). Valliammai A; Sethupathy S; Priya A; Selvaraj A; Bhaskar JP; Krishnan V; Pandian SK 5-Dodecanolide interferes with biofilm formation and reduces the virulence of Methicillin-resistant Staphylococcus aureus (MRSA) through up regulation of agr system. Scientific reports 2019, 9, 1–16. [PubMed: 30626917]

(144). Gaupp R; Ledala N; Somerville GA Staphylococcal response to oxidative stress. Frontiers in cellular and infection microbiology 2012, 2, 33. [PubMed: 22919625]

(145). Ke M-R; Eastel JM; Ngai KL; Cheung Y-Y; Chan PK; Hui M; Ng DK; Lo P-C Photodynamic inactivation of bacteria and viruses using two monosubstituted zinc (II) phthalocyanines. European Journal of Medicinal Chemistry 2014, 84, 278–283. [PubMed: 25036788]

(146). Kashef N; Huang Y-Y; Hamblin MR Advances in antimicrobial photodynamic inactivation at the nanoscale. Nanophotonics 2017, 6, 853–879. [PubMed: 29226063]

(147). Maliszewska I; Lisiak B; Popko K; Matczyszyn K Enhancement of the efficacy of photodynamic inactivation of Candida albicans with the use of biogenic gold nanoparticles. Photochemistry and Photobiology 2017, 93, 1081–1090. [PubMed: 28191638]

(148). Gil-Tomás J; Dekker L; Narband N; Parkin IP; Nair SP; Street C; Wilson M Lethal photosensitisation of bacteria using a tin chlorin e6–glutathione–gold nanoparticle conjugate. Journal of Materials Chemistry 2011, 21, 4189–4196.

(149). Xiao Q; Jaatinen E; Zhu H Direct Photocatalysis for Organic Synthesis by Using Plasmonic - Metal Nanoparticles Irradiated with Visible Light. Chemistry–An Asian Journal 2014, 9, 3046–3064.

(150). Wang C; Astruc D Nanogold plasmonic photocatalysis for organic synthesis and clean energy conversion. Chemical Society Reviews 2014, 43, 7188–7216. [PubMed: 25017125]

(151). Tahir K; Nazir S; Li B; Khan AU; Khan ZUH; Ahmad A; Khan QU; Zhao Y Enhanced visible light photocatalytic inactivation of Escherichia coli using silver nanoparticles as photocatalyst. Journal of Photochemistry and Photobiology B: Biology 2015, 153, 261–266.

(152). Khan S; Runguo W; Tahir K; Jichuan Z; Zhang L Catalytic reduction of 4-nitrophenol and photo inhibition of Pseudomonas aeruginosa using gold nanoparticles as photocatalyst. Journal of Photochemistry and Photobiology B: Biology 2017, 170, 181–187.

(153). Aruda KO; Tagliazucchi M; Sweeney CM; Hannah DC; Schatz GC; Weiss EA Identification of parameters through which surface chemistry determines the lifetimes of hot electrons in small Au nanoparticles. Proceedings of the National Academy of Sciences 2013, 110, 4212–4217.

(154). Bian Z; Tachikawa T; Zhang P; Fujitsuka M; Majima T Au/TiO2 superstructure-based plasmonic photocatalysts exhibiting efficient charge separation and unprecedented activity. Journal of the American Chemical Society 2014, 136, 458–465. [PubMed: 24308587]

(155). Priebe JB; Karnahl M; Junge H; Beller M; Hollmann D; Brückner A Water reduction with visible light: synergy between optical transitions and electron transfer in Au - TiO2 catalysts visualized by in situ EPR spectroscopy. Angewandte Chemie International Edition 2013, 52, 11420–11424. [PubMed: 24030724]

(156). Liga MV; Bryant EL; Colvin VL; Li Q Virus inactivation by silver doped titanium dioxide nanoparticles for drinking water treatment. Water research 2011, 45, 535–544. [PubMed: 20926111]

(157). Wu T-S; Wang K-X; Li G-D; Sun S-Y; Sun J; Chen J-S Montmorillonite-supported Ag/TiO2 nanoparticles: an efficient visible-light bacteria photodegradation material. ACS applied materials & interfaces 2010, 2, 544–550. [PubMed: 20356203]

(158). Adhikari S; Banerjee A; Eswar NK; Sarkar D; Madras G Photocatalytic inactivation of E. coli by ZnO–Ag nanoparticles under solar radiation. RSC Advances 2015, 5, 51067–51077.

(159). Gupta R; Eswar NK; Modak JM; Madras G Effect of morphology of zinc oxide in ZnO-CdS-Ag ternary nanocomposite towards photocatalytic inactivation of E. coli under UV and visible light. Chemical Engineering Journal 2017, 307, 966–980.

(160). Das S; Sinha S; Suar M; Yun S-I; Mishra A; Tripathy SK Solar-photocatalytic disinfection of Vibrio cholerae by using Ag@ ZnO core–shell structure nanocomposites. Journal of Photochemistry and Photobiology B: Biology 2015, 142, 68–76.

(161). Ma S; Zhan S; Jia Y; Shi Q; Zhou Q Enhanced disinfection application of Ag-modified g-C3N4 composite under visible light. Applied Catalysis B: Environmental 2016, 186, 77–87.

(162). Shi H; Wang C; Zhao Y; Liu E; Fan J; Ji Z Highly efficient visible light driven photocatalytic inactivation of E. coli with Ag QDs decorated Z-scheme Bi2S3/SnIn4S8 composite. Applied Catalysis B: Environmental 2019, 254, 403–413.

(163). Xin X; Li S-H; Zhang N; Tang Z-R; Xu Y-J 3D graphene/AgBr/Ag cascade aerogel for efficient photocatalytic disinfection. Applied Catalysis B: Environmental 2019, 245, 343–350.

(164). Shi H; Li G; Sun H; An T; Zhao H; Wong P-K Visible-light-driven photocatalytic inactivation of E. coli by Ag/AgX-CNTs (X= Cl, Br, I) plasmonic photocatalysts: Bacterial performance and deactivation mechanism. Applied Catalysis B: Environmental 2014, 158, 301–307.

(165). Tallósy SP; Janovák L; Nagy E; Deák Á; Juhász Á; Csapó E; Buzás N; Dékány I Adhesion and inactivation of Gram-negative and Gram-positive bacteria on photoreactive TiO2/polymer and Ag–TiO2/polymer nanohybrid films. Applied Surface Science 2016, 371, 139–150.

(166). Sontakke S; Modak J; Madras G Photocatalytic inactivation of Escherischia coli and Pichia pastoris with combustion synthesized titanium dioxide. Chemical engineering journal 2010, 165, 225–233.

(167). Liu Y; Wang X; Yang F; Yang X Excellent antimicrobial properties of mesoporous anatase TiO2 and Ag/TiO2 composite films. Microporous and Mesoporous Materials 2008, 114, 431–439.

(168). Tsen SD; Wu TC; Kiang JG; Tsen KT Prospects for a novel ultrashort pulsed laser technology for pathogen inactivation. J. Biomed. Sci. 2012, 19, 62. [PubMed: 22768792]

(169). Tsen SD; Kibler K; Jacobs B; Fay JC; Podolnikova NP; Ugarova TP; Achilefu S; Tsen KT Selective photonic disinfection of cell culture using a visible ultrashort pulsed laser. IEEE J Sel Top Quantum Electron 2016, 22.

(170). Berchtikou A; Greschner AA; Tijssen P; Gauthier MA; Ozaki T Accelerated inactivation of M13 bacteriophage using millijoule femtosecond lasers. Journal of Biophotonics 2020, 13, e201900001. [PubMed: 31654474]

(171). Tsen S-WD; Chapa T; Beatty W; Tsen K-T; Yu D; Achilefu S Inactivation of enveloped virus by laser-driven protein aggregation. Journal of biomedical optics 2012, 17, 128002. [PubMed: 23224114]

(172). Tsen KT; Tsen S-WD; Sankey OF; Kiang JG Selective inactivation of micro-organisms with near-infrared femtosecond laser pulses. Journal of Physics: Condensed Matter 2007, 19, 472201.

(173). Tsen S-WD; Tsen Y-SD; Tsen K-T; Wu TC Selective inactivation of viruses with femtosecond laser pulses and its potential use for in vitro therapy. Journal of Healthcare Engineering 2010, 1.

(174). Nazari M; Li X; Alibakhshi MA; Yang H; Souza K; Gillespie C; Gummuluru S; Hong MK; Reinhard BM; Korolev KS, Ziegler LD, Zhao Q, Wanunu M Femtosecond photonic viral inactivation probed using solid-state nanopores. Nano Futures 2018, 2, 045005.

(175). Robinson JT; Tabakman SM; Liang Y; Wang H; Sanchez Casalongue H; Vinh D; Dai H Ultrasmall reduced graphene oxide with high near-infrared absorbance for photothermal therapy. Journal of the American Chemical Society 2011, 133, 6825–6831. [PubMed: 21476500]

(176). Wang R; Zhao N; Xu FJ Hollow nanostars with photothermal gold caps and their controlled surface functionalization for complementary therapies. Advanced Functional Materials 2017, 27, 1700256.

(177). Ibelli T; Templeton S; Levi-Polyachenko N Progress on utilizing hyperthermia for mitigating bacterial infections. International Journal of Hyperthermia 2018, 34, 144–156. [PubMed: 29498314]

(178). Nims RW; Plavsic M Polyomavirus inactivation–a review. Biologicals 2013, 41, 63–70. [PubMed: 23116715]

(179). Turcheniuk K; Hage C-H; Spadavecchia J; Serrano AY; Larroulet I; Pesquera A; Zurutuza A; Pisfil MG; Héliot L; Boukaert J Plasmonic photothermal destruction of uropathogenic E. coli with reduced graphene oxide and core/shell nanocomposites of gold nanorods/reduced graphene oxide. Journal of Materials Chemistry B 2015, 3, 375–386. [PubMed: 32262041]

(180). Ko YC; Fang HY; Chen DH Fabrication of Ag/ZnO/reduced graphene oxide nanocomposite for SERS detection and multiway killing of bacteria. Journal of Alloys and Compounds 2017, 695, 1145–1153.

(181). Xia D; Liu H; Xu B; Wang Y; Liao Y; Huang Y; Ye L; He C; Wong PK; Qiu R Single Ag atom engineered 3D-MnO2 porous hollow microspheres for rapid photothermocatalytic inactivation of E. coli under solar light. Applied Catalysis B: Environmental 2019, 245, 177–189.

(182). Santos GM; de Santi Ferrara FI; Zhao F; Rodrigues DF; Shih W-C Photothermal inactivation of heat-resistant bacteria on nanoporous gold disk arrays. Optical Materials Express 2016, 6, 1217–1229.

(183). Loeb SK; Kim J; Jiang C; Early LS; Wei H; Li Q; Kim J-H Nanoparticle enhanced interfacial solar photothermal water disinfection demonstrated in 3-D printed flow-through reactors. Environmental science & technology 2019, 53, 7621–7631. [PubMed: 31184883]

(184). Ocsoy I; Yusufbeyoglu S; Yılmaz V; McLamore ES; Ildız N; Ülgen A DNA aptamer functionalized gold nanostructures for molecular recognition and photothermal inactivation of methicillin-Resistant Staphylococcus aureus. Colloids and Surfaces B: Biointerfaces 2017, 159, 16–22. [PubMed: 28778062]

(185). Peng Y; Liu Y; Lu X; Wang S; Chen M; Huang W; Wu Z; Lu G; Nie L Ag-hybridized plasmonic Au-triangular nanoplates: highly sensitive photoacoustic/Raman evaluation and improved antibacterial/photothermal combination therapy. Journal of Materials Chemistry B 2018, 6, 2813–2820. [PubMed: 32254234]

(186). Yang G; Yin H; Liu W; Yang Y; Zou Q; Luo L; Li H; Huo Y; Li H Synergistic Ag/TiO2-N photocatalytic system and its enhanced antibacterial activity towards Acinetobacter baumannii. Applied Catalysis B: Environmental 2018, 224, 175–182.

(187). Li M; Huang L; Wang X; Song Z; Zhao W; Wang Y; Liu J Direct generation of Ag nanoclusters on reduced graphene oxide nanosheets for efficient catalysis, antibacteria and photothermal anticancer applications. Journal of colloid and interface science 2018, 529, 444–451. [PubMed: 30078416]

(188). Santos GM; de Santi Ferrara FI; Zhao F; Rodrigues DF; Shih W-C In Tilte2016; International Society for Optics and Photonics.

(189). Xu M-L; Guan L-Y; Li S-K; Chen L; Chen Z Stable gold graphitic nanocapsule doped hydrogels for efficient photothermal antibacterial applications. Chemical Communications 2019, 55, 5359–5362. [PubMed: 30994651]

(190). Bucharskaya A; Maslyakova G; Terentyuk G; Yakunin A; Avetisyan Y; Bibikova O; Tuchina E; Khlebtsov B; Khlebtsov N; Tuchin V Towards effective photothermal/photodynamic treatment using plasmonic gold nanoparticles. International journal of molecular sciences 2016, 17, 1295.

(191). Morones-Ramirez JR; Winkler JA; Spina CS; Collins JJ Silver enhances antibiotic activity against gram-negative bacteria. Science translational medicine 2013, 5, 190ra181–190ra181.

(192). Marambio-Jones C; Hoek EM A review of the antibacterial effects of silver nanomaterials and potential implications for human health and the environment. Journal of Nanoparticle Research 2010, 12, 1531–1551.

(193). Lara HH; Ayala-Nuñez NV; Ixtepan-Turrent L; Rodriguez-Padilla C Mode of antiviral action of silver nanoparticles against HIV-1. Journal of nanobiotechnology 2010, 8, 1–10. [PubMed: 20145735]

(194). Broglie JJ; Alston B; Yang C; Ma L; Adcock AF; Chen W; Yang L Antiviral activity of gold/copper sulfide core/shell nanoparticles against human norovirus virus-like particles. PloS one 2015, 10, e0141050. [PubMed: 26474396]

(195). Adhikari MD; Goswami S; Panda BR; Chattopadhyay A; Ramesh A Membrane - Directed High Bactericidal Activity of (Gold Nanoparticle) – Polythiophene Composite for Niche Applications Against Pathogenic Bacteria. Advanced healthcare materials 2013, 2, 599–606. [PubMed: 23184755]

(196). Cagno V; Andreozzi P; D'Alicarnasso M; Silva PJ; Mueller M; Galloux M; Le Goffic R; Jones ST; Vallino M; Hodek J Broad-spectrum non-toxic antiviral nanoparticles with a virucidal inhibition mechanism. Nature materials 2018, 17, 195–203. [PubMed: 29251725]

(197). Zhao Y; Tian Y; Cui Y; Liu W; Ma W; Jiang X Small molecule-capped gold nanoparticles as potent antibacterial agents that target gram-negative bacteria. Journal of the American Chemical Society 2010, 132, 12349–12356. [PubMed: 20707350]

(198). Tatur S; Maccarini M; Barker R; Nelson A; Fragneto G Effect of functionalized gold nanoparticles on floating lipid bilayers. Langmuir 2013, 29, 6606–6614. [PubMed: 23638939]

(199). Pillai PP; Kowalczyk B; Kandere - Grzybowska K; Borkowska M; Grzybowski BA Engineering gram selectivity of mixed - charge gold nanoparticles by tuning the balance of surface charges. Angewandte Chemie International Edition 2016, 55, 8610–8614. [PubMed: 27253138]

(200). Morones JR; Elechiguerra JL; Camacho A; Holt K; Kouri JB; Ramírez JT; Yacaman MJ The bactericidal effect of silver nanoparticles. Nanotechnology 2005, 16, 2346. [PubMed: 20818017]

(201). Peretyazhko TS; Zhang Q; Colvin VL Size-controlled dissolution of silver nanoparticles at neutral and acidic pH conditions: kinetics and size changes. Environmental science & technology 2014, 48, 11954–11961. [PubMed: 25265014]

(202). Tanneru CT; Hill VR; Chellam S Relative insignificance of virus inactivation during aluminum electrocoagulation of saline waters. Environmental science & technology 2014, 48, 14590–14598. [PubMed: 25405814]

(203). Radzig M; Koksharova O; Khmel I; Ivanov V; Yorov K; Kiwi J; Rtimi S; Tastekova E; Aybush A; Nadtochenko V Femtosecond spectroscopy of Au hot-electron injection into TiO2: Evidence for Au/TiO2 plasmon photocatalysis by bactericidal Au ions and related phenomena. Nanomaterials 2019, 9, 217.

(204). Li F; Lei C; Shen Q; Li L; Wang M; Guo M; Huang Y; Nie Z; Yao S Analysis of copper nanoparticles toxicity based on a stress-responsive bacterial biosensor array. Nanoscale 2013, 5, 653–662. [PubMed: 23223666]

(205). Kim T; Feng QL; Kim J; Wu J; Wang H; Chen G; Cui F Antimicrobial effects of metal ions (Ag +, Cu2+, Zn2+) in hydroxyapatite. Journal of materials science: Materials in Medicine 1998, 9, 129–134. [PubMed: 15348901]

(206). Jung WK; Koo HC; Kim KW; Shin S; Kim SH; Park YH Antibacterial activity and mechanism of action of the silver ion in Staphylococcus aureus and Escherichia coli. Applied and environmental microbiology 2008, 74, 2171–2178. [PubMed: 18245232]

(207). Rtimi S; Nadtochenko V; Khmel I; Kiwi J Evidence for differentiated ionic and surface contact effects driving bacterial inactivation by way of genetically modified bacteria. Chemical Communications 2017, 53, 9093–9096. [PubMed: 28758649]

(208). Ramalingam B; Parandhaman T; Das SK Antibacterial effects of biosynthesized silver nanoparticles on surface ultrastructure and nanomechanical properties of gram-negative bacteria viz. Escherichia coli and Pseudomonas aeruginosa. ACS applied materials & interfaces 2016, 8, 4963–4976. [PubMed: 26829373]

(209). Chu Y; Tan X; Shen Z; Liu P; Han N; Kang J; Duan X; Wang S; Liu L; Liu S Efficient removal of organic and bacterial pollutants by Ag-La0. 8Ca0. 2Fe0. 94O3-δ perovskite via catalytic peroxymonosulfate activation. Journal of hazardous materials 2018, 356, 53–60. [PubMed: 29807239]

(210). Hamida RS; Ali MA; Goda DA; Khalil MI; Al-Zaban MI Novel biogenic silver nanoparticle-induced reactive oxygen species inhibit the biofilm formation and virulence activities of methicillin-resistant staphylococcus aureus (MRSA) strain. Frontiers in bioengineering and biotechnology 2020, 8.

(211). Nagy A; Harrison A; Sabbani S; Munson RS Jr; Dutta PK; Waldman WJ Silver nanoparticles embedded in zeolite membranes: release of silver ions and mechanism of antibacterial action. International journal of nanomedicine 2011, 6, 1833. [PubMed: 21931480]

(212). Geilich BM; van de Ven AL; Singleton GL; Sepúlveda LJ; Sridhar S; Webster TJ Silver nanoparticle-embedded polymersome nanocarriers for the treatment of antibiotic-resistant infections. Nanoscale 2015, 7, 3511–3519. [PubMed: 25628231]

(213). Pornpattananangkul D; Zhang L; Olson S; Aryal S; Obonyo M; Vecchio K; Huang C-M; Zhang L Bacterial toxin-triggered drug release from gold nanoparticle-stabilized liposomes for the treatment of bacterial infection. Journal of the American Chemical Society 2011, 133, 4132–4139. [PubMed: 21344925]

(214). Wang Y; Ding X; Chen Y; Guo M; Zhang Y; Guo X; Gu H Antibiotic-loaded, silver core-embedded mesoporous silica nanovehicles as a synergistic antibacterial agent for the treatment of drug-resistant infections. Biomaterials 2016, 101, 207–216. [PubMed: 27294538]

(215). Song Z; Ma Y; Xia G; Wang Y; Kapadia W; Sun Z; Wu W; Gu H; Cui W; Huang X In vitro and in vivo combined antibacterial effect of levofloxacin/silver co-loaded electrospun fibrous membranes. Journal of Materials Chemistry B 2017, 5, 7632–7643. [PubMed: 32264238]

(216). Fayaz AM; Balaji K; Girilal M; Yadav R; Kalaichelvan PT; Venketesan R Biogenic synthesis of silver nanoparticles and their synergistic effect with antibiotics: a study against gram-positive and gram-negative bacteria. Nanomedicine: Nanotechnology, Biology and Medicine 2010, 6, 103–109.

(217). Shahverdi AR; Fakhimi A; Shahverdi HR; Minaian S Synthesis and effect of silver nanoparticles on the antibacterial activity of different antibiotics against Staphylococcus aureus and Escherichia coli. Nanomedicine: Nanotechnology, Biology and Medicine 2007, 3, 168–171.

(218). Lee KH; Zeng H Aptamer-based ELISA assay for highly specific and sensitive detection of Zika NS1 protein. Analytical chemistry 2017, 89, 12743–12748. [PubMed: 29120623]

(219). Aw TG; Rose JB Detection of pathogens in water: from phylochips to qPCR to pyrosequencing. Current opinion in biotechnology 2012, 23, 422–430. [PubMed: 22153035]

(220). Haynes CL; McFarland AD; Van Duyne RP: Surface-enhanced Raman spectroscopy. ACS Publications, 2005.

(221). Rusciano G; Zito G; Isticato R; Sirec T; Ricca E; Bailo E; Sasso A Nanoscale chemical imaging of Bacillus subtilis spores by combining tip-enhanced Raman scattering and advanced statistical tools. ACS nano 2014, 8, 12300–12309. [PubMed: 25415422]

(222). Cialla D; Deckert-Gaudig T; Budich C; Laue M; Möller R; Naumann D; Deckert V; Popp J Raman to the limit: tip - enhanced Raman spectroscopic investigations of a single tobacco mosaic virus. Journal of Raman Spectroscopy: An International Journal for Original Work in all Aspects of Raman Spectroscopy, Including Higher Order Processes, and also Brillouin and Rayleigh Scattering 2009, 40, 240–243.

(223). Neugebauer U; Rösch P; Schmitt M; Popp J; Julien C; Rasmussen A; Budich C; Deckert V On the way to nanometer - sized information of the bacterial surface by tip - enhanced Raman spectroscopy. Chemphyschem: a European journal of chemical physics and physical chemistry 2006, 7, 1428–1430. [PubMed: 16789043]

(224). Zhang R; Hong Y; Reinhard BM; Liu P; Wang R; Dal Negro L Plasmonic nanotrough networks for scalable bacterial Raman biosensing. ACS applied materials & interfaces 2018, 10, 27928–27935. [PubMed: 30051708]

(225). Fan Z; Yust B; Nellore BPV; Sinha SS; Kanchanapally R; Crouch RA; Pramanik A; Chavva SR; Sardar D; Ray PC Accurate identification and selective removal of rotavirus using a plasmonic–magnetic 3D graphene oxide architecture. The Journal of Physical Chemistry Letters 2014, 5, 3216–3221. [PubMed: 26276335]

(226). Premasiri WR; Lee JC; Sauer-Budge A; Theberge R; Costello CE; Ziegler LD The biochemical origins of the surface-enhanced Raman spectra of bacteria: a metabolomics profiling by SERS. Analytical and bioanalytical chemistry 2016, 408, 4631–4647. [PubMed: 27100230]

(227). Walter A; März A; Schumacher W; Rösch P; Popp J Towards a fast, high specific and reliable discrimination of bacteria on strain level by means of SERS in a microfluidic device. Lab on a Chip 2011, 11, 1013–1021. [PubMed: 21283864]

(228). Harz M; Kiehntopf M; Stöckel S; Rösch P; Straube E; Deufel T; Popp J Direct analysis of clinical relevant single bacterial cells from cerebrospinal fluid during bacterial meningitis by means of micro-Raman spectroscopy. Journal of biophotonics 2009, 2, 70–80. [PubMed: 19343686]

(229). Jarvis RM; Goodacre R Discrimination of bacteria using surface-enhanced Raman spectroscopy. Analytical chemistry 2004, 76, 40–47. [PubMed: 14697030]

(230). Wu X; Xu C; Tripp RA; Huang Y.-w.; Zhao Y Detection and differentiation of foodborne pathogenic bacteria in mung bean sprouts using field deployable label-free SERS devices. Analyst 2013, 138, 3005–3012. [PubMed: 23563168]

(231). Kearns H; Goodacre R; Jamieson LE; Graham D; Faulds K SERS detection of multiple antimicrobial-resistant pathogens using nanosensors. Analytical chemistry 2017, 89, 12666–12673. [PubMed: 28985467]

(232). Zhang L; Xu J; Mi L; Gong H; Jiang S; Yu Q Multifunctional magnetic–plasmonic nanoparticles for fast concentration and sensitive detection of bacteria using SERS. Biosensors and Bioelectronics 2012, 31, 130–136. [PubMed: 22036668]

(233). Xu J; Zhang L; Gong H; Homola J. í.; Yu Q Tailoring plasmonic nanostructures for optimal SERS sensing of small molecules and large microorganisms. Small 2011, 7, 371–376. [PubMed: 21294266]

(234). Thrift WJ; Ronaghi S; Samad M; Wei H; Nguyen DG; Cabuslay AS; Groome CE; Santiago PJ; Baldi P; Hochbaum AI Deep Learning Analysis of Vibrational Spectra of Bacterial Lysate for Rapid Antimicrobial Susceptibility Testing. ACS nano 2020.

(235). Alexander TA; Pellegrino PM; Gillespie JB Near-infrared surface-enhanced-Raman-scattering-mediated detection of single optically trapped bacterial spores. Applied spectroscopy 2003, 57, 1340–1345. [PubMed: 14658146]

(236). Paul AM; Fan Z; Sinha SS; Shi Y; Le L; Bai F; Ray PC Bioconjugated gold nanoparticle based SERS probe for ultrasensitive identification of mosquito-borne viruses using raman fingerprinting. The Journal of Physical Chemistry C 2015, 119, 23669–23675.

(237). Rösch P; Harz M; Schmitt M; Popp J Raman spectroscopic identification of single yeast cells. Journal of Raman Spectroscopy: An International Journal for Original Work in all Aspects of Raman Spectroscopy, Including Higher Order Processes, and also Brillouin and Rayleigh Scattering 2005, 36, 377–379.

(238). Cao YC; Jin R; Mirkin CA Nanoparticles with Raman spectroscopic fingerprints for DNA and RNA detection. Science 2002, 297, 1536–1540. [PubMed: 12202825]

(239). Li M; Cushing SK; Liang H; Suri S; Ma D; Wu N Plasmonic nanorice antenna on triangle nanoarray for surface-enhanced Raman scattering detection of hepatitis B virus DNA. Analytical chemistry 2013, 85, 2072–2078. [PubMed: 23320458]

(240). Xu S; Ji X; Xu W; Li X; Wang L; Bai Y; Zhao B; Ozaki Y Immunoassay using probe-labelling immunogold nanoparticles with silver staining enhancement via surface-enhanced Raman scattering. Analyst 2004, 129, 63–68. [PubMed: 14737585]

(241). Wang H; Zhou Y; Jiang X; Sun B; Zhu Y; Wang H; Su Y; He Y Simultaneous capture, detection, and inactivation of bacteria as enabled by a Surface - Enhanced raman scattering multifunctional chip. Angewandte Chemie 2015, 127, 5221–5225.

(242). Ochmann SE; Vietz C; Trofymchuk K; Acuna GP; Lalkens B; Tinnefeld P Optical nanoantenna for single molecule-based detection of zika virus nucleic acids without molecular multiplication. Analytical chemistry 2017, 89, 13000–13007. [PubMed: 29144729]

(243). Flynn JD; Haas BL; Biteen JS Plasmon-enhanced fluorescence from single proteins in living bacteria. The Journal of Physical Chemistry C 2016, 120, 20512–20517.

(244). Chan P-H; Chen Y-C Human serum albumin stabilized gold nanoclusters as selective luminescent probes for Staphylococcus aureus and methicillin-resistant Staphylococcus aureus. Analytical chemistry 2012, 84, 8952–8956. [PubMed: 23088348]

(245). Ashiba H; Iizumi Y; Okazaki T; Wang X; Fujimaki M Carbon Nanotubes as Fluorescent Labels for Surface Plasmon Resonance-Assisted Fluoroimmunoassay. Sensors 2017, 17, 2569.

(246). Nasrin F; Chowdhury AD; Takemura K; Kozaki I; Honda H; Adegoke O; Park EY Fluorometric virus detection platform using quantum dots-gold nanocomposites optimizing the linker length variation. Analytica Chimica Acta 2020.

(247). Lee J; Ahmed SR; Oh S; Kim J; Suzuki T; Parmar K; Park SS; Lee J; Park EY A plasmon-assisted fluoro-immunoassay using gold nanoparticle-decorated carbon nanotubes for monitoring the influenza virus. Biosensors and Bioelectronics 2015, 64, 311–317. [PubMed: 25240957]

(248). Ashiba H; Sugiyama Y; Wang X; Shirato H; Higo-Moriguchi K; Taniguchi K; Ohki Y; Fujimaki M Detection of norovirus virus-like particles using a surface plasmon resonance-assisted fluoroimmunosensor optimized for quantum dot fluorescent labels. Biosensors and Bioelectronics 2017, 93, 260–266. [PubMed: 27597126]

(249). Wang X; Cui Q; Yao C; Li S; Zhang P; Sun H; Lv F; Liu L; Li L; Wang S Conjugated polyelectrolyte–silver nanostructure pair for detection and killing of bacteria. Advanced Materials Technologies 2017, 2, 1700033.

(250). Takemura K; Adegoke O; Takahashi N; Kato T; Li T-C; Kitamoto N; Tanaka T; Suzuki T; Park EY Versatility of a localized surface plasmon resonance-based gold nanoparticle-alloyed quantum dot nanobiosensor for immunofluorescence detection of viruses. Biosensors and Bioelectronics 2017, 89, 998–1005. [PubMed: 27825520]

(251). Nasrin F; Chowdhury AD; Takemura K; Lee J; Adegoke O; Deo VK; Abe F; Suzuki T; Park EY Single-step detection of norovirus tuning localized surface plasmon resonance-induced optical signal between gold nanoparticles and quantum dots. Biosensors and Bioelectronics 2018, 122, 16–24. [PubMed: 30236804]

(252). Draz MS; Fang BA; Li L; Chen Z; Wang Y; Xu Y; Yang J; Killeen K; Chen FF Hybrid nanocluster plasmonic resonator for immunological detection of hepatitis B virus. ACS nano 2012, 6, 7634–7643. [PubMed: 22934963]

(253). Baccar H; Mejri M; Hafaiedh I; Ktari T; Aouni M; Abdelghani A Surface plasmon resonance immunosensor for bacteria detection. Talanta 2010, 82, 810–814. [PubMed: 20602974]

(254). Wang X; Li Y; Wang H; Fu Q; Peng J; Wang Y; Du J; Zhou Y; Zhan L Gold nanorod-based localized surface plasmon resonance biosensor for sensitive detection of hepatitis B virus in buffer, blood serum and plasma. Biosensors and Bioelectronics 2010, 26, 404–410. [PubMed: 20729056]

(255). Yoo SM; Kim D-K; Lee SY Aptamer-functionalized localized surface plasmon resonance sensor for the multiplexed detection of different bacterial species. Talanta 2015, 132, 112–117. [PubMed: 25476286]

(256). Chen C-D; Cheng S-F; Chau L-K; Wang CC Sensing capability of the localized surface plasmon resonance of gold nanorods. Biosensors and Bioelectronics 2007, 22, 926–932. [PubMed: 16697633]

(257). Nath S; Kaittanis C; Tinkham A; Perez JM Dextran-coated gold nanoparticles for the assessment of antimicrobial susceptibility. Analytical chemistry 2008, 80, 1033–1038. [PubMed: 18198893]

(258). Tawil N; Sacher E; Mandeville R; Meunier M Surface plasmon resonance detection of E. coli and methicillin-resistant S. aureus using bacteriophages. Biosensors and Bioelectronics 2012, 37, 24–29. [PubMed: 22609555]

(259). Lee T; Kim GH; Kim SM; Hong K; Kim Y; Park C; Sohn H; Min J Label-free localized surface plasmon resonance biosensor composed of multi-functional DNA 3 way junction on hollow Au spike-like nanoparticles (HAuSN) for avian influenza virus detection. Colloids and Surfaces B: Biointerfaces 2019, 182, 110341. [PubMed: 31284148]

(260). Wang S; Shan X; Patel U; Huang X; Lu J; Li J; Tao N Label-free imaging, detection, and mass measurement of single viruses by surface plasmon resonance. Proceedings of the National Academy of Sciences 2010, 107, 16028–16032.

(261). Shedbalkar U; Singh R; Wadhwani S; Gaidhani S; Chopade B Microbial synthesis of gold nanoparticles: current status and future prospects. Advances in colloid and interface science 2014, 209, 40–48. [PubMed: 24456802]

(262). Sojinrin T; Conde J; Liu K; Curtin J; Byrne HJ; Cui D; Tian F Plasmonic gold nanoparticles for detection of fungi and human cutaneous fungal infections. Analytical and bioanalytical chemistry 2017, 409, 4647–4658. [PubMed: 28573322]

(263). Kaushik A; Yndart A; Kumar S; Jayant RD; Vashist A; Brown AN; Li C-Z; Nair M A sensitive electrochemical immunosensor for label-free detection of Zika-virus protein. Scientific reports 2018, 8, 1–5. [PubMed: 29311619]

(264). Wang S; Li L; Jin H; Yang T; Bao W; Huang S; Wang J Electrochemical detection of hepatitis B and papilloma virus DNAs using SWCNT array coated with gold nanoparticles. Biosensors and Bioelectronics 2013, 41, 205–210. [PubMed: 22947516]

(265). Lv X; Ge W; Li Q; Wu Y; Jiang H; Wang X Rapid and ultrasensitive electrochemical detection of multidrug-resistant bacteria based on nanostructured gold coated ITO electrode. ACS applied materials & interfaces 2014, 6, 11025–11031. [PubMed: 24950258]

(266). Zhu F; Zhao G; Dou W A non-enzymatic electrochemical immunoassay for quantitative detection of Escherichia coli O157: H7 using Au@ Pt and graphene. Analytical biochemistry 2018, 559, 34–43. [PubMed: 30144412]

(267). Li K; Lai Y; Zhang W; Jin L Fe2O3@ Au core/shell nanoparticle-based electrochemical DNA biosensor for Escherichia coli detection. Talanta 2011, 84, 607–613. [PubMed: 21482257]

(268). Lee J-H; Oh B-K; Choi J-W Electrochemical sensor based on direct electron transfer of HIV-1 Virus at Au nanoparticle modified ITO electrode. Biosensors and Bioelectronics 2013, 49, 531–535. [PubMed: 23816850]

(269). Liu C; Dong J; Waterhouse GI; Cheng Z; Ai S Electrochemical immunosensor with nanocellulose-Au composite assisted multiple signal amplification for detection of avian leukosis virus subgroup J. Biosensors and Bioelectronics 2018, 101, 110–115. [PubMed: 29055192]

(270). Lee T; Park SY; Jang H; Kim G-H; Lee Y; Park C; Mohammadniaei M; Lee M-H; Min J Fabrication of electrochemical biosensor consisted of multi-functional DNA structure/porous au nanoparticle for avian influenza virus (H5N1) in chicken serum. Materials Science and Engineering: C 2019, 99, 511–519. [PubMed: 30889726]

(271). Mantri Y; Jokerst JV Engineering Plasmonic Nanoparticles for Enhanced Photoacoustic Imaging. ACS nano 2020, 14, 9408–9422. [PubMed: 32806027]

(272). Beard P Biomedical photoacoustic imaging. Interface focus 2011, 1, 602–631. [PubMed: 22866233]

(273). Kim T; Zhang Q; Li J; Zhang L; Jokerst JV A gold/silver hybrid nanoparticle for treatment and photoacoustic imaging of bacterial infection. ACS nano 2018, 12, 5615–5625. [PubMed: 29746090]

(274). Lu SZ; Guo XY; Zou MS; Zheng ZQ; Li YC; Li XD; Li LL; Wang H Bacteria - Instructed In Situ Aggregation of AuNPs with Enhanced Photoacoustic Signal for Bacterial Infection Bioimaging. Advanced Healthcare Materials 2020, 9, 1901229.

(275). Chen YS; Frey W; Aglyamov S; Emelianov S Environment - dependent generation of photoacoustic waves from plasmonic nanoparticles. Small 2012, 8, 47–52. [PubMed: 22114029]

(276). Liu Y; Lin A; Liu J; Chen X; Zhu X; Gong Y; Yuan G; Chen L; Liu J Enzyme-responsive Mesoporous Ruthenium for Combined Chemo-photothermal Therapy of Drug-resistant Bacteria. ACS applied materials & interfaces 2019.

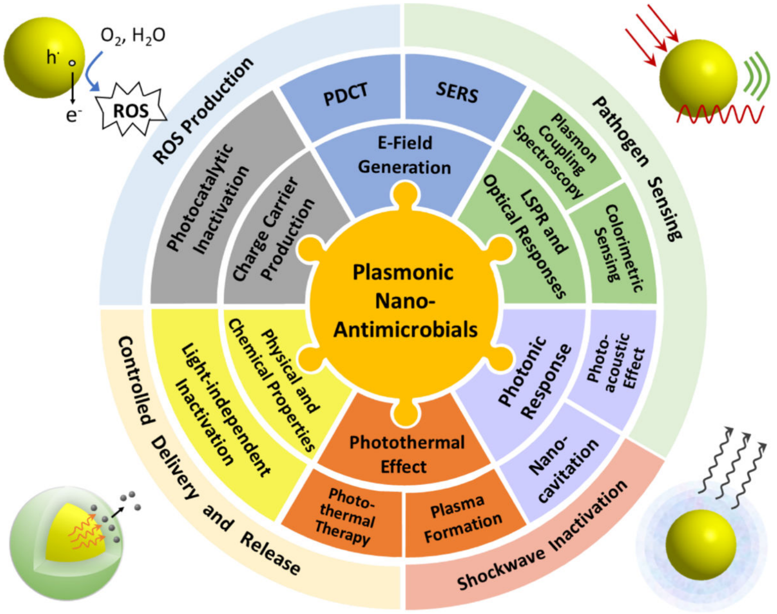

Figure 1.

Properties and Inactivation Mechanisms of Plasmonic Nano-Antimicrobials.

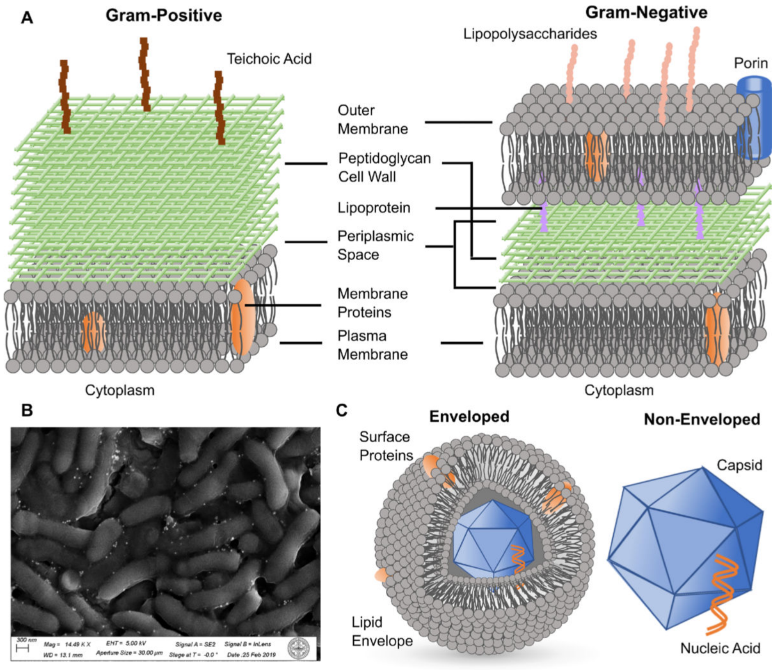

Figure 2. Microbial Pathogens.

(A) Scheme of the cell wall and membrane structures of Gram-positive (left) and Gram-negative (right) bacteria.

(B) SEM micrograph of a biofilm formed from *Arthrobacter sp*. mixed with Ag NPs.

(C) Scheme of the structures of enveloped (left) and non-enveloped (right) viruses.

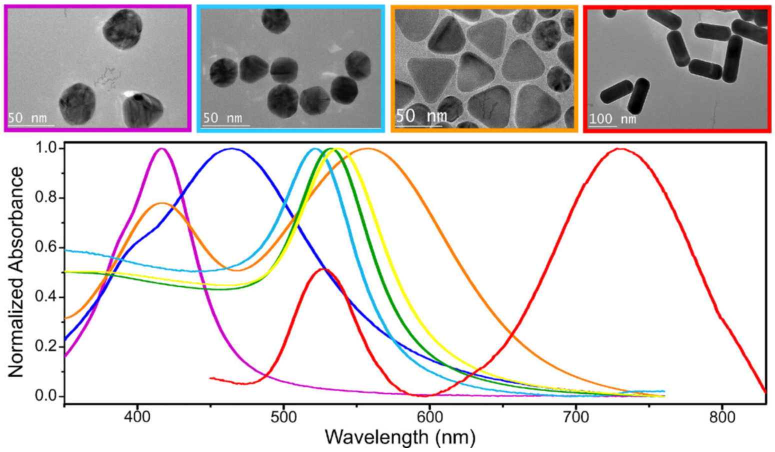

Figure 3. TEM Micrographs (top) and Absorbance Spectra (bottom) of Different Plasmonic Nanostructures.

Color code: 40 nm (purple) and 80 nm (blue) Ag nanospheres; 40 nm (cyan), 60 nm (green) and 80 nm (yellow) Au nanospheres; Ag nanoplates (orange); and Au nanorods (red).

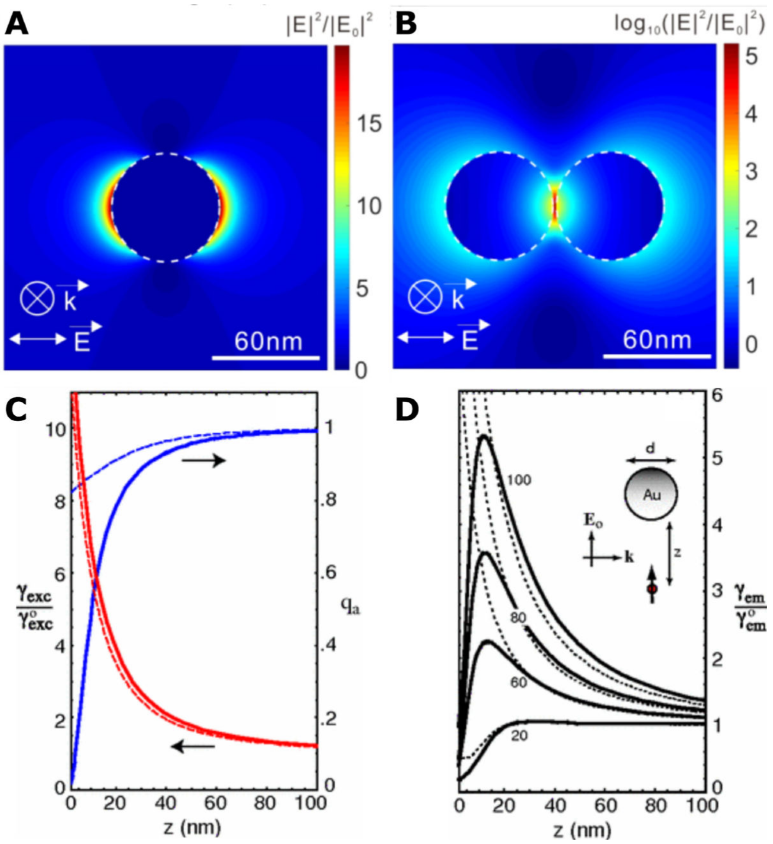

Figure 4. Plasmonic E-Field Generation and Enhancement of Molecular Excitation and Emissions.

(A, B) Calculated E-field intensity maps for a 60 nm Au NP monomer (A) and dimer (B). Reproduced from Ref. 35. © IOP Publishing. Reproduced with permission. All rights reserved.

(C, D) Calculated quantum yield q_a, excitation rate γ_{exc} and fluorescence emission rate γ_{em} normalized with free-space values as a function of fluorophore-metal separation for 80 nm Au NPs (C) and Au NPs with various diameters (D). Solid curves: MMP calculations, dashed curves: dipole approximation. Reprinted figures with permission from [Anger, P.; Bharadwaj, P.; Novotny, L. *Physical review letters 96*, 113002, 2006. https://doi.org/10.1103/PhysRevLett.96.113002]. Copyright (2006) by the American Physical Society.

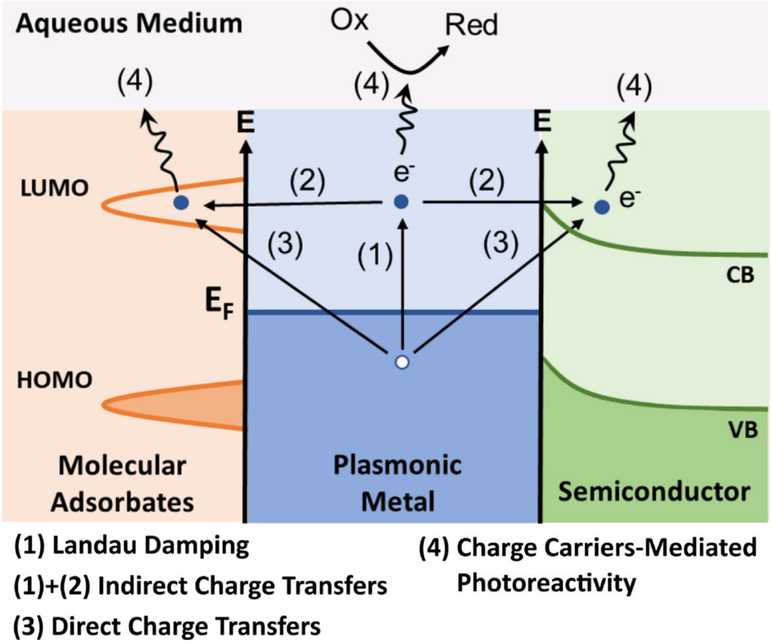

Figure 5.

Mechanisms of Plasmonic Charge Carrier Production.

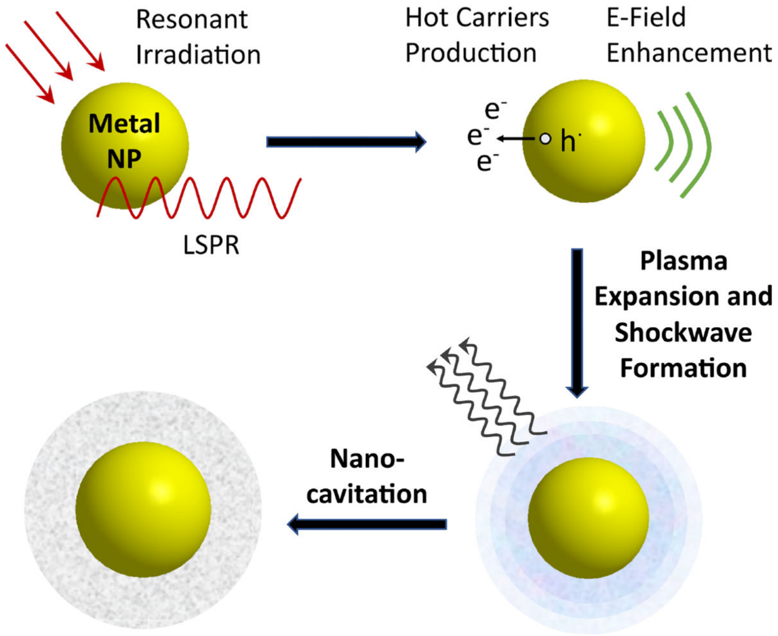

Figure 6.

Scheme of Plasmon-Enhanced Nanocavitation and Shockwave Formation under Resonant Pulsed Laser Irradiation.

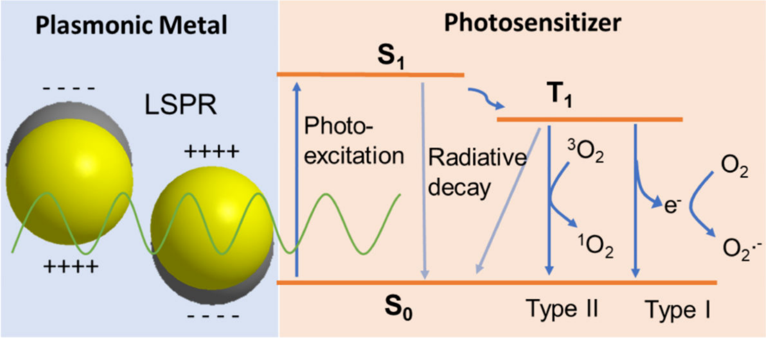

Figure 7.

Scheme for Photophysical Processes in PDCT.

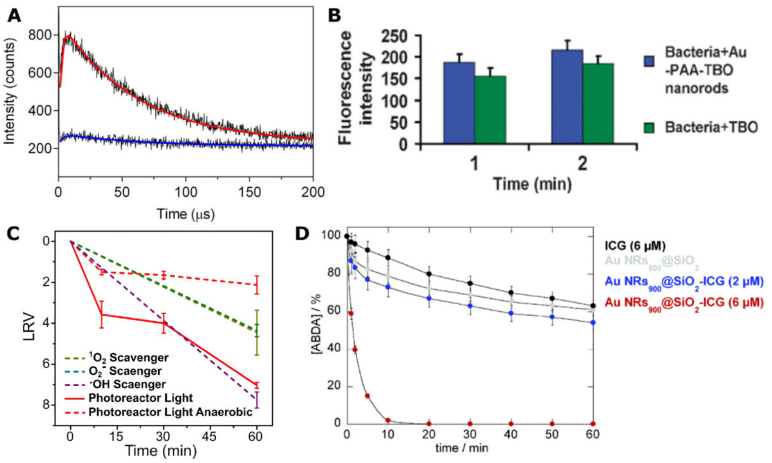

Figure 8. Evidence for ROS Generation in PDCT.

(A) Time-resolved luminescence of $^1O_2$ and biexponential fits at 1275 nm for hybrid plasmonic nanoparticles (red) and an etched control (blue). Reprinted with permission from Ref. 97. Copyright (2016) American Chemical Society.

(B) Fluorescence intensity of singlet oxygen sensor green staining for MRSA treated with Au NRs-TBO system or just with TBO for 1 or 2 min. Reproduced from Ref. 119 with permission from The Royal Society of Chemistry.

(C) Inactivation curves for Ag-$[Ru(bpy)_3]^{2+}$ photoreactor system without (red, solid) or with different ROS scavengers (dashed). Reprinted with permission from Ref. 118. Copyright (2020) American Chemical Society.

(D) ABDA degradation curve with Au NRs@SiO_2 nanocomposites incorporating various concentrations of indocyanine green. Reproduced from Ref. 84 with permission from The Royal Society of Chemistry.

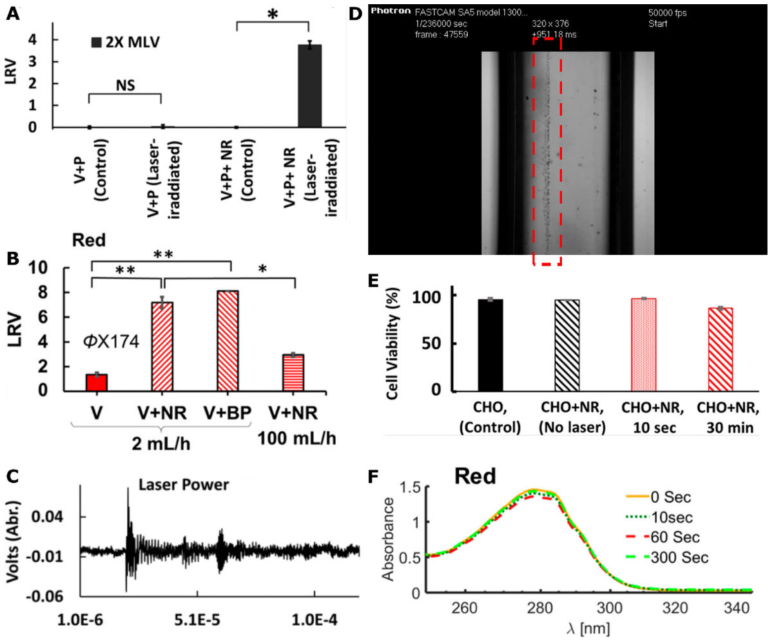

Figure 9. Characterizations of Shockwave Inactivation Mechanism.

(A) Photonic inactivation of MLVs (V) with Au NRs (NR) and pulsed NIR laser illumination in the presence of IgG antibody (P). NS: non-significant difference; *: significant level $P < 0.05$.

(B) Photonic inactivation of ϕX174 (V) with NIR pulsed laser and Au NRs or BPs. *: $P<0.05$; **: $P<0.005$.

(C) Evidence of shockwave emission recorded by a photoacoustic transducer.

(D) Image of bubble formation during nanocavitation experiment using a 700 nm Ti:Sapphire laser with 35 fs pulses and Au NPs. Bubble formation along the laser path is highlighted by the red rectangle.

(E-F) Effect of shockwave inactivation of NIR laser and Au NRs on (E) mammalian cells, and (F) monoclonal antibodies measured by UV-vis absorption spectrum of antibody before or after different times of illumination.

(A, C) Reproduced from Ref. 42 under the CC BY 4.0 Creative Commons license.

(B, E, F) Reprinted with permission from Ref. 86. Copyright (2019) American Chemical Society.

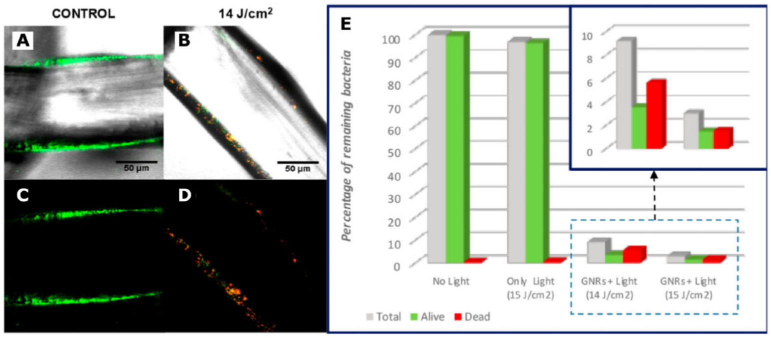

Figure 10. Photothermal Inactivation of *S. aureus* Biofilm on Surgical Meshes by Au NRs.

(A-D) Fluorescence confocal microscope images at the mesh surfaces for no illumination control (A, C) and group treated with 300 ms-pulsed NIR laser with fluence of 14 J/cm^2 (B, D). A, B are a merge of bright field images with fluorescence images, and C, D are pure fluorescence maps. (E) Proportion of alive bacteria at the mesh surface after treatment with different laser fluences.

(A-E) Adapted with permission from Ref. 67. Copyright (2019) American Chemical Society.

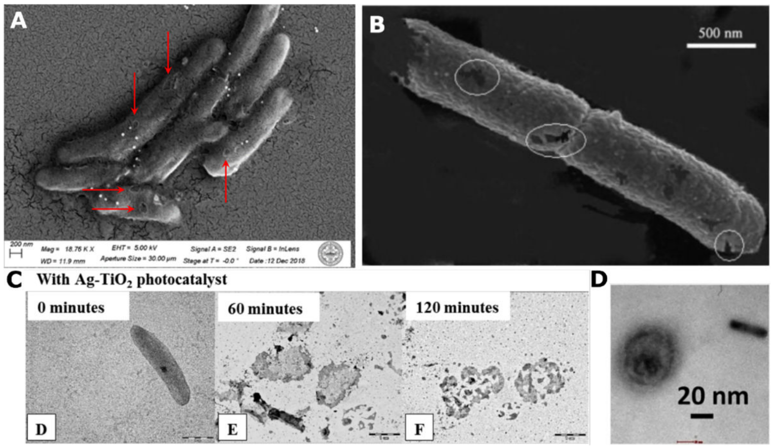

Figure 11. Pathogen Structural Damages Produced by Light-Induced Inactivation Pathways of Plasmonic Nano-Antimicrobials.

(A) SEM image of pore formation found on *Arthrobacter sp.* bacteria cell body after PDCT treatment for 1 hour with Ag / $[Ru(bpy)_3]^{2+}$ photoreactor nanocomposites and 430 nm LED. Reprinted with permission from Ref. 118. Copyright (2020) American Chemical Society.

(B) SEM image of pore formation on *E. coli* cell body after PC inactivation with Ag/TiO_2 composite film and UV LED for 5 min. Reprinted from Ref. 167, Copyright (2008), with permission from Elsevier.

(C) TEM images of cell rupture of *E. coli* after PC inactivation with Ag/TiO_2 nanohybrid films and 405 nm LED for 0, 60 and 120 min. Reprinted from Ref. 165, Copyright (2016), with permission from Elsevier.

(D) TEM image of structural damage to MLV after Au NRs-assisted photonic shockwave inactivation 805 nm fs pulsed laser treatment for 10 seconds. Reproduced from Ref. 42 under the CC By 4.0 Creative Commons license.

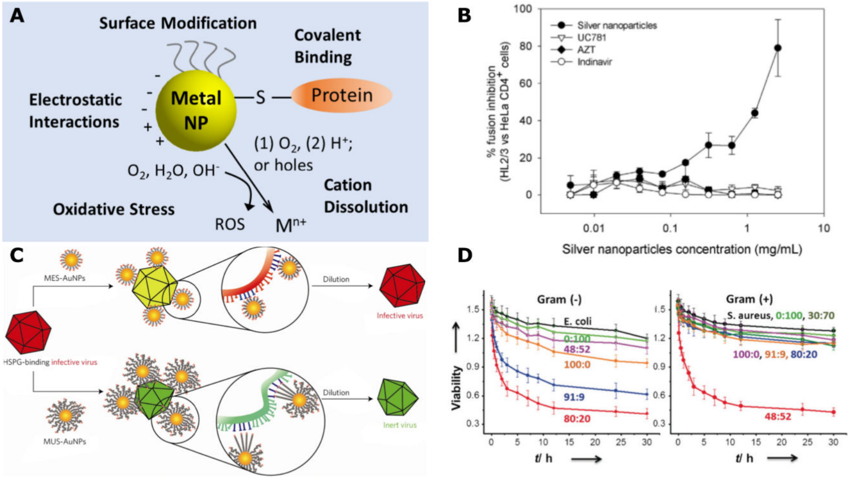

Figure 12. Light-Independent Inactivation Pathways of Plasmonic Nano-Antimicrobials.

(A) Scheme for light-independent interaction modes of plasmonic metal NPs with microbial pathogens.

(B) Fusion assay mimicking gp120-CD4 binding based on HIV-1 Env-expressing HL2/3 cells and HeLa-CD4-LTR-β-gal cells. Reproduced from Ref. 193 under the CC BY 2.0 Creative Commons license.

(C) Scheme for the virucidal activity of MES-Au NPs and MUS-Au NPs. Reprinted by permission from Springer Nature, Nature Materials. Ref. 196. COPYRIGHT (2017).

(D) Quantification of the antibacterial activity and Gram selectivity for 5.2 nm Au NPs with different positive:negative ligand ratios. Reproduced from Ref. 199. © 2016 WILEY-VCH Verlag GmbH&Co. KGaA, Weinheim.

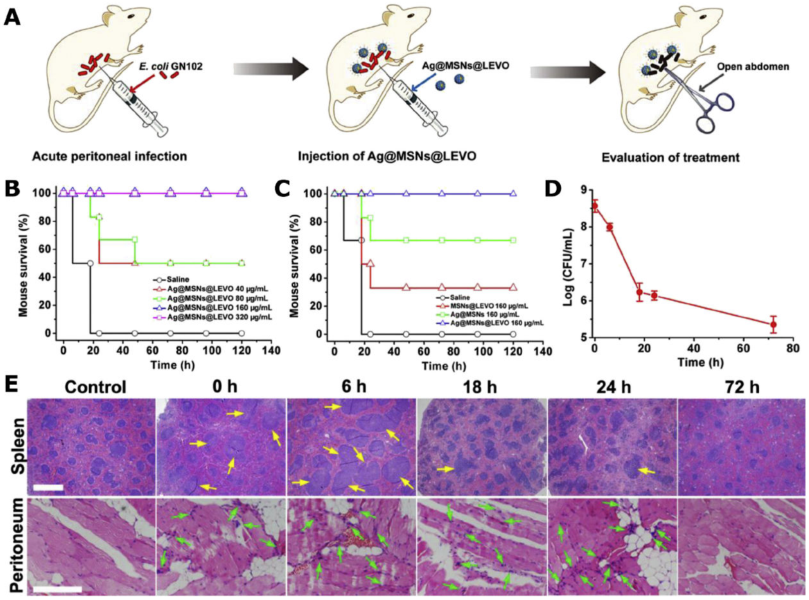

Figure 13. *In vivo* Evaluation of *E. coli* Infected Mice Peritoneal Wound Healing Effect of Ag@MSNs@LEVO.

(A) Scheme of in vivo infection and treatment procedure.

(B, C) Mice survival rates after acute peritoneal infection and treatment with Ag@MSNs@LEVO and control groups.

(D) Bacterial counts within the peritoneal cavity of mice after treatment with 160 μg/mL Ag@MSNs@LEVO.

(E) H&E staining of histological sections including spleen and peritoneum of mice after acute peritoneal infection and treatment with 160 μg/mL Ag@MSNs@LEVO. Extended lymphoid nodules on spleen and inflammatory cells on peritoneum are respectively marked with yellow and green arrows.

(A-E) Reprinted from Ref. 214, Copyright (2016), with permission from Elsevier.

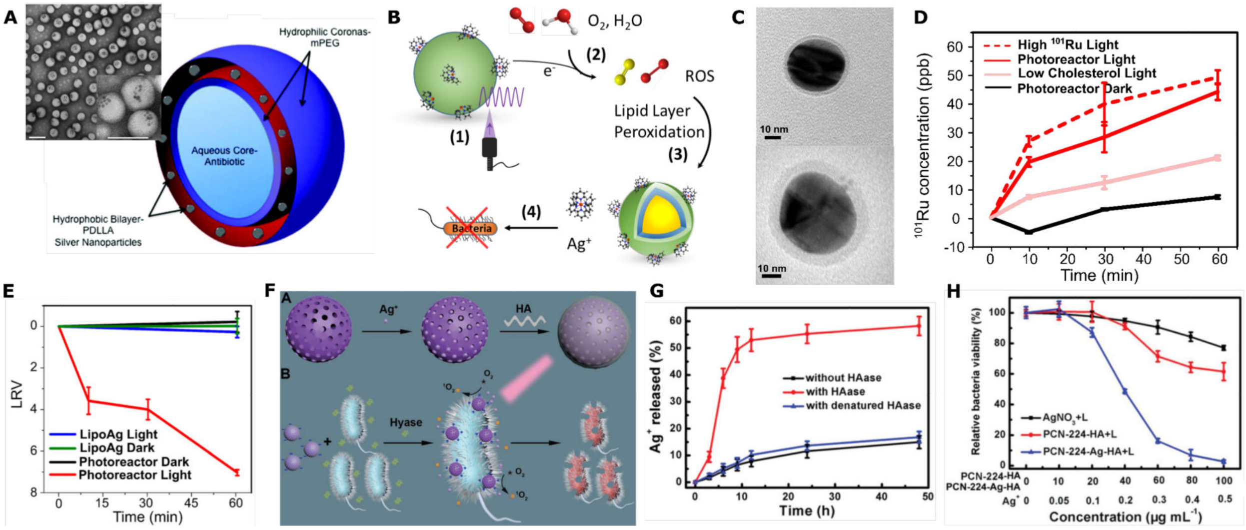

Figure 14. Delivery and Controlled Release Strategies Enabled by Plasmonic Nano-Antimicrobials.

(A) Scheme and TEM micrograph of Ag NP-polymersome system for synergistic bacteria inactivation of Ag and ampicillin. Adapted from Ref. 212 with permission from The Royal Society of Chemistry.

(B-E) Light controlled release scheme (B), TEM micrographs before (top) and after 1-hour (bottom) illumination with 430 nm LED (C), Ru release curves (D), and inactivation LRV curves for *Arthrobacter sp.* (E) with a lipid-wrapped Ag-[Ru(bpy)$_3$]$^{2+}$ photoreactor system. Reprinted with permission from Ref. 118. Copyright (2020) American Chemical Society.

(F-H) Hyase-facilitated HA degradation and release scheme (F), Ag$^+$ release curve (G) and inactivation curve of drug-resistant *E. coli* (H) by PCN-224-Ag-HA. Reproduced from Ref. 15. © 2019 WILEY-VCH Verlag GmbH & Co. KGaA, Weinheim.

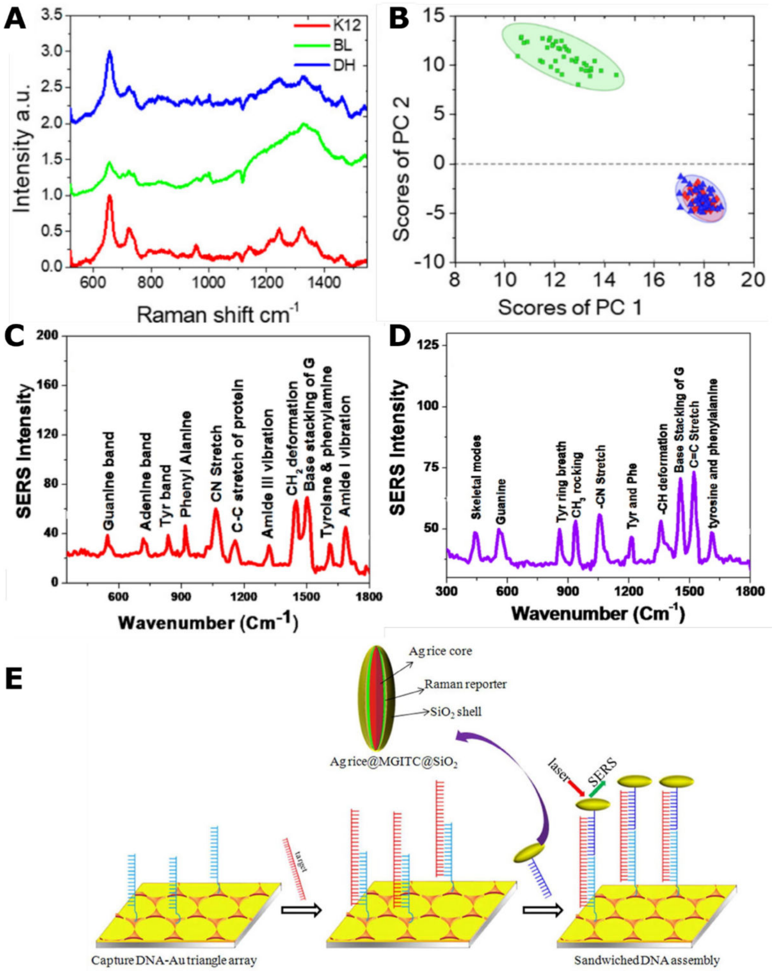

Figure 15. SERS Sensing of Microbial Pathogens.

(A-B) Average normalized SERS spectra (A) and principal component analysis with 95% confidential ring (B) of *E. coli* K12 (red), *E. coli* DH 5α E (blue) and *E. coli* BL21 (DE3) (green). Reprinted with permission from Ref. 224. Copyright (2018) American Chemical Society.

(C-D) SERS spectra of mosquito-borne flaviviruses WNV (C) and DENV (D). Reprinted with permission from Ref. 236. Copyright (2015) American Chemical Society.

(E) Scheme of structure of Ag nanorice@MGITC@SiO2 as SERS sensor for HBV DNA. Reprinted with permission from Ref. 239. Copyright (2013) American Chemical Society.

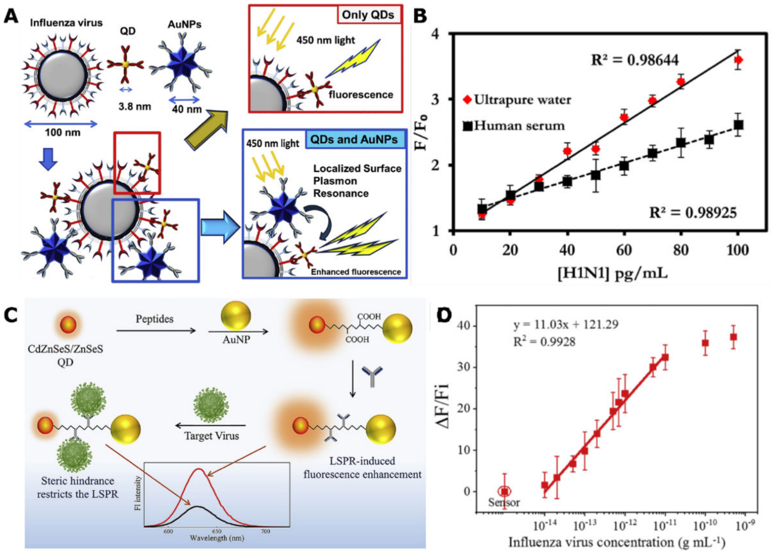

Figure 16. Plasmon-Enhanced Fluorescence Sensing of Microbial Pathogens.

(A, B) Scheme (A) and photoluminescence calibration curve (B) of a Au-QDs immunofluorescence sensor for detection of influenza H1N1 virus. Reprinted from Ref. 250, Copyright (2017), with permission from Elsevier.

(C, D) Scheme (C) and photoluminescence calibration curve (D) of a Au-QDs composite sensor for quenching-based detection of influenza H1N1 virus. Reprinted from Ref. 246. Copyright (2020), with permission from Elsevier.

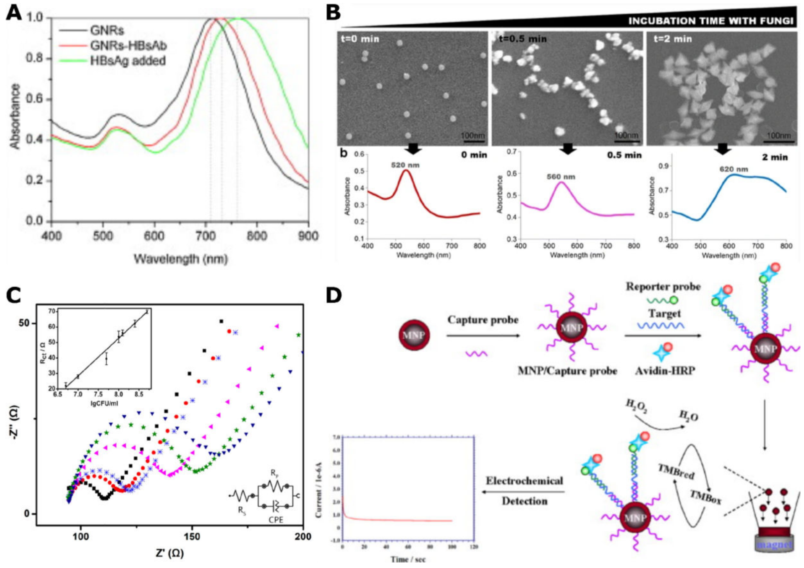

Figure 17. LSPR and Electrochemical Sensing of Microbial Pathogens.

(A) Shift of longitudinal resonance in Au nanorods (black), antibody-presenting nanorods before (red) and after (green) HBV surface antigen (HBsAg) addition. Reprinted from Ref. 254, Copyright (2010), with permission from Elsevier.

(B) SEM images and absorbance spectra of Au NPs/nanostars diagnostic agents at different incubation time with *Aspergillus niger*. Reprinted by permission from Springer Nature, Analytical and Bioanalytical Chemistry. Ref. 262. COPYRIGHT (2017).

(C) EIS study of the binding of different concentrations of *E. coli* to a Au NPs on ITO electrode in 5 mM $[Fe(CN)_6]^{3-/4-}$ electrolyte containing 0.1 M KCl. Insets: linear relationship between R_{ct} and $\log_{10}$(CFU/mL) (top left) and the equivalent circuit (bottom right). Reprinted with permission from Ref. 265, Copyright (2014) American Chemical Society.

(D) Scheme of electrochemical detection of *E. coli* by a magnetic Fe_2O_3@Au NP sensor through HRP-catalyzed hydroxide reduction. Reprinted from Ref. 267, Copyright (2011), with permission from Elsevier.

Table 1.

Summary of PDCT Pathogen Inactivation Studies.

Ref	Pathogen Species (Type)	Material / Photosensitizer	Illumination Type and Power or Power Density as Reported	*In vitro* LRV / Inactivation time	Additional Remarks
[118]	*Arthrobacter sp.* (Gram +) *E. coli* (Gram −)	Ag NPs / $[Ru(bpy)_3]^{2+}$	430 nm CW LED, 9.76 mW/cm^2	7 / 1 hour 4 / 1 hour	Light-controlled Ag$^+$ release; biofilm inactivation
[97][98]	*S. aureus* (Gram +) *E. coli* (Gram −)	Ag nanospheres or nanocubes / RB	520 nm CW LED, 4 W	7 / 2 hour 6 / 220 min	Simultaneous fluorescence imaging and inactivation
[142]	*S. aureus* (Gram +) *E. coli* (Gram −)	Ag NPs / rGO	660 nm CW laser, 180 mW	2.2 / 20 min 1.4 / 20 min	*In vivo* treatment of *S. aureus*-induced infection in mice
[124]	*T. rubrum* (fungi)	Ag@SiO$_2$ NPs / Hematoporphyrin IX dihydrochloride	400 nm CW LED, 54 mW/cm^2	> 3 / 30 min	
[147]	*C. albicans* (fungi)	Au NPs / RB	Xe lamp, 53 mW/cm^2	4.89 / 30 min	
[128]	*S. aureus* (Gram +) *P. aeruginosa* (Gram −)	Au NPs / Riboflavin	RPR-3500 A UV Lamp with center wavelength 350 nm, 9.6 mW/cm^2	3 / 2 hours 2.3 / 2 hours	
[139]	*S. aureus* (Gram +) *E. coli* (Gram −)	Ag NPs @ AgCl / Polydopamine-polyacrylamide hydrogel	Xe lamp, 0.2 W/cm^2	3.5 / 10 min 3.0 / 10 min	*In vivo* treatment of *S. aureus*-induced infection in rats; also sustains PPT inactivation
[141]	MRSA (Gram +)	Ag NPs / RB / Up-conversion nanoparticles (UCNs)	980 nm CW laser, 1 W/cm^2	4.4 / 10 min with PDCT only	Also sustains sonodynamic response for UCNs
[119]	MRSA (Gram +)	Au NRs / TBO	633 nm CW laser, 0.06 W/cm^2	1 / 1 min	Also sustains PPT inactivation
[148]	*S. aureus* (Gram +)	Au NPs/ Tin chlorin e6	White light halogen lamp, 470 μW/nm^2	> 3 / 20 min	
[121]	*S. aureus* (Gram +)	Au-Ag nanocages or Au NRs / hematoporphyrin	625 nm CW LED, 39 mW/cm^2	1–2 / 30 min	
[120]	*S. epidermidis* (Gram +) *E. coli* (Gram −)	Ag / hematoporphyrin	LumaCare LC122 lamp with White light (400 – 800 nm), 408 mW/cm^2	6–7 / 12 min	
[89]	*E. coli* (Gram −)	Au NRs / verteporfin	710 nm pulsed laser, 100 fs, 80 MHz, 1 W/cm^2	3 / 30 min	
[84]	*E. coli* (Gram −)	Au NRs / ICG	810 nm pulsed laser, 100 fs, 80 MHz, 1 W/cm^2	> 6 / 60 min	

Table 2.

Summary of PC Pathogen Inactivation Studies.

Ref	Pathogen Species (Type)	Materials Composition	Illumination Type and Power or Power Density as Reported	*In vitro* LRV / Inactivation time	Additional Remarks
[151]	*E. coli* (Gram −)	Ag NPs	Unspecified visible light source	1–2 / 2 hours	Inhibition of biofilm formation
[152]	*P. aeruginosa* (Gram −)	Au NPs	Unspecified visible light source	-	Inhibition of biofilm formation
[131]	*E. coli* (Gram −) *S. aureus* (Gram +)	Ag NPs / CuO	AM 1.5G light, 100 mW/cm^2	7 / 10 min	Light-induced Ag$^+$ release
[165]	*MRSA* (Gram +) *P. aeruginosa, E. coli* (Gram −)	Ag/TiO_2/polymer	405 nm LED, 7 W	5 / 2 hours	
[160]	*Vibrio cholerae* (Gram −)	Ag/ZnO	Sun light	> 6 / 50 min	
[132]	*E. coli* (Gram −)	Ag/AgBr/TiO_2	Visible light (> 420 nm), 25.3 mW/cm^2	7 / 110 min	
[157]	*E. coli* (Gram −)	Ag/TiO_2	Fluorescent lamp with visible light (> 400 nm), 40 W	6 / 2 hours	
[162]	*E. coli* (Gram −)	Ag/Bi_2S_3/$SnIn_4S_8$	Xe lamp (> 420 nm)	> 7 / 4 hours	
[161]	*E. coli* (Gram −)	Ag/graphitic C_3N_4	Xe lamp, 300 W	> 7 / 90 min	
[156]	Bacteriophage MS2 (non-enveloped virus)	Ag/TiO_2	UV lamp (350 nm), 2.5 mW/cm^2	> 6 / 2 min	
[158]	*E. coli* (Gram −)	Ag/ZnO	Sun light, 0.753 kW/m^2	5.7 / 60 min	
[25]	*E. coli* (Gram −)	Ag/$BiVO_4$	Xe lamp (> 420 nm), 300 W	7 / 3 hours	
[166]	*E. coli* (Gram −) *Pichia Pastoris* (yeast)	Ag/TiO_2	Mercury vapor lamp (315–400 nm), 64 W/m^2	7–8 / 45 min 8 / 60 min	
[90][91]	*E. coli* (Gram −) Bacteriophage f2 (non-enveloped virus)	Cu/TiO_2 nanofibers	Xe lamp, 100 mW/cm^2	> 6 / 240 min > 5 / 240 min	
[163]	*E. coli* (Gram −)	Ag/AgBr/reduced graphene oxide	Xe lamp, 0.383 W/cm^2	6–7 / 20 min	
[164]	*E. coli* (Gram −)	Ag/AgX/CNTs	Xe lamp, 60 mW/cm^2	7–8 / 40 min	

Table 3.

Summary of Studies on Plasmonic Photothermal Pathogen Inactivation.

Ref	Pathogen Species	Material	Illumination Type and Power or Power Density as Reported	ΔT in aqueous medium / Illumination time	*In vitro* LRV / Inactivation time	Additional Remarks
[179]	*E. coli* (Gram −)	rGO-PEG-Au NRs	700–820 nm, 100 fs, 80 MHz, 8 W/cm^2	49 °C / 10 min	7 / 10 min	
[187]	*E. coli* (Gram −) *S. aureus* (Gram +)	Ag nanoclusters / rGO	808 nm CW laser, 2 W/cm^2	15 °C / 5 min	> 2	
[188] [182]	*E. coli* (Gram −) *B. Subtilis, Exiguobacterium* (Gram +)	Nanoporous Au disks	785 nm CW laser, 0.085 W/mm^2	75 °C / 30 s	> 1 / 30 s	
[119]	MRSA (Gram +)	Ag NRs / TBO	808 nm CW laser, 3.1 W/cm^2	48 °C / 40 min	1 / 25 min	Also sustains PDCT inactivation
[87]	*E. coli* (Gram −) *S. aureus* (Gram +)	Pd@Ag nanosheets	808 nm CW laser, 0.5 W/cm^2	19 °C / 10 min	7 / 10 min	
[189]	*E. coli* (Gram −) *S. aureus* (Gram +)	Au NRs graphitic nanocapsules	808 nm CW laser, 2 W/cm^2	43.3 °C / 10 min	1–2 / 10 min	
[184]	*MRSA* (Gram +)	DNA aptamer functionalized Au NRs	808 nm CW laser, 1.1 W/cm^2	29.2 °C / 30 s	1–2 / 2 min	
[185]	*E. coli* (Gram −)	Ag / Au Nanoplates	808 nm CW laser, 1 W/cm^2	~50 °C / 5 min		*In vivo* treatment of *E. coli*-induced infection in mice
[180]	*E. coli* (Gram −)	Ag / ZnO / rGO	Xe lamp, 0.45 W/cm^2	25 °C / 30 min	7 / 30 min	
[181]	*E. coli* (Gram −)	Ag / MnO_2	Xe lamp, 0.5 W/cm^2	36 °C / 30 min	7.11 / 10 min	
[139]	*S. aureus* (Gram +) *E. coli* (Gram −)	Ag NPs @ AgCl / hydrogel	Xe lamp, 0.2 W/cm^2	32.8 °C / 10 min	3.5 / 10 min 3.0 / 10 min	*In vivo* treatment of *S. aureus*-induced infection in rats; also sustains PDCT inactivation
[186]	*Acinetobacter baumannii* (Gram −)	Ag NPs / TiO_2	Xe lamp (> 420 nm)	17 °C / 185 s	1–2 / 30 min	
[134] [183]	Bacteriophage MS2 (non-enveloped virus) Bacteriophage PR772 (non-enveloped virus) *E. coli* (Gram −)	Au NRs / carbon black composite	Sun light simulator, 100 mW/cm^2	18 °C / 30 min	1.3 / 90 min 1.6 / 90 min 5 / 90 min	Ph otothermal disinfection device

Table 4.

Plasmonic Nanostructures for Microbial Pathogen Sensing.

Ref	Sensing Modality	Pathogen	Material	Pathogen Immobilization Approach	Figure of Merit	Effect / LOD
[225]	SERS	Rotavirus (non-enveloped virus)	Antibody - conjugated Au NPs	Antigen - antibody binding	Virus SERS fingerprint from 420 – 1680 cm^{-1}	
[236]		DENV and WNV (enveloped viruses)				10 PFU/ml
[222]	TERS	TMV (non-enveloped virus)	Ag or Au NPs coated AFM tips	-	Bacteria or virus TERS fingerprints from 600 – 1700 cm^{-1}	
[223]		*S. epidermidis* (Gram +)				Spectra or maps with 20 nm lateral resolution
[221]		*B. subtilis* spores (Gram +)				
[230]	SERS	*Salmonella enterica, Salmonella enteritidis, E. coli* (Gram −) *S. epidermidis* (Gram +)	Ag NRs arrays	Vancomycin binding to bacteria cell wall	Bacteria SERS fingerprint at 728 cm^{-1} and PCA analysis	100 CFU/ml
[227]	SERS	*E. coli* (Gram −)	Ag colloid	-	PCA analysis of bacteria SERS fingerprints	Discrimination of different strains of *E. coli*
[224]			Ag nanotrough			
[51][50]	SERS	*E. coli* (Gram −) *S. aureus, B. cereus* (Gram +)	Au NP cluster arrays	-	PCA analysis of bacteria SERS fingerprints	Discrimination of different bacteria species
[233]		*E. coli, Acinetobacter calcoaceticus, P. aeruginosa,* (Gram −) *S. epidermidis* (Gram +)	Au NP arrays			
[229]		*E. coli, P. mirabilis, Klebsiella pneumoniae, K. oxytoca, C. freundii* (Gram −) Enterococcus spp. (Gram +)	Aggregated Ag colloid			
[241]	SERS	*E. coli* (Gram −) *S. aureus* (Gram +)	Ag NPs - 4-MPBA	Boronic acid - bacteria cell wall peptidoglycan binding	Bacteria SERS fingerprints from 1100 – 1400 cm^{-1}	100 CFU/ml, LRV=1.98 (24 hours)
[240]	SERS	Hepatitis B virus (enveloped virus)	Immunogold NPs – 4-MBA	Antigen - antibody binding	4-MBA v_{8a} aromatic ring vibration at 1585 cm^{-1}	0.5 μg/ml (HBV surface antigens)
[239]	SERS	Hepatitis B virus (enveloped virus)	Ag nanorice - SiO_2 shell / MGITC	Hydrogen bond (nucleotide base pairing)	MGITC SERS band at 1335 cm^{-1}	50 aM (HBV DNA)
[231]	SERS	*E. coli, Salmonella typhimurium* (Gram −) MRSA (Gram +)	Ag@Magnetic NPs / Raman Reporters	Antigen - antibody binding	PCA analysis of reporter molecules Raman signatures	10 CFU/mL
[243]	FL	*Vibrio cholerae* (Gram −)	Au nanotriangle arrays - fluorescent protein	-	FL emission intensity at 610 nm	

Ref	Sensing Modality	Pathogen	Material	Pathogen Immobilization Approach	Figure of Merit	Effect / LOD
[244]	FL	*E. coli,* Enterobacter cloacae, *P. aeruginosa, A. baumannii* (Gram −) *S. aureus, Streptococcus pyogenes, E. faecalis* (Gram +)	Human serum albumin (HSA) - Au nanoclusters	Peptide binding in HSA	FL emission intensity at 640 nm	10^6 cells/ml
[95][94]	FL	*E. coli* (Gram −)	Au@SiO$_2$ NP - Rhodamine B	“noncovalent interactions”	FL emission intensity at 550−650 nm	Bacteria imaging
[249]	FL	*E. coli* (Gram −)	Ag NPs - conjugated polyelectrolytes	Electrostatic interaction	FL emission intensity ratio at 427 nm/at 663 nm	Minimum tested CFU=10^5; LRV=2 (5 min)
[242]	FL	Zika virus (enveloped virus)	Ag NP - ATTO 647N dye - BlackBerry Quencher 650	Hydrogen bond (nucleotide base pairing)	FL emission intensity	Detection of 1 nM Zika DNA
[245]	FL	Influenza virus (enveloped virus)	Au - Carbon Nanotubes (CNTs)	Antigen - antibody binding	FL emission intensity at 970 nm	Minimum number of detectable virus particles = 900
[250] [246]	FL	Influenza H1N1 virus (enveloped virus)	Au NPs - QDs	Antigen – antibody binding	FL emission intensities	0.03 pg/mL (in water), 0.4 pg/mL from [250] or 17.02 fg/mL from [246] (in serum)
[247] [250]		H3N2 virus (enveloped virus)				10 PFU/mL from [250], 50 PFU/mL from [247]
[251]		Norovirus (non-enveloped virus)				12.1 fg/mL, 95 virus/ml
[252]		HBV (enveloped virus)				1–100 viral particles
[248]	FL	Norovirus (non-enveloped virus)	Al - QDs	Biotin - Streptavidin binding	FL emission intensity at 700 nm	0.01 ng/mL, 100 virus/mL
[262]	LSPR	*Aspergillus niger, Aspergillus oryzae, Penicillium chrysogenum, Mucor hiemalis* (fungi)	Au NPs or nanostars	-	Shift of LSPR	10 CFU/mL
[257]		*E. coli* (Gram −)	Au NPs - dextran	-		
[254]		HBV (enveloped virus)	Au NRs	Antigen – antibody binding		0.01 IU/mL HBV surface antigen
[260]	LSPR	*Influenza A virus* (enveloped virus)	Au film	-	Changes in LSPR intensity	1 ag or 0.2 fg/mm^2
[253]		*E. coli* (Gram −)			Changes in reflectivity	10^3 CFU/mL
[255]	LSPR	*E. coli, P. aeruginosa, S. typhimurium* (Gram −) *L. acidophilus* (Gram +)	Au coated silica NPs - aptamers	aptamer	Changes in extinction	10 – 3×10^4 CFU/mL
[259]	LSPR	Avian Influenza virus H5N1 (enveloped virus)	Hollow Au spike NPs - DNA 3-Way Junction	aptamer	Changes in LSPR intensity	I pM hemagglutinin protein in buffers
[270]	EC				current	

Ref	Sensing Modality	Pathogen	Material	Pathogen Immobilization Approach	Figure of Merit	Effect / LOD
[258]	LSPR, EC	*E. coli* (Gram −) MRSA (Gram +)	Au - bacteriophage	Virus-bacteria interaction	Changes in LSPR intensity, impedance	10^3 CFU/mL
[263]	EC	Zika virus	Au NPs - antibody	Antigen - antibody binding	Impedance	10 pM Zika virus protein
[265]		*E. coli* (Gram −) *S. aureus* (Gram +)	Au NPs	Doxorubicin - bacteria binding		
[264]		Hepatitis B virus (enveloped virus) Papilloma virus (non-enveloped virus)	Au NPs - SWCNT	Hydrogen bond (nucleotide base pairing)		1 aM HBV ssDNA
[267]	EC	*E. coli* (Gram −)	Fe_2O_3@Au NPs	Hydrogen bond (nucleotide base pairing)	Current	0.01 pM DNA, 5 CFU/mL *E. coli*
[268]		HIV-1 (enveloped virus)	Au NPs - antibody	Antigen - antibody binding		375 pg/mL
[266]		*E. coli* (Gram −)	rGO - Au@Pt			4.5×10^2 CFU/mL
[269]		Avian leukosis virus subgroup J (enveloped virus)	Nanocellulose - Au composite			$10^{1.98}$ TCID/mL
[185]	PA	*E. coli* (Gram −)	Au@Ag nanoplates	-	PA signals	PT inactivation and PA imaging of wound
[273]		MRSA (Gram +)	Ag-capped Au NRs	-		Ag+ inactivation and PA imaging of wound
[274]		*S. aureus* (Gram +)	P1 peptide-Au NPs	Peptide binding		PA imaging of wound

Table 5.

Comparison of Plasmonic Nano-Antimicrobials with Other Antimicrobial Strategies.

	Conventional Sterilization Techniques	**Plasmonic Nano-Antimicrobials**	**Other Nanoscale Antimicrobials**	**Molecular Antimicrobial Drugs or Peptides**	**Macroscale Antimicrobial Materials or Coatings**
Broad-band antimicrobial efficacy	✓	✓	✓	✓	✓
Visible light responsivity		✓✓	✓		
Resilience against microbial resistance development	✓	✓	✓		✓
Large-scale and repeatable i*n vitro* inactivation effect	✓	✓	✓	✓	✓
Specificity in *in vivo* disinfection applications				✓	
Sensing and theranostic capability		✓✓	✓		✓
Low cost and low energy and environmental hazards				✓	✓